

Xubo Yan

Synthesis and properties of novel single-chirality multi-wall carbon nanotubes
and silicon nitride nanocones

Schriftenreihe der Arbeitsgruppe des Lehrstuhls für Oberflächen- und
Werkstofftechnologie im Institut für Werkstofftechnik

Impressum

Prof. Dr. rer. nat. habil. Xin Jiang
Lehrstuhl für Oberflächen- und Werkstofftechnologie
Institut für Werkstofftechnik
Universität Siegen
57076 Siegen
ISSN: 2194-0096
Zugl.: Siegen, Univ., Diss., 2015

**SYNTHESIS AND PROPERTIES OF NOVEL SINGLE-
CHIRALITY MULTI-WALL CARBON NANOTUBES AND
SILICON NITRIDE NANOCONES**

Vom Department Maschinenbau
der Universität Siegen

zur Erlangung des akademischen Grades
Doktor-Ingenieur
genehmigte

Dissertation

von:	M. Sc. Xubo Yan
aus:	Hebei, China
eingereicht am:	01. Dezember 2014
Mündliche Prüfung am:	17. Februar 2015
Referent:	Prof. Dr. rer. nat. habil. Xin Jiang
Korreferent:	Prof. Dr. Holger Schönherr

Zusammenfassung

Der Fokus dieser Arbeit liegt auf der Synthese sowie den Untersuchungen des Wachstumsmechanismus und der Eigenschaften von monochiralen, mehrwändigen Kohlenstoffnanoröhren (*multi-wall carbon nanotubes*, MWCNT) sowie einkristallinen Siliciumnitrid (Si_3N_4) – Nanokegeln. Drei grundlegende Ziele wurden hierbei verfolgt: i) das Erzielen eines hochqualitativen Wachstums von CNTs und Si_3N_4 -Nanokegeln, ii) die Aufklärung der entsprechenden Wachstumsmechanismen der aufgewachsenen Nanomaterialien mittels HR-TEM und iii) die Erkundung der physikalischen Eigenschaften der synthetisierten Materialien, um mögliche Anwendungen identifizieren zu können. Die Synthese erfolgt hierbei im Rahmen der Arbeit mittels einer plasmaunterstützten chemischen Gasphasenabscheidung.

Inspiziert wurde die Arbeit durch in-situ Untersuchungen des katalytischen Wachstums von Kohlenstoffnanoröhren auf festen Eisencarbid (Fe_3C) Katalysatoren. Verbindungen von Übergangsmetallen (Fe, Co, Ni) mit Elementen, die einen, im Vergleich zum Übergangsmetall, hohen Schmelzpunkt aufweisen, scheinen, insbesondere in kohlenstoffhaltiger Atmosphäre, potentielle Kandidaten für ein Chiralitäts-kontrolliertes Wachstum von Kohlenstoffnanoröhren zu sein. Letzteres wird durch die Tatsache unterstützt, dass feste Katalysatoren die Möglichkeit besitzen kristallographische Informationen auf die zu wachsenden CNTs zu übertragen. In diesem Zusammenhang konnten im Rahmen dieser Arbeit neue Erkenntnisse bei der Verwendung von Fe-Cr-Carbiden als Katalysator erzielt werden. Flächenselektive Elektronendiffraktometrie (*selective area electron diffraction*, SAED) zeigte, dass monochirale MWCNTs katalytisch auf $(\text{Cr,Fe})_7\text{C}_3$ wachsen können. Durch systematische Untersuchung der Grenzfläche von Katalysator und CNT mittels hochauflösender Transmissionselektronenmikroskopie (*high resolution transmission electron microscopy*, HR-TEM) konnte nachgewiesen werden, dass das Wachstum der Graphitschichten durch einatomigen Stufen des Katalysators entlang der c-Achse initiiert wird. Diese Stufen bestehen aus einer Basisfläche sowie einer $\{20\cdot21\}$ -Flächen des Katalysatormaterials. Durch eine Kombination von SAED und HR-TEM konnte weiter gezeigt werden, dass unterschiedliche Orientierungen des Katalysators zu einer Ausbildung von monochiralen MWCNTs mit entsprechend unterschiedlichen Chiralwinkeln führen. Im Besonderen wurde gefunden, dass mit Katalysatoren mit einer $[0002]$ bzw. einer $[10\cdot10]$ -Orientierung Kohlenstoffnanoröhren mit chiralen Winkeln von 0° bzw. $4,5^\circ$ ausbilden. Dieses Erkenntnis lässt das Potential erkennen, gezielt CNTs mit definierten Chiralitäten für

Anwendungen in der Nanotechnologie CNTs erzeugen zu können. Die chiralen Indizes (n,m) der erzeugten CNTs wurden mittels weiterer sehr detaillierter SAED-Untersuchungen aufgeklärt. Ebenso wurde die Beziehung zwischen der Chiralität und der zugehörigen Facettenmorphologie untersucht. Auf bereits zuvor berichtete Unterschiede in den Ramanspektren der hier erzeugten zu verschiedenen anderen CNTs wurde in der Arbeit ebenfalls nochmals eingegangen.

Schließlich gelang im Rahmen dieser Arbeit erstmals die Synthese von β -Si₃N₄-Nanokegeln mittels plasmaunterstützter Gasphasenabscheidung. Hierbei wurde der redox-induzierte Wachstumsmechanismus eingehend analysiert. Abschließend wurde Photolumineszenz sowie der Einfluss der Morphologie auf die optischen Eigenschaften des Materials untersucht, um seine Eignung in Bezug auf potentielle Anwendungen zu evaluieren.

Acknowledgements

First of all, I would like to express my deep appreciation to my thesis advisor Prof. Xin Jiang for his guidance and great support during my doctoral period in University of Siegen. Prof. Jiang's penetrating insight and broad knowledge enabled me to develop a deep understanding of the subject. It is an honor for me to learn his attitude towards life and research, which is beneficial for all my life.

I would like to render my sincere gratitude to Prof. Holger Schönherr for readily agreeing to be co-referee for my thesis and related efforts. I also would like to thank Prof. Robert Brandt and Prof. Jörn Schmedt auf der Gönne for their contributions during the examination process.

The help extended by all of my colleagues at LOT, University of Siegen is greatly appreciated. Great thanks are given to Dr. Hao Zhuang for his constructive discussions and help during my thesis work. Many thanks are given to Dr. Lei Zhang for his great help in analysis of TEM. Thanks also to Thomas Degen and Michael Vogel for their help in construction of the reaction chamber and trouble shooting. Special thanks to Steffen Heuser for helping me in preparing the German version of the thesis abstract. I also would like to take this chance to thank Dr. Nan Huang and Dr. Bing Yang from Institute of Metal Research, CAS, for their help and discussion in the analysis of TEM and photoluminescence property. Thanks to Dr. Staedler, Dr. Nianjun Yang, Dr. Yao Ma, Petra auf dem Brike, Claudia Kretzer, Andrea Brombach, Haiyuan Fu, Tao Wang, Siyu Yu, and other colleagues for their kind help in my doctoral period.

This work would not have been possible without the help of my family. Their love and encouragement in every aspect allows me to overcome the difficulties I have met. Special thanks are also given to my girl friend, Hongyu She, for her support during my life and study. Thanks to China Scholarship Council(CSC) for the financial support in the past four years. The last but not the least, I would like to thank all my friends for their treasured memory and support.

Contents

Symbol List	III
Abstract	VII
1 Introduction	1
1.1 Nanomaterials	1
1.1.1 Classifications of nanomaterials	1
1.1.2 Characteristic of nanomaterials	3
1.1.3 Preparation techniques of nanomaterials	5
1.2 Objective of the thesis	6
1.2.1 Carbon nanotubes	6
1.2.2 Silicon nitride nanomaterials	6
1.3 Overview of the thesis	7
2 Theoretical background of carbon nanotubes and Si₃N₄ nabomaterials	9
2.1 Carbon nanotubes	9
2.1.1 The structure of carbon nanotubes	12
2.1.2 Synthesis techniques of carbon nanotubes	16
2.1.3 Growth Mechanism of Carbon Nanotubes	18
2.1.4 Theory for determination of the chiral indices (<i>m</i> , <i>n</i>) of carbon nanotubes	23
2.2 Silicon nitride nanomaterials	26
2.2.1 Structure of silicon nitride	27
2.2.2 Morphologies of silicon nitride nanomaterials	29
3 Experimentation	36
3.1 Materials preparation	36
3.1.1 Technique	36
3.1.2 Procedure	37
3.2 Characterization tools	39
3.2.1 Scanning electron microscopy (SEM)	39
3.2.2 Transmission electron microscopy (TEM)	39
3.2.3 X-ray diffraction (XRD)	40
3.2.4 Micro Raman scattering	40
3.2.5 Photoluminescence spectroscopy	40
4 Synthesis of single-chirality multi-wall carbon nanotubes	42

4.1 Strategies for chirality-controlling growth of carbon nanotubes	42
4.2 Synthesis of single-chirality multi-wall carbon nanotubes	47
4.2.1 The catalyst selection	47
4.2.2 The synthesis process	49
4.2.3 The characterization of catalyst	53
4.2.4 The characteristic of as-grown carbon nanotubes	56
4.2.5 Determination of the chiral indices (m , n) of carbon nanotubes	61
4.3 Single-chirality controlling of multi-wall carbon nanotubes	63
4.3.1 Variations of catalyst	64
4.3.2 Nucleation of the graphite layers	67
4.3.3 Step-site controlling the single-chirality	72
4.3.4 Growing into long tubes	79
4.4 The ‘visible’ chirality	80
4.5 Raman Spectra Analysis of single-chirality multi-wall carbon nanotubes	84
5 Synthesis and photoluminescence property of silicon nitride nanocones	91
5.1 Synthesis of β -silicon nitride nanocones	91
5.2 Characterization of β -silicon nitride nanocones	94
5.3 Growth mechanism of β -silicon nitride nanocones	97
5.4 Photoluminescence property of β -silicon nitride nanocones	101
6 Conclusions	104
7 References	107
Appendix I	124
Appendix II	127

Symbol List

Abbreviations

1D	one dimension
2D	two dimension
AC	alternating current
CNT	carbon nanotube
CCVD	catalytic chemical vapor deposition
CVD	chemical vapor deposition
DFT	density function theory
DNA	deoxyribonucleic acid
ED	electron diffraction
EDX	energy dispersive X-ray spectroscopy
ETEM	environmental transmission electron microscopy
FESEM	field effect scanning electron microscopy
FWHM	full-width half-maximum
HRTEM	high resolution transmission electron microscopy
JCPDS	the joint committee on powder diffraction standards
MWCNT	multi-wall carbon nanotube
MWCVD	microwave plasma enhanced chemical vapor deposition
NPCs	nanoparticles
PCVD	plasma chemical vapor deposition
PL	photoluminescence
RBM	radial breathing mode
SEAD	selective area electron diffraction
SEM	scanning electron microscopy
SWCNT	single-wall carbon nanotube
TEM	transmission electron microscopy
TGCs	tubular graphite cones
VLS	vapor liquid solid
VS	vapor solid
XRD	X-ray diffraction

Symbols

$^{\circ}$	degree
$^{\circ}\text{C}$	degree centigrade
μm	micrometer
A	ampere
\AA	Angstrom unit
Ag	silver
Al	aluminium
Al_2O_3	aluminum oxide
Au	gold
BaTiO_3	barium titanate(IV)
Be_2SiO_4	phenakite
C	carbon
CaTiO_3	calcium titanate
Ce	cerium
CH_4	methane
cm	centimeter
Co	cobalt
CO	carbon monoxide
Cr	chrome
Cu	copper
d	diameter
eV	electron volt
Fe	iron
Gd	gadolinium
GHz	Giga Hertz
H_2	hydrogen
kW	kilo watt
kV	kilo volt
mA	milli ampere
mW	milli watt
m^2/g	square meter per gram
min	minute
MgAl_2O_4	spinel

MgO	magnesium oxide
Mo	molybdenum
N ₂	nitrogen
NH ₃	ammonia
Ni	nickel
nm	nanometer
O	oxygen
Pd	lead
PbTiO ₃	lead titanate
Pt	platinum
Rh	rhodium
Ru	ruthenium
s	second
sccm	standard cubic centimeter per minute
Si	silicon
Si ₃ N ₄	silicon nitride
SiC	silicon carbide
SiO ₂	silicon dioxide
sp ²	sharp-principal-two
sp ²	sharp-principal-three
SrTiO ₃	strontium titanate
Ti	titanium
V	volt
W	watt
W	tungsten
Y	yttrium
YAG	yttrium aluminium garnet
ZnO	zinc oxide
α	alpha
β	beta
λ	wavelength
θ	theta
ω	omega

Abstract

This thesis focusses on the investigation of the synthesis of single-chirality multi-wall carbon nanotubes (MWCNT) and single-crystalline silicon nitride (Si_3N_4) nanocones as well as the growth mechanism and properties of both products. Three key objectives were pursued: i) to grow high quality CNTs and Si_3N_4 nanocones; ii) to investigate the growth mechanisms of as-grown nanomaterials by HR-TEM, and iii) to evaluate their physical properties with respect to potential applications. A microwave plasma enhanced chemical vapor deposition technique was utilized in this work to realize materials synthesis.

Inspired by in situ investigation of the growth of carbon nanotubes based on a solid iron carbide (Fe_3C) catalyst, alloys of transition metals (Fe, Co, Ni) and elements, which feature a higher melting point than the transition metals itself, especially in the carbon-rich atmosphere were chosen as potential candidates for a chirality-controlling growth of CNTs. These in particular offer the possibility to transfer crystallographic information from the catalyst to the as-grown CNTs. In this context, new results were obtained for the Fe-Cr carbide catalyst system. Selected area electron diffraction (SAED) patterns show that it is possible to grow single-chirality MWCNTs by employing $(\text{Cr,Fe})_7\text{C}_3$ catalysts. Systemic observations of the interface of as-grown CNTs and the catalysts by high resolution transmission electron microscopy (HR-TEM) revealed that graphite layers grow according to the c axis. Their growth is initiated by monoatomic step sites of the catalysts, which consist of a basal and a $\{20\cdot21\}$ plane of the catalyst. By combining SAED patterns and HR-TEM images, it could be concluded that different directions of the catalyst are responsible for the growth of single-chirality MWCNTs that feature different chiral angles. In particular, chiral angles of 0° and 4.5° were observed for catalysts that showed $[0002]$ and $[10\cdot10]$ direction, respectively. This correlation represents an opportunity to grow MWCNTs with a predefined chirality and properties, which are directly tailored for the requirements of specific applications or needs in CNT based nanoscience and nanotechnology. The chiral integers (n,m) of the as-grown CNTs were confirmed by a detailed study of the corresponding SAED patterns. Furthermore, the relationship between chirality and the facet morphology was investigated. Additionally, it was possible to confirm various characteristic features in the Raman spectra of the nanostructures analyzed here, which differed from those of other CNTs reported before.

Finally, aside from the CNTs mentioned above, $\beta\text{-Si}_3\text{N}_4$ nanocones were successfully synthesized via microwave plasma enhanced chemical vapor deposition technique for the first time within the framework of this thesis. Their redox induced growth mechanism was investigated

and their photoluminescence properties as well as the effect of their morphology on their corresponding optical properties were evaluated regarding potential applications.

1 Introduction

1.1 Nanomaterials

In 1980s, the ability of nature remarking to human beings extends to atomic and molecular level with the discovery of nanoscience and technology, which opens a new era for science research — Nanoscale Science and Technology Era. The development of nanoscale science and technology will drive the technological innovation in fields of Information Science, Material Science, Energy, Environment, and Agriculture and so on, which definitely gives rise to a new technological revolution.

Materials containing nanophase being studied for the first time can go back to 1950s. German scientists W. Kanzig and colleagues observed “polar regions” near the surface of BaTiO_3 crystals¹, whose size is among 10-100 nm. Later scientist of Soviet Union G.A. Smolensky² deduced that the reason for the dielectric dispersion in composite CaTiO_3 was the inhomogeneous of composition caused by existence of this “polar regions”. In this sense, nanophase exists in ferroelectric ceramics indeed and affects their electric property. But this could not attract a lot at that time.

Until 1960s, scientists began to study nanoparticles consciously to discovery the mystery of nanoworld. The concept of nanomaterial was firstly mentioned in a 1959 talk by famous scientist R. Feynman³. And later in 1962, Japanese scientist R. Kubo proposed “Kubo theory” based on the study of metallic nanoparticles⁴, which pushed experimental physicists towards further study on nanoscale particles. In 1980s, nanometer, not only used as a length unit, was defined a kind of material with a size of 0.1-100nm. At the beginning of nanomaterial research, nanomaterial just referred to nanoparticles and nano films and solids composed by nanoparticles. While, until now materials with at least one dimension in the range of nanoscale or their composites can be named nanomaterials. In July, 1990, the first International Conference on Nanoscience and Technology was hold in Baltimore, USA, which regarded nanomaterial science as a new branch of materials science. Since then, nanomaterials attract more and more scientists all over the world to work on them.

1.1.1 Classifications of nanomaterials

According to the difference of dimensionality of basic units composing nanomaterials, nanomaterials can be divided into four classes, shown in Fig. 1.1:

- Zero-dimensional: the entire three space dimensions are in the range of nanoscale.
- One-dimensional: two of the space dimensions are in the range of nanoscale.
- Two-dimensional: only one space dimension is in the range of nanoscale.

- Three-dimensional: solid materials composed of nanomaterials mentioned above.

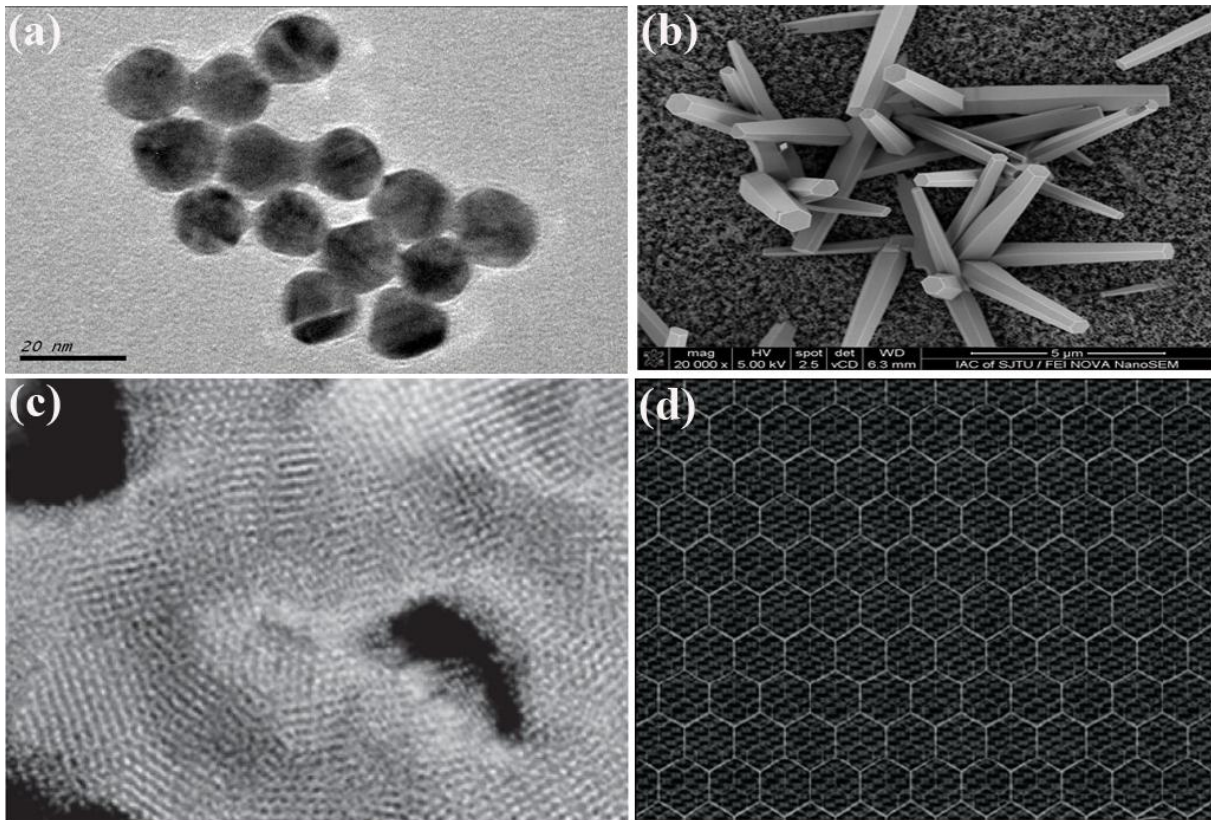


Figure 1.1. Four classes of nanomaterials: (a) Au nanoparticles⁵; (b) ZnO nanorods⁶; (c) Superlattices assembled by SiO₂ nanoparticles⁷; (d) MgO ceramics implanted with Ni atoms in nanoscale⁸.

Typical zero-dimensional nanomaterials are nanoparticles. These particles, with a granularity under 100 nm, are in the intermediate state between atoms, molecules and macroscopic objects. This kind of nanomaterials can be used as high-performance thermal insulation materials, high-density magnetic recording materials, absorbing materials, radiation proof materials, magnetic fluid materials, polishing materials for precision components, light sensitive materials, advanced battery and electrode materials, high-performance catalysts, combustion improvers, high-strength or high-ductility ceramics, the human body repairing materials and anti-tumor compositions and so on.

One-dimensional nanomaterials often lead to tubular, wire or rod materials with the diameter in the range of nanoscale and a long length. Carbon nanotubes⁹ (CNTs) are typical ones. These materials can be found used as micro cables, micro optical fibers and new laser materials and light-emitting diodes materials.

Super-thin films, multi-layered films and superlattice structures belong to two-dimensional nanomaterials. For two-dimensional nanofilms, they can be divided to two classes on the basis of different distribution. Nanoparticles sticking together with slender gaps

between each other compose granular films, while, nanoscale grains arranged together with on gaps form dense membranes. The application of these nanofilms is normally in gas catalytic materials, the filtration membrane materials, high-density magnetic recording materials, flat panel display manufacturing materials, and super conductivity materials and so on.

Three-dimensional nano ceramics are nano powders formed aggregates under high pressure. They can be used in high-strength materials, thermal insulation materials and intelligent materials and so on.

Besides those mentioned above, research on nanomaterials can also focus on: object surface with a roughness less than 100 nm, the assembling system of nanoparticles and porous medium, and the composites of nanoparticles and macro materials.

Since all the units show quantum nature, the unit of zero-, one- and two-dimensional nanomaterials can also be called quantum dot, quantum wire and quantum wall, respectively. With the development of nanoscience and technology, a mount of novel materials and devices based on one or more nanomaterials were exploited to meet the different needs of human beings. They can be called the fifth class of nanomaterials.

1.1.2 Characteristic of nanomaterials

Apart from the aspect of size, nanomaterials also show unique physical and chemical properties compared with atoms, molecules or macro objects. When the nanometer size range of materials is reached, nanomaterials perform typical distinctive phenomena: little size effect, surface effect, quantum measurement effect and macroscopical quantum tunnel effect.

Little size effect

When the crystal size is less than some physical characteristic lengths, such as optical wavelength, the de Broglie wavelength of conduction electron, and the coherent length or transmission depth of superconducting state, the periodic boundary conditions upon which normal state materials form will be destroyed. As a result, the atom density near the surface of amorphous nanoparticles will decrease, which result in the corresponding properties of acoustics, optics, thermology, mechanics and electromagnetics will show novel phenomena compared with those of bulk.

Surface effect

Due to the small size of nanoparticles, the volume fraction of atoms at the surface is huge, generating a large surface energy. With the decrease of the size of the nanoparticles, the specific surface area and the amount of atoms at the surface increase dramatically. For example, when the particle diameter is 5 nm, the specific surface area and the ratio of surface atoms

are $180 \text{ m}^2/\text{g}$ and 50%, respectively. While, those for the particles with a diameter decreases to 2 nm, are $450 \text{ m}^2/\text{g}$ and 80%, respectively. The increase in the number of surface atoms and the specific surface area causes the lack of coordination number and the presence of unsaturated bonds, resulting in many defects at the surface of nanomaterials. Therefore, these surfaces have a high activity and are particularly vulnerable to absorb or react with other atoms. The activity of surface atoms not only causes the change of surface transport and configuration, but also influent the electron spin, conformation and electron spectrum.

Quantum measurement effect

When the particle size is reduced to a certain level, the electron energy level near the Fermi level turns to be discrete instead of quasi-continuous level. For nanoparticles, as contained a few number of electrons, the energy gap no longer tends to zero, thus discrete energy levels is formed. Once the gas of the discrete level is greater than the characteristic value of thermal energy, magnetic energy, electric energy and photon energy, energy level varying, energy band gap broadening, emitted energy of particles increasing will be resulted in. The blue shift of optical absorption will also be stirred up, intuitively causing the change of the color.

Macroscopical quantum tunnel effect

It is well known that although the total energy of nanoparticles is less than barrier height, the particles can still pass through this barrier, which is so-called quantum tunnel effect. But recently, it was discovered that some macroscopic quantities, such as magnetization of nanoparticles and magnetic flux of quantum coherence devices, can also perform tunnel effect. These phenomena were named macroscopical quantum tunnel effect.

These features make nanoparticles and nano-solid exhibit many exotic physical and chemical properties, even “anomalies”. Examples below are given to describe those exotica. Metal is known as a conductor, but at low temperature metal nanoparticles are rendered electrically insulating due to the quantum size effect¹⁰. PbTiO_3 ¹¹, BaTiO_3 ¹² and SrTiO_3 ¹³ normally used as typical ferroelectric materials, becomes paraelectric when their size decrease to nanometer scale. The poly-domain of ferromagnetic materials turns to the single domain when their size is reduced to 5nm, resulting a strong paramagnetic effect¹⁴. Silicon nitride ceramics composed of nanoparticles with a size of several tens of nanometers have no typical characteristics of covalent bonds. Instead, partial polarization appears at the interface, causing a small resistance on AC power¹⁵. Bulk platinum is chemically inert, while, platinum nanoparticles have an excellent catalyst activity¹⁶. Metals present a variety of beautiful colors due to high light reflection. But that of metal nanoparticles decreases obviously, usually to as low as

1%¹⁷. The reason for that is the little size effect and surface effect. Fracture strength of iron nanomaterials with a size of 6 nm is 12 times higher than that of polycrystalline bulk iron¹⁸. Thermal diffusion coefficient and specific heat of Cu nanocrystals are 1016-1019 times and twice higher as those of conventional pure Cu, respectively¹⁹. Heat expansion coefficient of Pd nanocrystals increases to two times of that of bulk Pd crystals²⁰. Heat exchange rate raises 30% by utilize Ag nanocrystals as dilution refrigerator instead of traditional bulk materials²¹. Magnetic susceptibility of nano metal is 20 times as that of bulk metal, while saturation moment is only a half²².

1.1.3 Preparation techniques of nanomaterials

Nanomaterials deal with very fine structures, normally several, tens or hundreds of nanometers. There are two approaches to synthesize nanomaterials: “bottom up”²³ and “top down”²³, schematically shown in Fig. 1.2. The former is to assemble atoms together, while the latter is to dis-assemble (break, or dissociate) bulk solids into finer pieces until they are constituted of only a few of atoms. This domain is an interdisciplinary work encompassing physics, chemistry, and engineering upto medicine.

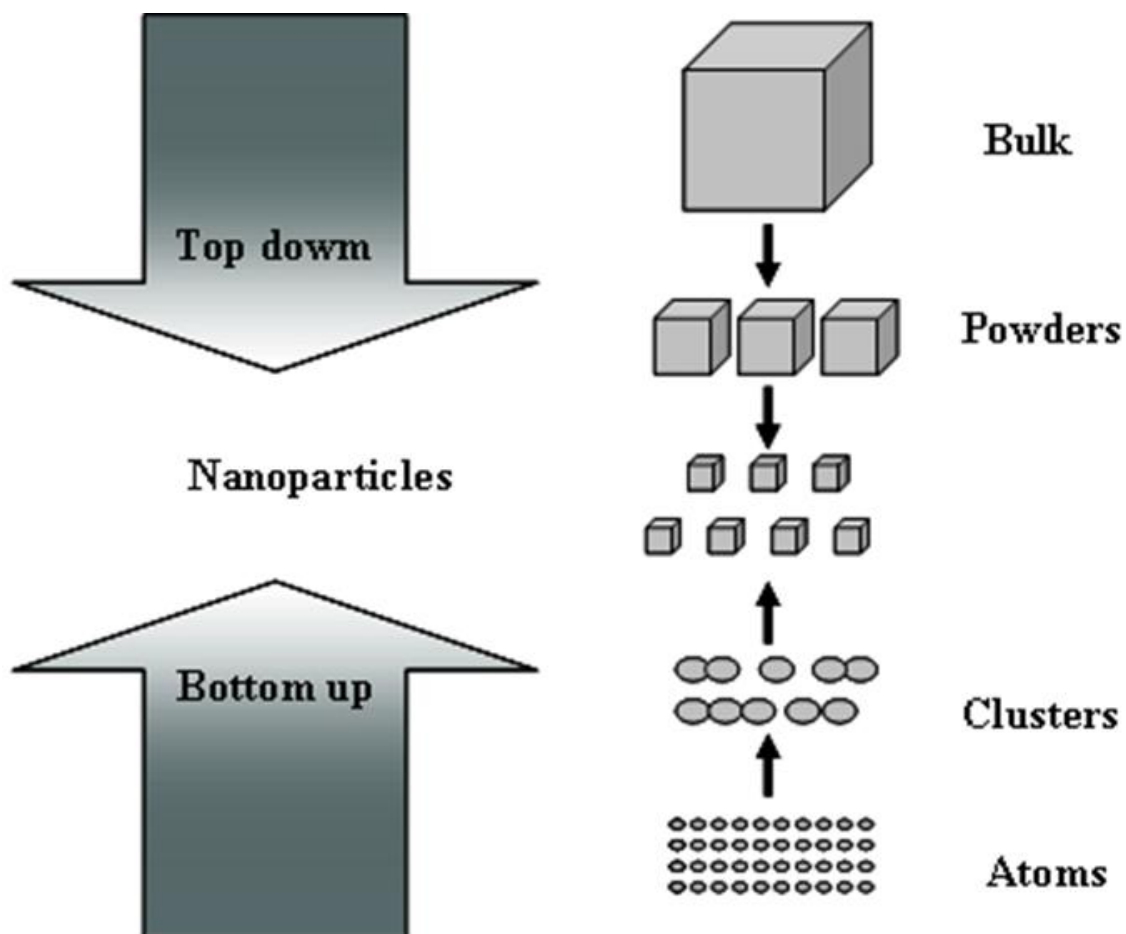


Figure 1.2. Schematic illustration of the two approaches of nanoparticles preparation.

There are many different ways of creating nanostructures. Among them, mechanical grinding²⁴, electrochemical etching²⁵, sputtered plasma processing²⁶ and laser ablation²⁷ belong to “top down” approach. The “bottom up” approach consist of gas condensation process²⁸, chemical vapor deposition²⁹, precipitation³⁰, sol-gel method³¹, hydrothermal method³² and spray pyrolysis³³. Of course, macromolecules or nanoparticles or buckyballs or nanotubes and so on can be synthesized artificially for certain specific materials. They can also be arranged by methods based on equilibrium or near-equilibrium thermodynamics such as methods of self-organization and self-assembly (sometimes also called bio-mimetic processes)³⁴. Using these methods, synthesized materials can be arranged into useful shapes so that finally the material can be applied to a certain application.

1.2 Objective of the thesis

1.2.1 Carbon nanotubes

Carbon nanotubes have excellent properties which are attractive for applications as the main component of nanodevices in many fields. And tremendous effort has been devoted to the promising studies. However, a key question restrict the further development. That is during the synthesis process, CNTs, either SWCNT or MWCNT, have a mixed microstructure which can definitely weaken the advantages of these novel materials. The precisely controlling of the structures of carbon nanotubes have not yet been explored in detail, and further work would be useful here, both from a fundamental standpoint and in view of the potential applications of these structures. Intensive researches have been carried out to successfully sort the as-gained CNTs to get what they want by some chemical, mechanical methods³⁵⁻⁴¹. But this not only decreases the outputs, but also is not economical. The latest idea is to focus on the catalysts utilized during the CNTs growth⁴²⁻⁴⁷. Since catalysts could maintain its structure and morphologies during the process, the interaction of the catalysts and the as-gained CNTs may be possible for the single microstructure controlling. Therefore, finding a suitable catalyst system seems crucial. A systematic study of a various of catalyst which may be metals, the combinations of two or more metals and their nitrides and carbides in order to catalyze single-chirality CNTs and the detailed investigation of the interaction of the catalysts and the as-gained CNTs form the main object of the study of carbon nanotubes in this thesis.

1.2.2 Silicon nitride nanomaterials

Si₃N₄ is an advanced material and usually two types of structural modifications exist, namely, metastable, low-temperature-phase trigonal α -Si₃N₄, and stable hexagonal β -Si₃N₄.

Si_3N_4 is one of the most important technical ceramics and can be a suitable material for a wide range of technical applications, especially for high-temperature engineering applications. However, compare with $\alpha\text{-Si}_3\text{N}_4$, pure single-crystalline $\beta\text{-Si}_3\text{N}_4$ nanostructures which may have better performances, have seldom reported. In recent few years, nanocones have emerged as a new kind of one dimensional nanostructure which is superior to nanotubes, nanowires, and nanobelts in some aspects⁴⁸⁻⁴⁹. For example, it is found that nanocones are more potential candidates for scanning probes and field emitters due to their radial rigidity, which eliminates the poor signals and noise caused by mechanical or thermal vibration⁴⁸. Furthermore, cone-shape structures are confirmed to have a novel photoluminescence property⁴⁸. As an important light-emission material, the nanocones-shape Si_3N_4 is promising. Therefore, the synthesis of $\beta\text{-Si}_3\text{N}_4$ nanocones and study of its photoluminescence property form another object of this thesis.

1.3 Overview of the thesis

In this thesis, Chapter 1 presents a short introduction of the nanomaterials and the main objective of this thesis. Chapter 2 gives the theoretical background about carbon nanotubes and silicon nitride nanomaterials.

Chapter 3 describes the main experimental methods that have been adopted in this work. The basic aspects about the MWCVD deposition equipment and deposition procedure are firstly explained. The main characterization techniques that have been used in obtaining the structural and compositional information are also described.

Chapter 4 presents the deposition and characterization results of single-chirality multi-wall carbon nanotubes. The strategy for possible chiral-controlling carbon nanotubes growth starts this chapter. Next follow is the growth process of single-chirality multi-wall carbon nanotubes. Then follow is the characterization of the catalysts and as-grown carbon nanotubes. The relationship of the instinctual chiral property and the facet morphology is discussed in detail. Raman spectra analysis of single-chirality carbon nanotubes ends this part.

Chapter 5 presents the growth and property of novel silicon nitride nanocones. The characteristic of the cones starts this section. Follow is the growth mechanism. The photoluminescence property of this new form nanomaterial of silicon nitride is detailed discussed as the end of this chapter. Chapter 6 presents the conclusions of this thesis work.

All the references that have been cited in the thesis have been arranged and numbered in the order they appear in the main text under the heading "References". Styles of each journal

citation are as follows: Authors names, *Journal name*, **Year**, *Volume number*, Starting page/article number.

2 Theoretical background of carbon nanotubes and Si₃N₄ nabomaterials

2.1 Carbon nanotubes

A carbon atom has four electrons in its outer valence shell; the ground state configuration is $2s^2 2p^2$. Diamond and graphite are considered as two natural crystalline forms of pure carbon. In diamond, carbon atoms exhibit sp^3 hybridization, in which all the electrons forms four equal C-C bonds with four other atoms occupying the vertices of a regular tetrahedron. The resulting three-dimensional network (diamond) is extremely rigid, which is one reason for its hardness. In graphite, sp^2 hybridization occurs, in which each atom is connected evenly to three other atoms (120°) in the xy plane, and a weak π bond is present in the z axis. The sp^2 set forms the hexagonal lattice typical of a sheet of graphite. The p_z orbital is responsible for a weak bond, a van der Waals bond. The spacing between the carbon layers is 3.35 Å. The free electrons in the p_z orbital move within this cloud and are no longer local to a single carbon atom (delocalized).

A new form of carbon, Buckminster fullerene (C₆₀) shown in Fig. 2.1, was discovered in 1985 by a team headed by Korto and co-workers⁵⁰. In this structure, a closed cluster containing precisely 60 carbon atoms represents a unique stability and symmetry. This discovery extended way beyond the confines of academic chemical physics, and marked the beginning of a new era in carbon science⁵¹⁻⁵⁴.

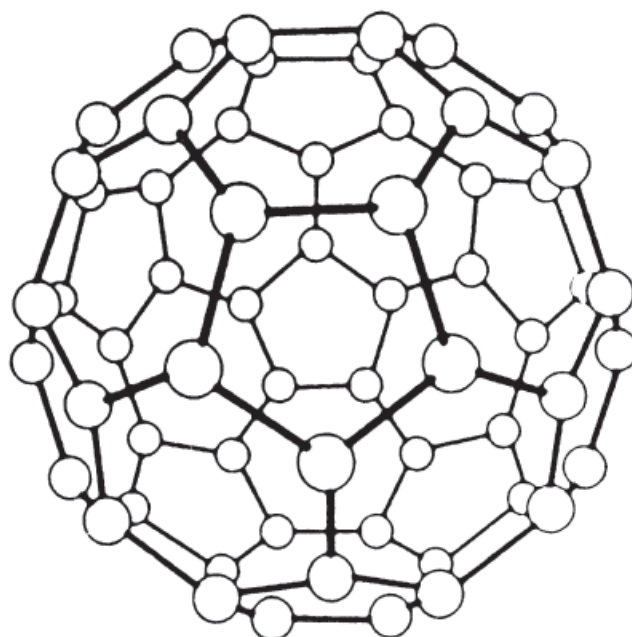


Fig. 2.1. Buckminster fullerene C₆₀

Besides diamond, graphite, and fullerene (C₆₀), one-dimensional nanotubes are considered as another new form of pure carbon. They can be visualized as rolled hexagonal carbon networks that are capped by pentagonal carbon rings. There are two types of carbon tubes: single-wall (SWCNTs)^{55,56} and multi-wall (MWCNTs)⁹.

Possibly the first series of high-resolution transmission electron microscopy (HRTEM) images of CNTs were obtained by Endo in the mid-1970s⁵⁷. The initial idea of his work was to analyse the internal structure of carbon fibres produced by pyrolysis of benzene and ferrocene at 1000 °C, and elucidate their growth mechanism in order to control the bulk production of the fibres. Because of thin specimens needed for HRTEM studies, he changed experimental conditions and thin fibres (<100 nm) were produced. He observed that tubular graphite of nanometer scale could be produced using this thermolytic process, and imaged the first ever-observed SWCNTs and MWCNTs (Fig. 2.2). Unfortunately, this report did not cause a great impact because researchers were more interested in micron-size carbon fibres.

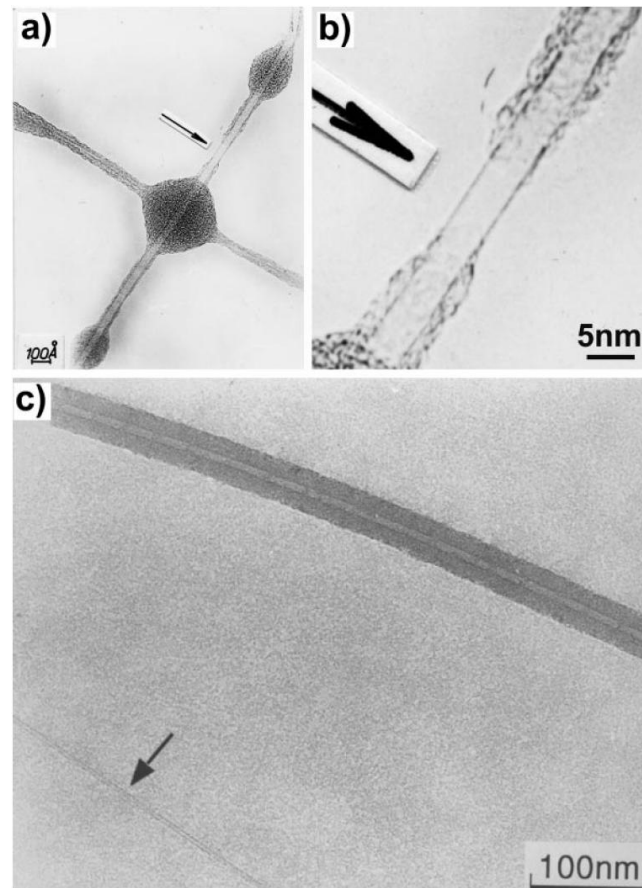


Fig. 2.2. (a) HRTEM image of two crossing SWCNTs coated with amorphous carbon; (b) Higher magnification of (a); (c) HRTEM image showing a MWCNT upper region together with a SWCNT indicated by an arrow.⁵⁷

Sixteen years later, S. Iijima, the electron microscopist of the NEC laboratories in Japan, using HRTEM and electron diffraction, reported the existence of helical carbon microtubules⁹ (now called nanotubes; Fig. 2.3(a)) consisting of nested graphene tubules (Fig. 2.3(b)). This material was generated in an arc-discharge fullerene reactor at low direct current⁹. These concentric tubules exhibited interlayer spacing of ~ 3.4 Å, a value slightly greater than that of graphite (3.35 Å). Iijima associated this spacing difference to a combination of the graphene sheet curvature and weaker van der Waals forces acting between the successive cylinders^{9,59,60}.

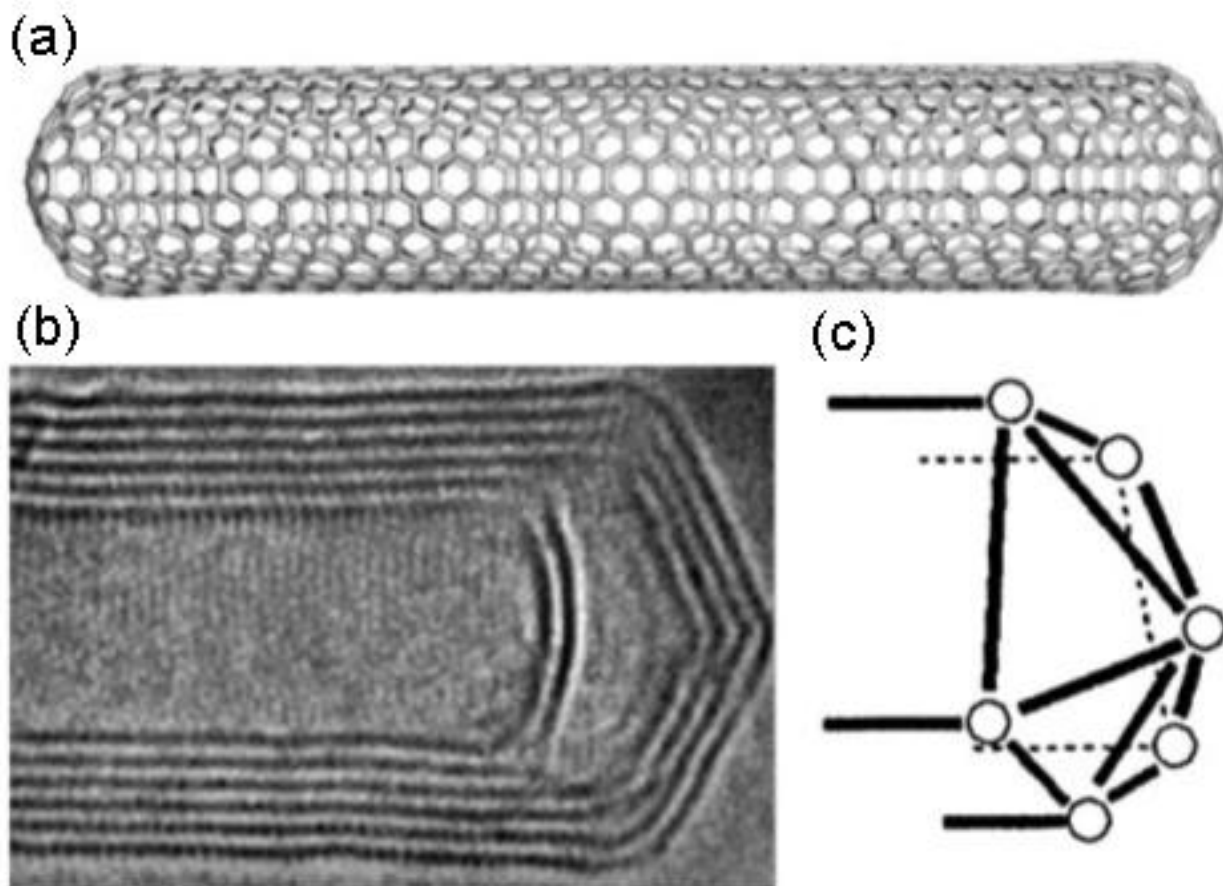


Fig. 2.3. (a) Molecular model of a SWCNT capped by six pentagons in each nanotube end; (b) HRTEM image of one end of a MWCNT; (c) model of a nanotube tip exhibiting the locations of the six pentagonal rings (open circles) that permit the hexagonal carbon lattice (graphene sheet) to close; the model resembles that shown in (b).⁵⁸

Carbon nanotubes are the one of the best examples of novel nanostructures derived by bottom-up chemical synthesis processes. The chemical composition and atomic bonding configuration present in nanotubes is simple, however, these materials represent diverse structure-property relations among the nanomaterials. Nowadays, CNTs can be produced using a wide variety of techniques such as arc-discharge⁶¹, pyrolysis of hydrocarbons over metal par-

ticles⁶², laser vaporization of graphite targets⁶³, solar carbon vaporization⁶⁴, electrolysis of carbon electrodes in molten ionic salts⁶⁵ and chemical vapor deposition⁶⁶.

2.1.1 The structure of carbon nanotubes

It is possible to construct a sp^2 -hybridized carbon tubule theoretically by rolling up a hexagonal graphene sheet and thus lead to “non-chiral” and chiral arrangements. In the non-chiral geometries, the honeycomb lattices, located at the top and bottom of the tube, are always parallel to the tube axis (these configurations are known as armchair and zig-zag). In the armchair structure, two C-C bonds on opposite sides of each hexagon are perpendicular to the tube axis, whereas in the zig-zag arrangement, these bonds are parallel to the tube axis (Fig. 2.4(a) and (b)). All other conformations in which the C-C bonds lie at an angle to the tube axis are known as chiral or helical structures (Fig. 2.4(c)).

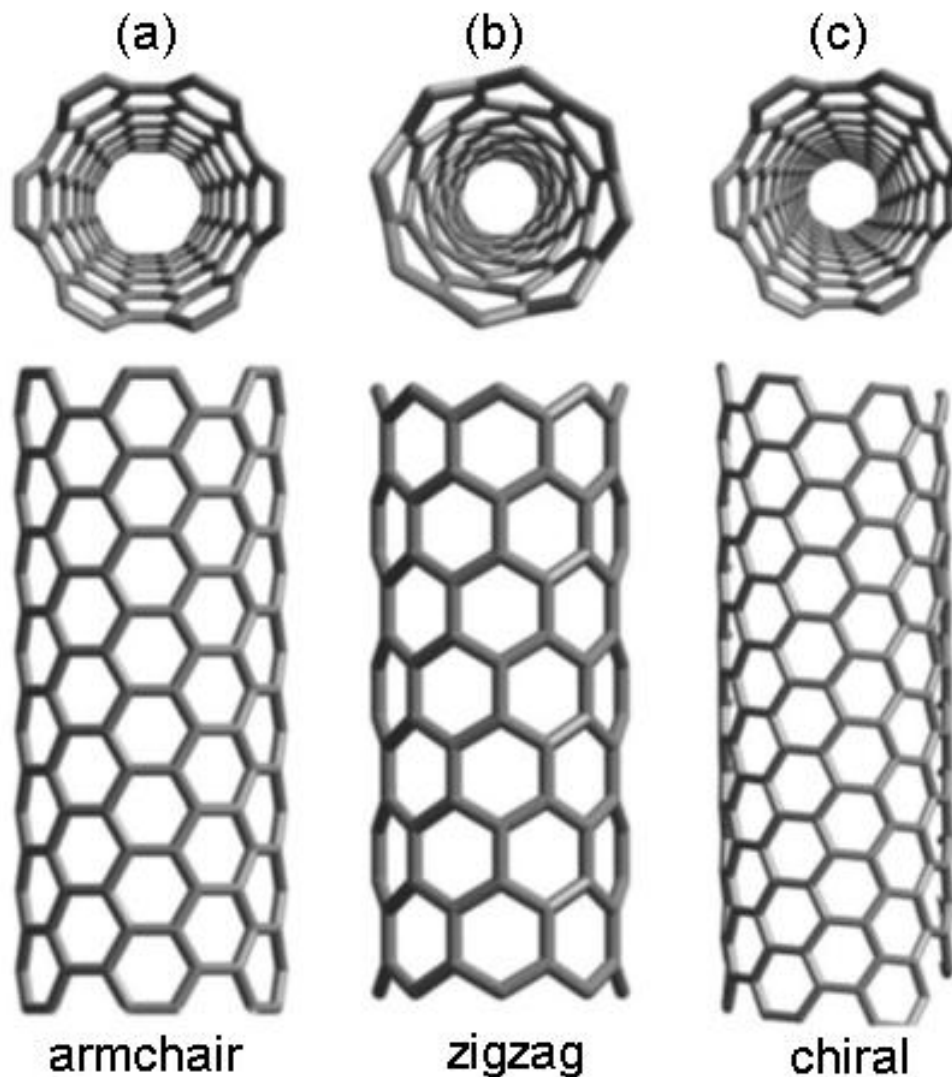


Fig. 2.4. Molecular models of SWCNTs exhibiting different chiralities: (a) armchair configuration, (b) zig-zag arrangement, and (c) chiral conformation.

Mathematically, the tube chirality can be defined in terms of a chiral vector \mathbf{C}_n , joining two equivalent points on the original graphene lattice. The cylinder is produced by rolling up the sheet such that the two end-points of the vector are superimposed. Because of the symmetry of the honeycomb lattice, many of the cylinders produced in this way will be equivalent, but there is an ‘irreducible wedge’ comprising one twelfth of the graphene lattice, within which unique tube structures are defined. Fig. 2.5 shows a small part of this irreducible wedge, with points on the lattice labelled according to the notation of Dresselhaus et al.^{67,68}. Each pair of integers (m, n) represents a possible tube structure. Thus the vector \mathbf{C} can be expressed as

$$\mathbf{C}_n = m\mathbf{a}_1 + n\mathbf{a}_2 \quad (2.1)$$

where \mathbf{a}_1 and \mathbf{a}_2 are the unit cell base vectors of the graphene sheet, and $m \geq n$. In order to determine the armchair and zigzag structure in terms of (m, n) , it is necessary to have the following conditions:

$$(m, n) = (p, 0) \quad (\text{zigzag})$$

$$(m, n) = (2p, -p) \text{ or } (p, p) \quad (\text{armchair})$$

where p is integer. All other tubes are chiral.

The vector also determines the tube diameter d ^{69,70}. The magnitude of \mathbf{C}_n in nanometer is

$$|\mathbf{C}_n| = a\sqrt{m^2 + mn + n^2} \quad (2.2)$$

thus, the diameter of a carbon tubule can be expressed as

$$d = \frac{a\sqrt{m^2 + mn + n^2}}{\pi} \quad (2.3)$$

where $a = 1.42 \times \sqrt{3} \text{ \AA}$ corresponds to the lattice constant in the graphite sheet. Note that the C-C distance is 1.42 \AA for sp^2 -hybridized carbon.

The chiral angle θ (angle between \mathbf{C}_n and the zigzag direction) is defined as

$$\theta = \arcsin\left[\frac{\sqrt{3}n}{2\sqrt{m^2 + mn + n^2}}\right] \quad (2.4)$$

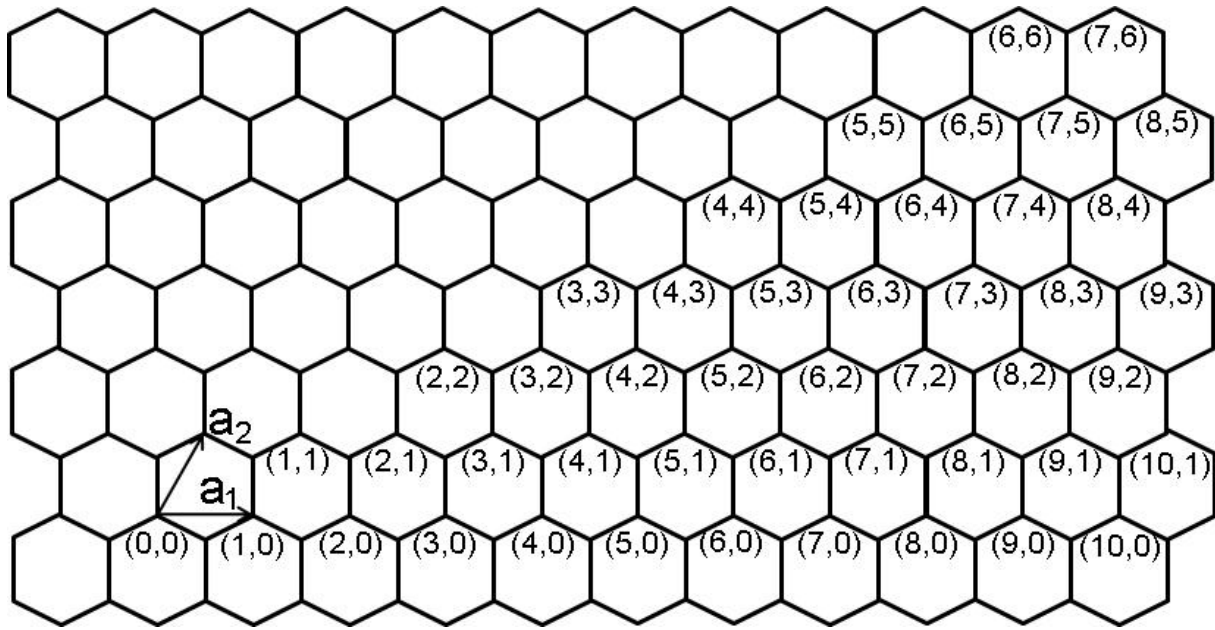


Fig. 2.5. Graphene layer with atoms labeled using (m, n) notation. Unit vectors of the 2D lattice are also shown.

Imaging a nanotube as a ‘one-dimensional crystal’, a translational unit cell can be defined along the tube axis. For all nanotubes, the translational unit cell has the form of a cylinder. Considering again the two archetypal tubes which can be capped by one half of a C₆₀ molecule, the ‘unrolled’ cylindrical unit cells for both of these are shown in Fig. 2.6⁷¹. For the armchair tube, the width of the cell is equal to the magnitude of a , the unit vector of the original 2D graphite lattice, while for the zig-zag tube the width of the cell is $\sqrt{3}a$. Larger diameter armchair and zig-zag nanotubes have unit cells which are simply longer versions of these. For chiral nanotubes, the lower symmetry results in larger unit cells. A simple method of constructing these cells has been described by Jishi, Dresselhaus and colleagues^{67,68,72,73}. This involves drawing a straight line through the origin **O** of the irreducible wedge normal to **C_n**, and extending this line until it passes exactly through an equivalent lattice point. This is illustrated in Fig. 2.7⁷¹ for the case of a (6, 3) nanotube. The length of the unit cell in the tube axis direction is the magnitude of the vector **T**. Expressions can be derived for this in terms of **C_n**, the magnitude of **C_n**, and the highest common divisor of n and m , which we denote d_H ^{68,72}. If

$$m - n \neq 3rd_H$$

where r is some integer, then

$$T = \sqrt{3}|C_n|/d_H \quad (2.5)$$

while if

$$m - n = 3rd_H$$

then

$$T = \sqrt{3}|C_n|/3d_H \quad (2.6)$$

It can also be shown that the number of carbon atoms per unit cell of a tube specified by (m, n) is $2N$ such that

$$N = 2(m^2 + mn + n^2)/d_H, \text{ if } m - n \neq 3rd_H \quad (2.7)$$

and

$$N = 2(m^2 + mn + n^2)/3d_H, \text{ if } m - n = 3rd_H \quad (2.8)$$

These simple expressions enable the diameters and unit cell parameters of nanotubes to be readily calculated. For nanotubes in the diameter range which is typically observed experimentally, i.e. ~2-30 nm, the unit cells can be very large. For example, the tube denoted (80, 67), which has a diameter of approximately 10 nm, has a unit cell 54.3nm in length containing 64996 atoms. These large unit cells can present problems in calculating the electronic and vibrational properties of nanotubes.

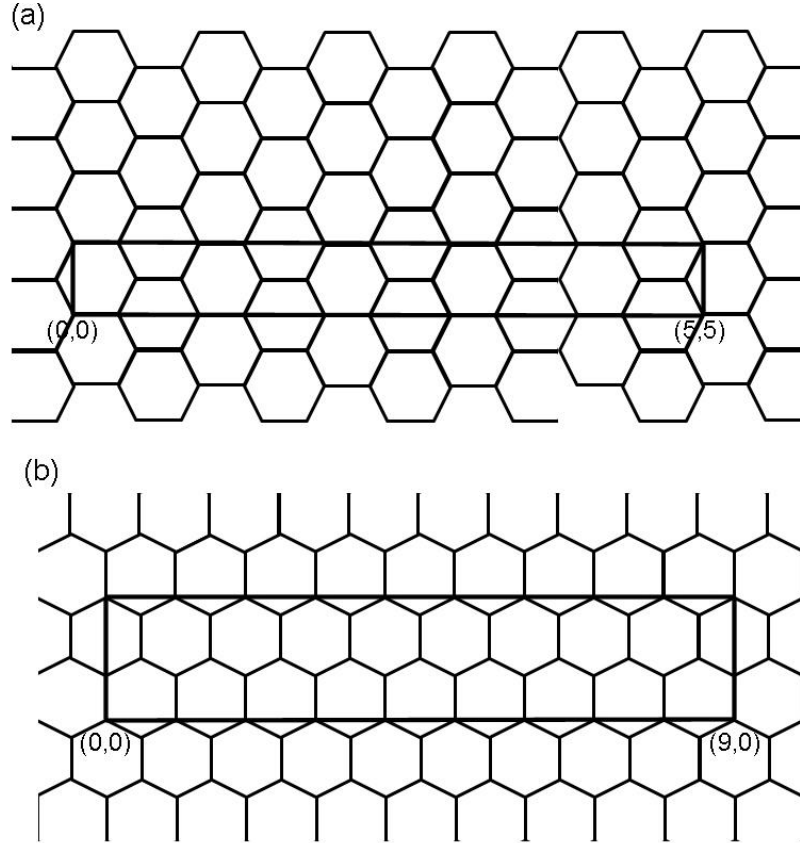


Fig. 2.6. Unit cells for (a) (5, 5) armchair nanotube and (b) (9, 0) zig-zag nanotube.

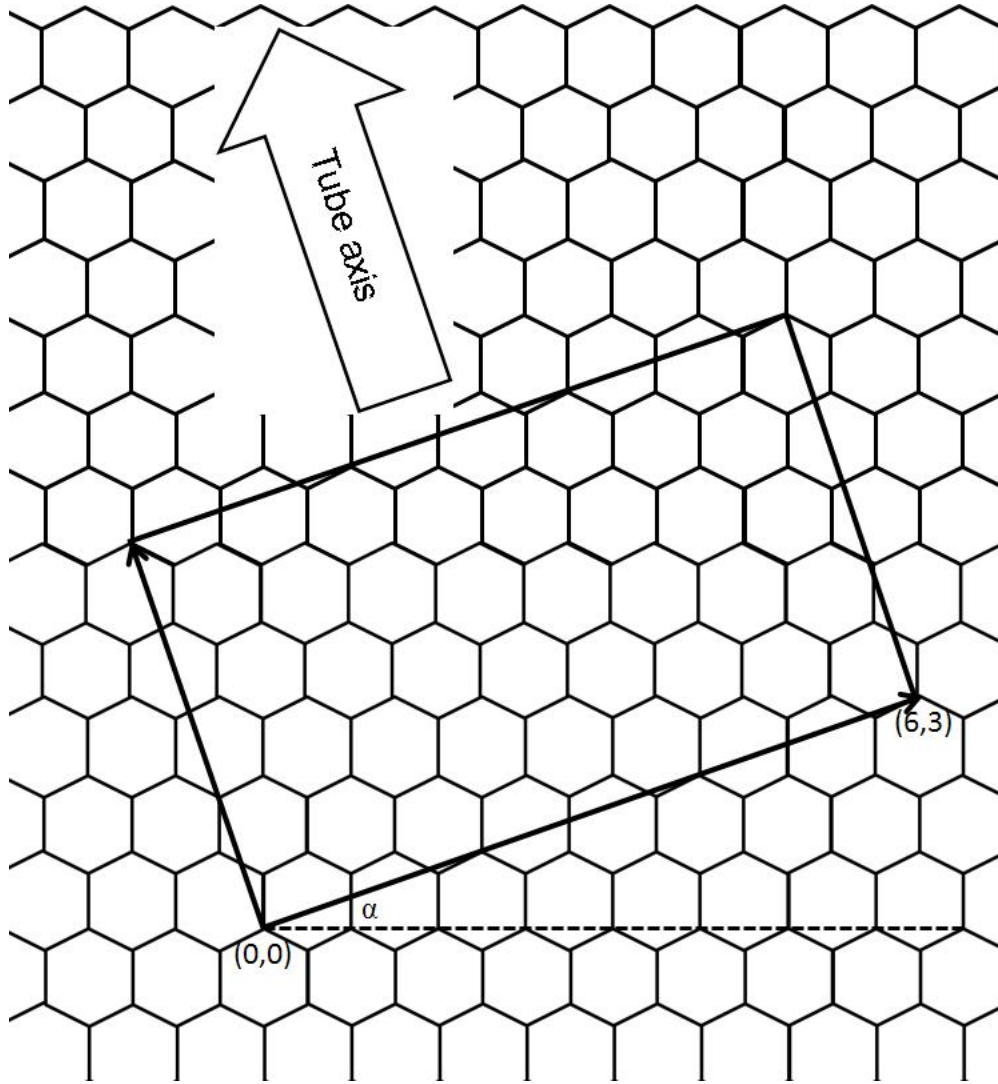


Fig. 2.7. Construction of the unit cell for a (6, 3) nanotube.

2.1.2 Synthesis techniques of carbon nanotubes

A variety of techniques have been developed to produce SWCNTs and MWCNTs with different structure and morphology in laboratory quantities. There are three methods commonly used to synthesize CNT: arc discharge⁶¹, laser ablation⁶³, and chemical vapor deposition (CVD)⁶⁵. The basic elements for the formation of nanotubes are catalyst, a source of carbon, and sufficient energy. The common feature of these methods is addition of energy to a carbon source to produce fragments (groups or single C atoms) that can recombine to generate CNT. The energy source may be electricity from an arc discharge, heat from a furnace or other assisted unit ($\sim 900^\circ\text{C}$) for CVD, or the high-intensity light from a laser (laser ablation).

Electric Arc-Evaporation

Electric arc-evaporation is the ‘classic’ method of preparing multiwall nanotubes, and produces the best quality samples. The optimal conditions for multiwall nanotubes generation

using this technique involve the passage of a direct current (80-100 A) through two high-purity graphite (6-10 mm for outside diameter) electrodes separated by ~1-2 mm, in a He atmosphere (500 Torr)⁶¹. Together with nanotubes, nested polyhedral graphene particles can also be generated meanwhile. In addition to MWCNTs, SWCNTs can also be produced when a metal catalyst is added in the process. The first report on the production of SWCNTs was by Iijima & Ichihashi⁵⁵ through arcing Fe-graphite electrodes in a methane-argon atmosphere. Nowadays SWCNTs can be produced using the carbon arc method in conjunction with different metals such as Gd⁷⁴, Co-Pt⁷⁵, Co-Ru⁷⁵, Co⁷⁶, Ni-Y⁷⁷, Rh-Pt⁷⁸, and Co-Ni-Fe-Ce⁷⁹.

The arc method usually involves high-purity graphite electrodes, metal powders (only for producing SWCNTs), and high-purity He and Ar gases; thus the costs associated with the production of SWCNTs and MWCNTs are high. Although the crystallinity of the material is also high, there is no control over dimensions (length and diameter) of the tubes. Unfortunately, by-products such as polyhedral graphite particles (in the case of MWCNTs), encapsulated metal particles (for SWCNTs), and amorphous carbon are also formed.

Laser Vaporization

High-power laser vaporization (YAG type) of pure graphite targets inside a furnace at 1200 °C, in an Ar atmosphere is capable of generating MWCNTs^{80,81}. The nanotube growth using this technique has been explained in terms of the attachment of incoming carbon species at the edges of adjacent growing graphene tubules, responsible for prolonging the lifetime of the open structure (e.g., lip-lip interactions), which finally results in a multi-layered tube⁶⁵. In order to generate SWCNTs using the laser technique, adding metal particles is also necessary as catalysts to the graphite targets. In this context, Thess et al.⁸² were the first to obtain SWCNT bundles using graphite-Co-Ni targets. But the repeatability is not so good as expected.

Unfortunately, the laser technique is not economically advantageous because the process involves high-purity graphite rods, the laser powers required are high (in some cases two laser beams are required), and the amount of nanotubes that can be produced per day is not as high as the method discussed above.

Chemical Vapor Deposition

Hydrocarbon (e.g., methane, benzene, acetylene, naphthalene, ethylene, etc.) decomposition over metal catalysts (e.g., Co, Ni, Fe, Pt, and Pd deposited on substrates such as silicon, graphite, or silica), is able to produce fullerenes, CNTs, and other fascinating *sp*²-like nanostructures.

Possibly the first record of the production of carbon filaments dates from the nineteenth century, when two French scientists, P. and L. Schuetzenberger, described the formation of carbon microfilaments⁸³ by passing cyanogen over porcelain at “cherry red” heat. Unfortunately, at that time, it was impossible to observe nanometer-scale structures; however, it is highly likely CNTs and associated nanostructures were produced. At present, mechanisms that account for the formation of carbon filaments via pyrolytic approaches are explained as follows:

- a) Top carbon diffusion through catalytic particles;
- b) Top carbon diffusion on catalytic particles;
- c) Bottom carbon diffusion through catalytic particles.

MWCNTs can be considered hollow carbon filaments that are highly crystalline, in which the graphitic (002) planes lie parallel to the tube axis. And carbon segregates preferentially on selected faces of the metal particle⁸⁴. For example, the Fe particle is oriented with its (100) axis along the filament axis, whereas Fe-Co or Fe-Ni alloys prefer the (110) orientation^{57,84}. However, carbon diffusion parameters depend critically on the dimensions of the particles, the transition metal characteristics of the metal used as catalyst, temperature, and the hydrocarbon and gases involved in the process. Therefore, graphite planes can grow parallel to the exterior filament planes and a hollow core can be formed⁸⁵.

It is also possible to generate SWCNTs via CVD methods. In this context, Dai et al.⁸⁶ reported the generation of SWCNTs via thermolytic processes involving Mo particles in conjunction with CO (CO disproportionation) at 1200 °C. It is clear that CVD processes will be used in the future to grow large quantities of pure and crystalline SWCNTs. But there may not be a unique growth mechanism for the production of carbon filaments and nanotubes using the hydrocarbon decomposition at elevated temperatures. By changing the parameters such as type of hydrocarbon, metal catalysts, particle size, carrier gases, and temperature, different filaments possessing various morphologies and degrees of graphitization can result. However, any pyrolysis experiment in the presence of a transition metal could lead to the formation of tubular structures.

2.1.3 Growth Mechanism of Carbon Nanotubes

Compared with the arc-evaporation and laser vaporization processes, CVD process requires much lower temperatures, thus seems to be more adapted for large-scale production at lower cost, attracting many research groups all over the world working on the growth of

CNTs by CVD. However, the ability to grow CNTs directly on a substrate at a desired position is a great challenge from a technological point of view. The control over the catalytic chemical vapor deposition (CCVD) growth of CNTs could be a solution solving with this challenge. This technique would permit the integration of the CNT growth into fabrication processes of microelectronic circuits.

Metals used to catalyse CNT formation are most often transition metals, in particular iron, cobalt and nickel. A very large number of papers can be found in the literature reporting CNT growth. Most of the papers available in the literature about growth of CNTs on iron based catalysts report growth of MWCNTs⁸⁷⁻¹⁰⁹. Many groups also obtained SWCNTs¹¹⁰⁻¹¹⁹. Most of the reported results obtained with cobalt-based catalysts concern formation of MWCNTs^{92,94,95,103,104,119-127}, a few others SWCNTs^{119,128-130}. Nickel-based catalysts generally lead to MWCNTs^{92,123,131-144}, seldom to SWCNTs^{129,130,145}. Mixtures of transition metals are often observed to be more efficient for CNT production than one metal alone. Iron-nickel alloys are found to produce MWCNTs¹⁴⁶⁻¹⁴⁸, iron-cobalt alloys seem to produce rather SWCNTs¹⁴⁹⁻¹⁵³ and Dai et al. obtained SWCNTs with a nickel-cobalt alloy¹⁵⁴. Other authors studied several alloy catalysts and mainly obtained SWCNTs^{87,129,130,155,156}. Palladium seems to be an interesting metal for connecting carbon nanotubes since the contact between this metal and metallic CNTs is ohmic in nature¹⁵⁷. The catalyst nanoparticle would therefore not disturb the electronic transport properties of the nanotube by forming a Schottky barrier. Nevertheless, palladium has been used a little as a catalyst for CNT formation, as described in references 158-160. These three papers report growth of MWCNTs. Other metals than iron, cobalt, nickel or palladium have been used as cocatalyst. These metals are generally but not necessarily non-active catalysts alone but at any rate are used to improve the performance of the “classical” catalysts when added to them in different quantities. Molybdenum is the most important, added to Fe¹⁶¹⁻¹⁷¹ or to Co¹⁷²⁻¹⁸². Except for in reference 180, all these papers report formation of SWNTs with iron-molybdenum or cobalt-molybdenum catalysts. Magnesium-nickel oxides have been used as catalysts for MWCNT growth¹⁸³⁻¹⁸⁵ and magnesium-cobalt oxides for SWCNT growth^{182,186,187}.

The CVD process on a supported catalyst consists of several steps. The first is to prepare metal nanoparticles on a substrate. The substrate is then placed in a furnace and the nanoparticles are then generally submitted to a reduction treatment upon heating under typically H₂ or NH₃. And finally, hydrocarbon gas or CO is let into the furnace and carbon deposition occurs by catalytic decomposition of the hydrocarbon molecules on the metal nanoparticles by temperatures ranging roughly from 500 to 1200 °C.

The growth process may be quite different in the CVD process compared with the arc-evaporation and laser vaporization methods. Because of the analogy between CNTs grown by CVD on a supported catalyst and carbon filaments grown also by CVD on a supported catalyst, the growth model for carbon filaments will be firstly discussed.

The carbon filament growth model generally adopted is based on the concepts of the VLS (vapor-liquid-solid) theory developed by Wagner and Ellis¹⁸⁸. In this model, molecular decomposition and carbon solution are assumed to occur at one side of the catalytic particle, which then becomes supersaturated¹⁸⁹. Carbon diffuses from the side where it has been decomposed to another side where it is precipitated from solution¹⁹⁰. It is not clear at this point of the model which is the driving force for carbon diffusion within the catalytic particle. For many authors, this force originates from the temperature gradient created in the particle by exothermic decomposition of the hydrocarbon at the exposed front faces and endothermic deposition of carbon at the rear faces, which are initially in contact with the support face^{190,191}. Others ascribed the driving force to a concentration gradient^{189,192}. However, because of a much lower surface energy of the basal planes of the graphite compared with the prismatic planes, it is energetically favourable for the filament to precipitate with the basal planes as the cylindrical planes¹⁸⁹. The metal-support interactions are found to play a determinant role for the growth mechanism^{162,190}. Weak interactions yield tip-growth mode whereas strong interactions lead to base-growth. Both growth modes are schematically shown in Fig. 2.8.¹⁹³

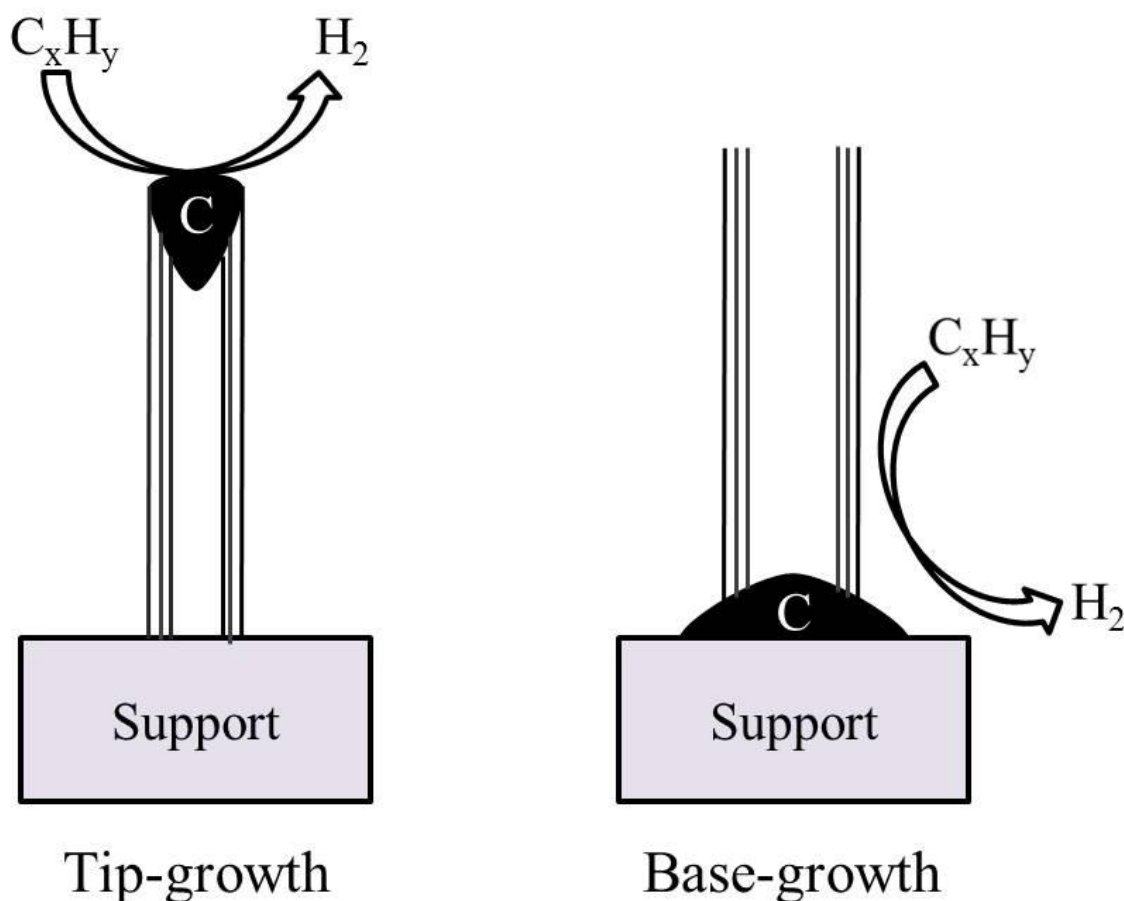


Fig. 2.8. The two growth modes of filamentous carbon.

This growth model for carbon filaments has been widely used for carbon nanotubes. However, the specificity of the growth of nanotubes on nanoparticles with regard to the growth of carbon filaments is their nanometer dimensions. The energetic argument of the precipitation of carbon on its low-energy basal planes is for example no longer valid since the curving of the graphite layers introduces an extra elastic term into the free-energy equation of nucleation and growth, leading to a lower limit of about 10 nm ¹⁸⁹. Other mechanisms are therefore necessary to explain the growth of CNTs, whose diameter can be much smaller than this lower size limit¹⁹⁴. In the catalytic growth of CNTs, not the “fluid nature” of the metal particle as in the VLS model has to be considered but the chemical interactions between the transition metal 3d electrons and the p carbon electrons¹⁹⁵. Nanoparticles exhibit a very high surface energy per atom. The carbon in excess present during CVD process could solve this energetic problem by assembling a graphene cap on the particle surface with its edges strongly chemisorbed to the metal. Since the basal planes of graphite have an extremely low surface energy, the total surface energy diminishes. This is the Yarmulke mechanism proposed by Dai et al.¹⁵⁴. The hemifullerene cap so formed on the partially carbon-coated particle lifts off and

additional carbon atoms are continuously added to the edge of the cap, forming a hollow tube with constant diameter which grows away from the particle¹¹³. The driving force for the lifting process is believed to originate from the free energy release due to relaxation of the strain built up in the carbon cap around the spherical surface of the catalyst nanoparticle when carbon fragments assemble to form a CNT^{145,196}.

Growth of SWCNTs in the arc-discharge and laser-ablation methods has been already widely discussed from a theoretical point of view. Molecular dynamics and total energy calculations revealed the basic atomic process by which single shelled nanotubes can grow out of metal-carbide particles by the root growth mechanism¹⁹⁷. In contrast, almost no theoretical work could be found on the CCVD growth of CNTs until the recent publication of Shibuta and Maruyama¹⁹⁸. The authors performed molecular dynamics simulation of SWCNT growth by CCVD and showed that carbon atoms are absorbed into the metal cluster until saturation to make a hexagonal network of carbon atoms inside the surface of the cluster. Further supply of carbon then leads to a separation of the carbon network from the metal surface itself. Furthermore, carbon atoms inside the supersaturated nickel cluster gradually lift up the carbon-shell. This described process can be regarded as an initial stage of the growth process of SWCNT and at any rate confirms the Yarmulke mechanism proposed by Dai et al.¹⁵⁴.

Another paper from Helveg et al.¹⁹⁹ deals with a high-resolution *in situ* transmission electron microscope observation of catalytic tip-growth of CNTs by decomposition of methane over a nickel-based catalyst. The nickel particles are observed first to elongate with simultaneous formation of graphene sheets with their basal planes oriented parallel to the nickel surface. A contraction follows, explained by the fact that the increase in the nickel surface energy can no longer be compensated for by the energy gained when binding the graphitic tube to the nickel surface. This study furthermore reveals that monoatomic steps are present at the nickel surface and that a graphene sheet terminates at each of these steps. Between a pair of such step edges, an additional graphene layer grows as the nickel steps move towards the ends of the nickel cluster and vanish, involving transport of carbon atoms towards and nickel atoms away from the graphene-nickel interface. Note that this proposed growth process, confirmed with density-functional theory calculations performed by the authors, concerns a tip-growth mechanism. It therefore is not really surprising that it clearly differs from the Yarmulke mechanism presented above, valid for base-growth processes.

2.1.4 Theory for determination of the chiral indices (m, n) of carbon nanotubes

In order to determine the atomic structure of a carbon nanotube, it is necessary to determine the chiral indices (m, n) that in turn determine the diameter and chirality of the nanotube. Traditionally, using transmission electron microscopy, the diameter has been measured directly from high-resolution electron micrographs and the chirality is deduced from the electron diffraction patterns.

In the present work we utilize a convenient method to determine the chiral indices (m, n) firstly proposed by L. Qin²⁰⁰. On the electron diffraction pattern of a single-walled carbon nanotube, the primary graphene reflections of Miller indices (10), (01), (11), (-10), (0-1), and (-1-1), are of the strongest intensity. These reflections form three pairs of layer lines (three layer lines above the equatorial line and three below the equatorial line), labeled l_1 (formed by the graphene (01) reflections), l_2 (formed by the graphene (-10) reflections) and l_3 (formed by the graphene (11) reflections) with respective layer line spacings D_1 , D_2 , and D_3 relative to the equatorial layer line. These three pairs of layer lines are referred to as the principal layer lines and are schematically illustrated in Fig. 2.9. It is experimentally most convenient to use these principal layer lines to characterize the carbon nanotube. Due to the very small diameter of carbon nanotubes, the diffraction peaks are elongated perpendicular to the tubule axis and only reflections close to the meridian have significant intensities. In some cases, the reflections (1-1) and (-11) are also used, which will be referred to in this article as layer line l_4 with layer line spacing D_4 .

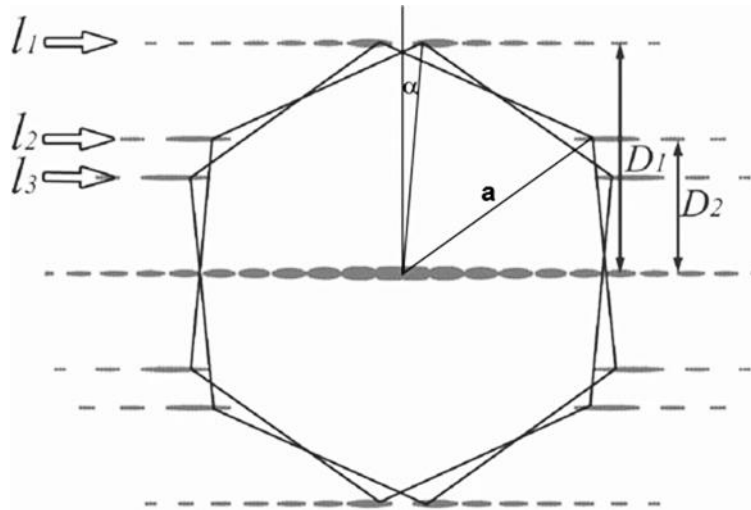


Fig. 2.9. Schematic diffraction pattern of a carbon nanotube of helical angle α —the layer line spacings D_1 , D_2 , etc are not affected by the curvature of the nanotube. Spotty graphene reflections become streaks elongated in the directions perpendicular to the tubule axis.²⁰⁰

It is important to note that on each layer line, there is usually only one order of Bessel function that dominates the intensity distribution on this particular layer line. All the others contribute negligibly to the layer line intensity. The order of the single operating Bessel function for a given carbon nanotube (m, n) can be obtained by considering the crystallographic indices of the graphene reflections using the extended cell of the nanotube in radial projection which is related to the index u . And the index u has a relationship with (m, n) as follows:

$$u = hm + kn, \quad (2.9)$$

where h and k refer to the concerned graphene reflection (hk).

As shown in Fig. 2.9, the three principal layer lines l_1 , l_2 and l_3 are formed by graphene reflections (01), (-10) and (11), respectively. When choosing the reference graphene reflection as (01), i.e. $h = 0$ and $k = 1$, the order of the dominating Bessel function is

$$u = n, \quad (2.10)$$

for graphene reflection (-10)

$$u = -m, \quad (2.11)$$

and for graphene reflection (11)

$$u = m + n. \quad (2.12)$$

Therefore, the contributing Bessel functions to the three principal layer lines are of orders n , $-m$ and $m + n$, respectively.

Therefore, the reflection intensities of the three principal layer lines l_1 , l_2 and l_3 are related to the chiral indices m and n by

$$I_{l1}(R) \propto |J_n(\pi dR)|^2, \quad (2.13)$$

$$I_{l2}(R) \propto |J_m(\pi dR)|^2, \quad (2.14)$$

and

$$I_{l3}(R) \propto |J_{m+n}(\pi dR)|^2, \quad (2.15)$$

where $J_u(X)$ refers to the order u of Bessel function.

$J_u(X)$ can be determined by examining the positions of its peaks, which are unique to each Bessel function. An efficient and convenient means to determine the order u of Bessel function $J_u(X)$ is to examine the ratio X_2/X_1 of the positions of its first two peaks located at X_1 and X_2 , respectively, or any other pair of peaks unique to this Bessel function. Once the orders

of the respective Bessel functions are determined, the chiral indices, m and n , are obtained directly. The chiral indices (m, n) can therefore be obtained directly by determining the order of Bessel functions $J_n(X)$ and $J_m(X)$ with $X = \pi dR$ from the scattering intensity distribution on layer lines l_1 and l_2 , whose intensities are proportional to $|J_n(\pi dR)|^2$ and $|J_m(\pi dR)|^2$, respectively. On the experimental diffraction pattern, the positions of the first two peaks, R_1 and R_2 , can be measured and the ratio $R_2/R_1 = X_2/X_1$ is independent of the camera length of the electron microscope at which the electron diffraction pattern is acquired.

This method allows a rapid and accurate assignment of the chiral indices (m, n). From the ratios $R_2/R_1 = X_2/X_1$ measured directly from the electron diffraction pattern, the indices m and n can be obtained from the tabulated values given in Table 2.1²⁰⁰. Using this method, the peak positions with a precision of 0.3% can be obtained, allowing to assign the chiral indices unambiguously up to index 30 or nanotube diameter up to 4 nm.

For non-helical nanotubes, i.e. zigzag and armchair nanotubes with chiral indices ($m, 0$) and (m, m), respectively, overlap of the principal layer lines occurs. For a zigzag nanotube of indices ($m, 0$), layer lines l_2 and l_3 overlap with each other and its first principal layer line l_1 has intensity distribution proportional to $|J_0(\pi dR)|^2$ and the second layer line l_2 has intensity proportional to $|J_m(\pi dR)|^2$. For an armchair nanotube (m, m), the first layer line l_1 and the second line l_2 overlap with intensities proportional to $|J_m(\pi dR)|^2$ and layer line l_3 falls on the equatorial line.

Table 2.1. Ratio of the second and the first peak positions of Bessel functions.

n	X_2/X_1	n	X_2/X_1	n	X_2/X_1
1	2.892	11	1.373	21	1.239
2	2.197	12	1.350	22	1.232
3	1.907	13	1.332	23	1.226
4	1.751	14	1.315	24	1.218
5	1.639	15	1.301	25	1.211
6	1.565	16	1.287	26	1.206
7	1.507	17	1.275	27	1.201
8	1.465	18	1.266	28	1.196
9	1.428	19	1.256	29	1.192
10	1.398	20	1.247	30	1.188

Since the atomic structure of carbon nanotube (m, n) is periodic in the axial direction, the layer lines are sharp and the respective layer line spacings D_1 , D_2 and D_3 can be measured accurately from the electron diffraction pattern. Although the cylindrical curvature of the

nanotube causes severe distortion to the otherwise hexagonal electron diffraction pattern, the layer line spacings will not change due to the cylindrical curvature. The axial distances to the equatorial line of the fundamental reflections that give rise to the principal layers lines can be calculated using the trigonometric relations illustrated in Fig. 2.9:

$$D_1 = a \times \sin(90^\circ - \alpha) = a \times \cos \alpha, \quad (2.16)$$

$$D_2 = a \times \sin(30^\circ + \alpha), \quad (2.17)$$

then the helical angle α can be deduced from the ratios of the layer line spacings

$$\alpha = \tan^{-1}\left(\frac{2D_2 - D_1}{\sqrt{3}D_1}\right), \quad (2.18)$$

and the ratio of the chiral indices m and n is given by

$$\frac{n}{m} = \frac{2D_2 - D_1}{2D_1 - D_2}. \quad (2.19)$$

Equation (2.19) offers the convenient method to determine the chiral indices (m, n) for the following reasons:

- a) The ratio is independent of the camera length at which the electron diffraction pattern is taken.
- b) The ratio is independent of the relative orientation between the nanotube and the incident electron beam.
- c) When the signal/noise ratio is low, this ratio can still be conveniently obtained.

The use of equation (2.19) can result in a very high accuracy. The indeterminacy arising from the uncertainties leads to only the nanotube of the smallest diameter (m_0, n_0) . Other nanotubes meeting the same equation have chiral indices that are multiples of (m_0, n_0) , i.e. $(m, n) = (um_0, un_0)$, where $u = 1, 2, 3 \dots$. All the possible n/m ratios for chiral indices (m, n) up to (30, 30) are listed in Appendix I at the back of this thesis.

2.2 Silicon nitride nanomaterials

Silicon nitride has been researched intensively for more than 40 years, largely in response to the challenge to develop internal combustion engines with hot-zone components made entirely from ceramics. The ceramic engine programs have had only partial success, but this research effort has succeeded in generating a degree of understanding of silicon nitride and of its processing and properties, which in many respects is more advanced than of more widely used technical ceramics.

2.2.1 Structure of silicon nitride

Early discussions concerned the composition of the compound obtained by heating mixtures of SiO_2 and carbon or by silicon alone in nitrogen: SiN_2 , Si_2N_2 , and Si_3N_4 were proposed²⁰¹ as formulas, with 'normal' Si_3N_4 being shown to have 3:4 stoichiometry. There are two major ceramic forms of this material (reaction bonded and sintered) as well as the often overlooked, but extremely important, amorphous form normally used as a thin film. Each form has its own characteristic production routes, compositions, microstructures, and properties, and underlying all the forms are the fundamental physical and chemical properties of the basic structural unit itself, Si_3N_4 , which, at the atomic and unit-cell levels, provides the basis for many of the bulk property values.

Detailed X-ray diffraction (XRD) examinations in the mid-1950s proved the existence of two crystallographic modifications (α and β), both appearing to be hexagonal²⁰². The c-axis dimension of the unit cell of the α phase was approximately twice that of the β phase, with the phenacite (Be_2SiO_4) structure, in which Be is replaced by Si and O by N. Therefore, there is nothing unusual in nitrides having crystal structures based on those of the oxides²⁰³. Each silicon was at the centre of a tetrahedron, and each nitrogen in trigonal and approximately planar coordination by three silicons, so as to link three SiN_4 tetrahedra. The structures also can be regarded as puckered eight-membered Si-N rings joined to form sheets, which are, in turn, linked by bridging Si-N bonds (Fig. 2.10).

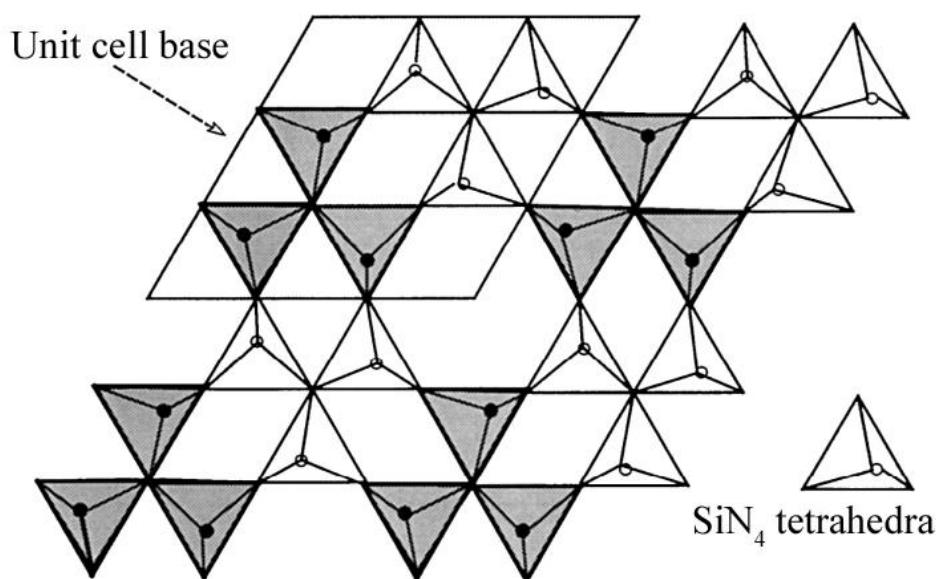


Fig. 2.10. Outline of Si_3N_4 crystal structure.²⁰⁴

The unit cell of $\beta\text{-Si}_3\text{N}_4$ consists of Si_6N_8 , which Hardie and Jack assigned to space group $P6_3/m$ ²⁰⁵, shown in Fig. 2.11. The structure of $\alpha\text{-Si}_3\text{N}_4$ was determined to be closely related to that of $\beta\text{-Si}_3\text{N}_4$, consisting of alternate basal layers of $\beta\text{-Si}_3\text{N}_4$ and a mirror image of $\beta\text{-Si}_3\text{N}_4$, accounting for the doubled c -axis dimension, and a unit-cell composition $\text{Si}_{12}\text{N}_{16}$ (space group $P3_1c$) (Fig. 2.12). However, although the β structure was almost strain free, the α structure contained considerable strain, expressed by lattice distortion and the displacement of atoms from the idealized positions²⁰⁶. A further feature of the two structures is that the larger voids in each basal sheet created by the linking of six eight-membered Si-N rings align in the β structure to provide a continuous c -axis channel of approximate diameter (0.3 nm), whereas, in the α structure, because of the operation of a c glide plane, the continuous voids are interrupted to form a series of large interstices, linked by 0.14 nm diameter tunnels. Later electron diffraction work on thick samples of $\beta\text{-Si}_3\text{N}_4$ ²⁰⁷ suggested that the three silicon atoms coordinating $\text{N}2(c)$ sites were not exactly coplanar, and the space group was probably $P6_3$. Neutron time-of-flight studies¹⁹² subsequently suggested that, at higher temperatures (to 1000 °C), the regular tetrahedra were unchanged, but the irregular became more uniform.

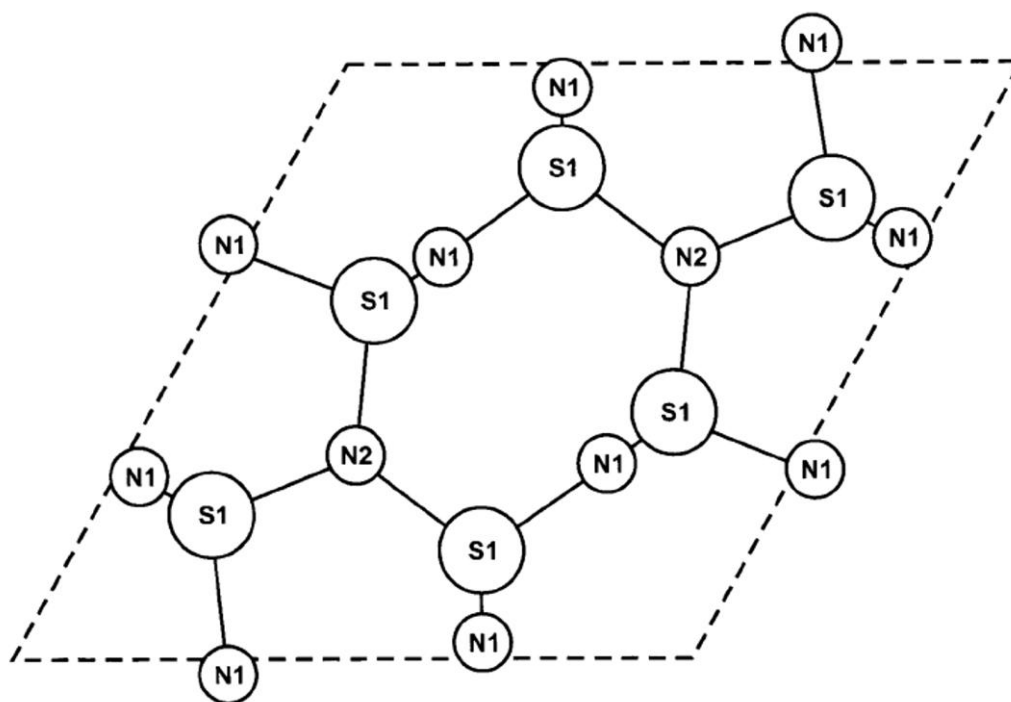
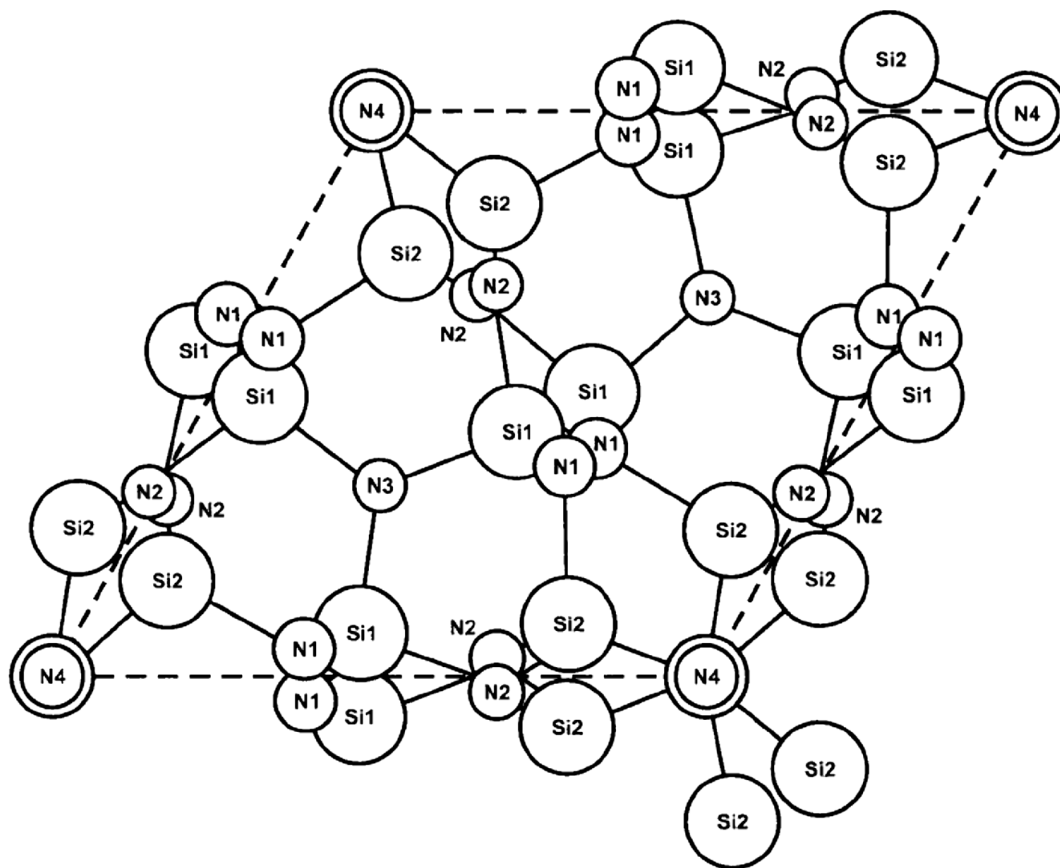


Fig. 2.11. $\beta\text{-Si}_3\text{N}_4$ unit cell²⁰⁹.



*Fig. 2.12. $\alpha\text{-Si}_3\text{N}_4$ unit cell.*²⁰⁹

2.2.2 Morphologies of silicon nitride nanomaterials

Being a hard and strong ceramic material and possessing excellent properties, silicon nitride can be applied to many areas. Pure Si_3N_4 or Si_3N_4 -based materials exhibit improved tribological performance and mechanic properties²¹⁰⁻²¹² characterized by low frictional coefficient, high wear resistance and high strength, fracture toughness, and high flexibility. On the other hand, due to its wide band gap and chemical stability, Si_3N_4 can be used to grow quantum well structures to obtain blue lasers²¹³. Their infrared absorption rate and coercivity can be applied to optics and magnetics^{214,215}. Si_3N_4 nanomaterials should be potentially applied to strengthening and resistance to abrasion as well as the finest fabric additives by incorporation into ceramic, plastic matrix, or fabrics. Recent research has verified that the strength and ductility of nanostructured ceramics and nanosized whiskers are greater than that of micro-sized materials^{216,217}.

Much research has focused on the synthesis of 1D Si_3N_4 nanostructures. Various 1D pure Si_3N_4 nanostructures, such as nanosaws²¹⁸, network-like branched nanostructures²¹⁸, nanobelts²²⁰, nanowires²²¹, and nanodendrites²²² could be obtained by using various methods, in-

cluding catalyst-assisted pyrolysis of polysilazane²²³, vapor-solid (VS) thermal reaction²²⁴, and so forth²²⁵⁻²³¹.

$\alpha\text{-Si}_3\text{N}_4$ nanosaws

Fig. 2.13 (A) and (B) show the SEM images of the $\alpha\text{-Si}_3\text{N}_4$ nanosaws deposited about 7 cm away from the source material. From these images, it is clear that the most dominant morphology found in the as-grown sample is the saw-shaped nanoribbons. The $\alpha\text{-Si}_3\text{N}_4$ nanosaws have one flat side and one sharp, teethlike side instead of two flat sides. The thickness of a typical nanosaw is about 90 nm, as shown in the inset of Fig. 2.13(B). These interesting $\alpha\text{-Si}_3\text{N}_4$ nanosaw structures were further investigated by using TEM; the corresponding images are shown in Fig. 2.13(C)-(F). From these images, it can be seen that the width of the nanosaws is about 3-5 μm . The nanosaws are almost transparent as the copper grid can even be seen through several thin nanosaws. The tips of the nanosaws are flat and no particles were found attached to the tips, indicating that the vapor-liquid-solid (VLS) process may not be the dominant growth mechanism for the growth of $\alpha\text{-Si}_3\text{N}_4$ nanosaws. The apparent ripple-like contrast in the TEM images is due to the strain resulting from the ribbon bending. The ribbon-shaped structures can also be clearly seen in the inset of Fig. 2.13(E). The inset of Fig. 2.13(F) is the corresponding selected-area electron diffraction (SAED) pattern of the nanosaw shown in Fig. 2.13(F). The SAED pattern was obtained from the [100] zone axis of the $\alpha\text{-Si}_3\text{N}_4$ nanosaws, which corresponds to the nanobelt grown along the [011] direction. Upon careful checking of several tens of nanosaws it was found that all the $\alpha\text{-Si}_3\text{N}_4$ nanosaws have a unique growth along the [011] direction.

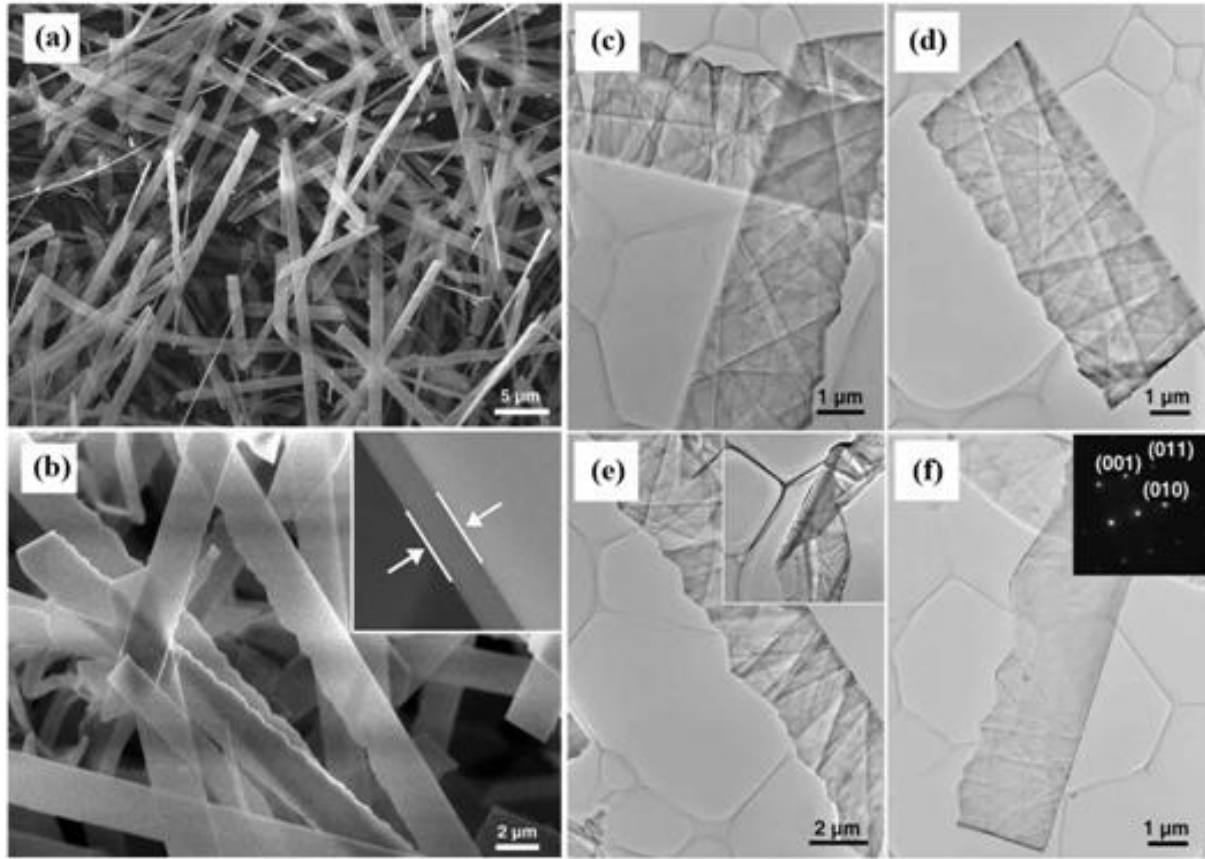


Fig. 2.13. (a) Low-, (b) high-magnification SEM images and (c)-(f) TEM images of as-grown α - Si_3N_4 nanosaws. The upper right inset in (b), (e) and (f) show the typical thickness of a nanosaw, the ribbon shape and the SAED pattern, respectively.²¹⁸

Network-like branched nanostructures

Fig. 2.14 shows two typical SEM images of the as-prepared network-like branched nanostructure. The low-magnification SEM image in Fig. 2.14(a) reveals that the nanonetworks can be prepared in mass production, which is essential in industrial application for such materials. The high-magnification SEM image in Fig. 2.14(b) clearly displays that the nanostructures are interconnected with each other to form nanonetworks, and these networks can construct more complicated nanostructures by multi-layer stack. The diameters of each linear part of the network-like nanostructure varied in the range of 150~400 nm, and most of the junctions are connected through three branches or more. From Fig. 2.14(b), one can also see some nanoparticles on the surfaces of the nanostructures (see the circled spots), which were confirmed to be Fe-rich nanoparticles by SEM-EDX and TEM-EDX, indicating that the growth of the nanostructures was controlled by vapor-liquid-solid (VLS) mechanism.

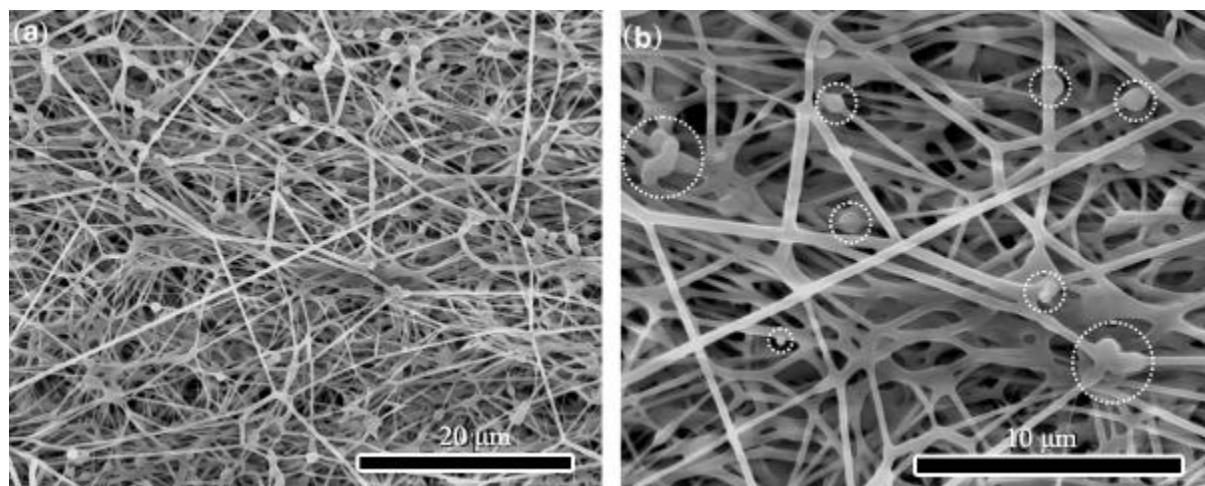


Fig. 2.14. (a) Low- and (b) high-magnification SEM images of the as-prepared network-like branched Si_3N_4 nanostructures. The circled spots are Fe-rich nanoparticles.²¹⁹

Nanobelts

Fig. 2.15 (a) shows a representative SEM image of the pyrolyzed products, showing that relatively high density nanobelts have grown homogeneously on the top of the powder matrix. Closer examinations under high magnification (Fig. 2.15(b) and (c)) reveal that the cross-sections of the Si_3N_4 nanostructures are rectangular, 50-100 nm in thickness and 400-1000 nm in width. The lengths of the belts range from a few 100 nm up to several millimetres. Within each individual belt, the thickness and width are uniform along its entire length. The SEM observation also reveals that the surfaces of the belts are smooth and clear without any particles. Most of the nanobelts are highly curved, suggesting they are flexible. Fig. 2.15(d) shows typical image of the tips of the belts. It can be seen from the image that (i) liquid droplets, which are associated with vapor–liquid–solid (VLS) growth process, are not found at the tips; and (ii) the tips take on a triangular shape, suggesting a significant growth along the width direction at the earlier stage.

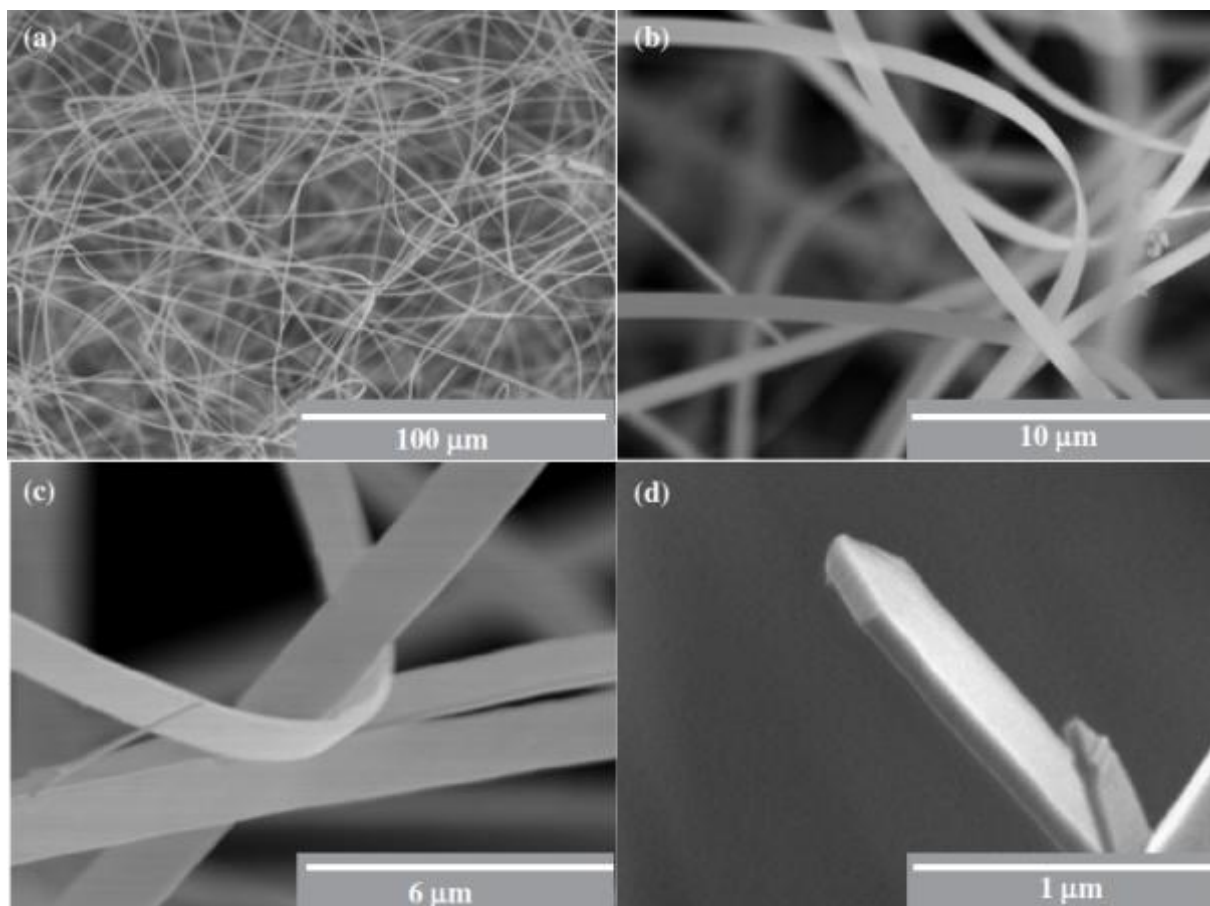


Fig. 2.15. SEM images of Si_3N_4 nanobelts: (a) the morphology under low magnification; (b) and (c) show cross section of the nanobelts; (d) shows (i) there are no liquid droplets on the tips of the belts and (ii) the tips take on a triangular shape.²²⁰

Nanowires

Fig. 2.16 (a) and (b) are the optical images of the products. It is seen that the wires are very long, up to several centimetres (Fig. 2.16(a); the wires are detached from the graphite sheet), and are well aligned along the direction perpendicular to the graphite sheet (Fig. 2.16(b)). This is the longest Si_3N_4 wires have been grown in an aligned manner so far. Fig. 2.16(c)-(f) are typical SEM images of the obtained products under different magnifications. These images reveal that (i) the wires are well aligned (Fig. 2.16(c) and (d)); (ii) the wires exhibit a cylindrical shape (Fig. 2.16(e) and (f)); (iii) the diameters of the wires are narrowly distributed around 200 nm and within each individual wire the diameter is uniform along its entire length; and (iv) the surfaces of the wires are smooth and clean, without any attached particles.

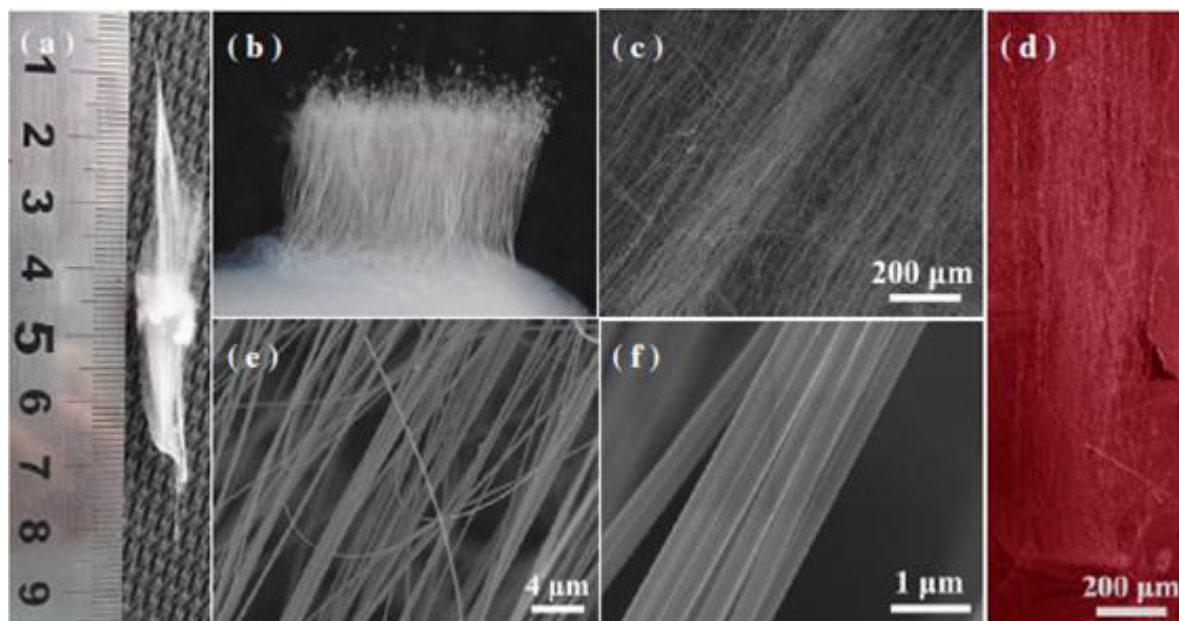


Fig. 2.16. (a) and (b) images of Si_3N_4 nanowires using a digital camera; (c)-(f) typical SEM images of the wires under different magnifications.²²¹

Nanodendrites

Fig. 2.17 shows typical SEM images of the as-synthesized sample at different magnifications. The most surprising feature of the product is that the branches only grew on one surface of the stem, to form a unique asymmetric dendrite structure. The branches are very long, up to several tens of microns (Fig. 2.17(b) and (c)). The ultralong branches could be useful as connecting cables for nanodevices or as three-dimensional reinforcements for nanocomposites. The wireshaped branches are very uniform in size with a diameter of $\sim 50\text{nm}$ and uniformly separated from each other by $\sim 50\text{ nm}$ (Fig. 2.17(d)). Closer observation shows that catalytic droplets exist at the roots of the branches (as indicated by arrows in the inset of Fig 2.17(d)), suggesting the branches grew via a solid-liquid-gas-solid process.

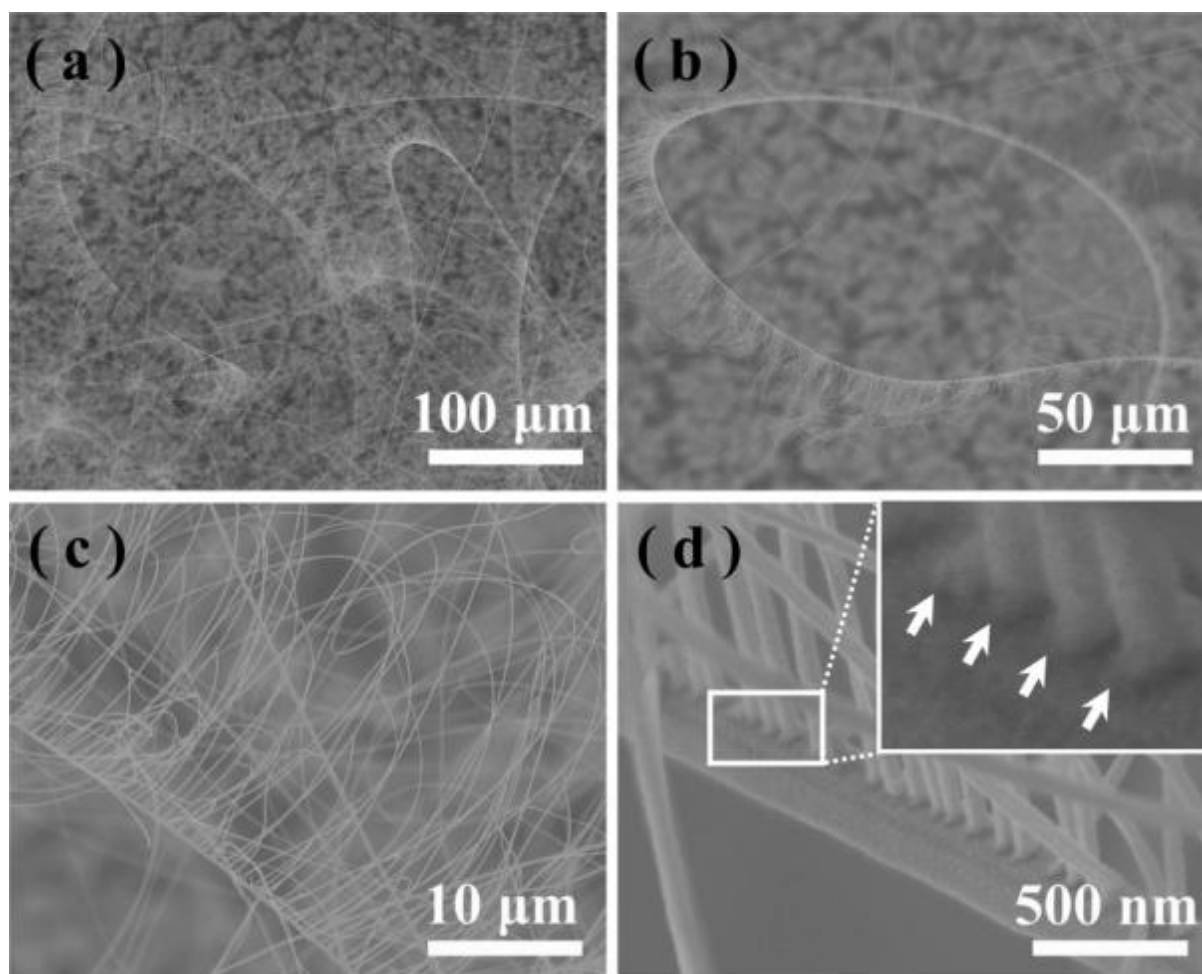


Fig. 2.17. Typical SEM images of the Si_3N_4 nanodendrites at different magnifications showing their overall and detail morphologies. The inset of (d) is the enlargement of the selected area; the arrow-heads indicate catalytic droplets at the root of each branch.²²²

3 Experimentation

3.1 Materials preparation

3.1.1 Technique

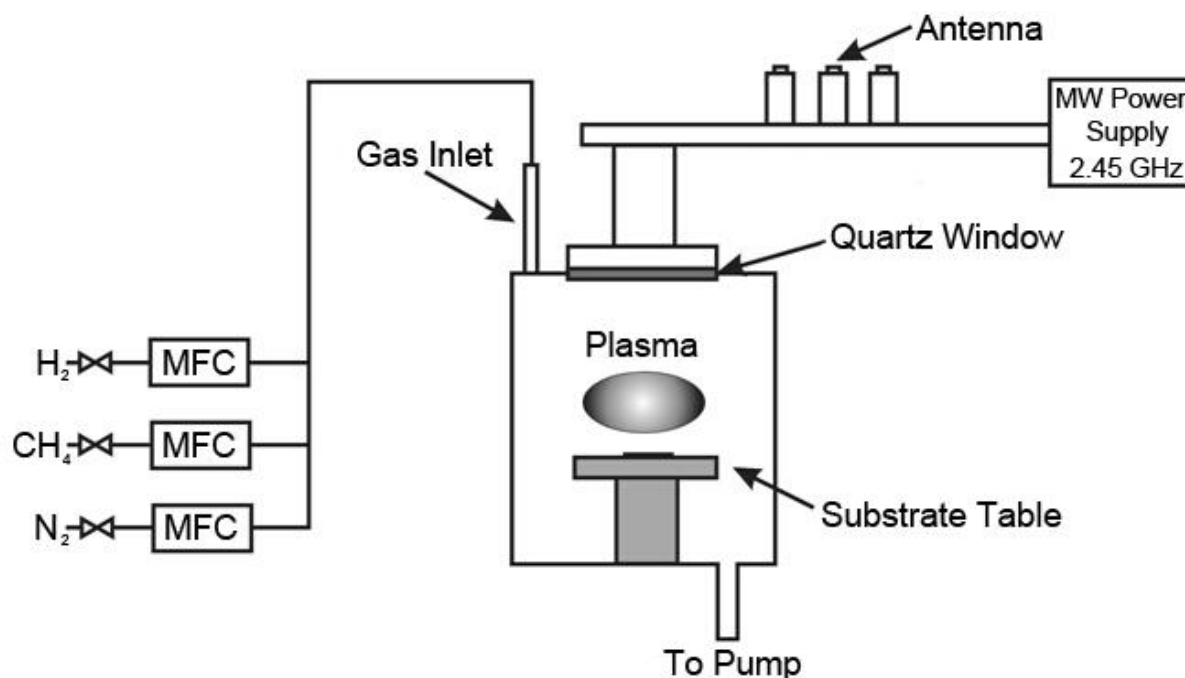


Figure 3.1. Scheme of the MWCVD reactor used in the present work.

In the present work, all the nanostructures were synthesized via microwave plasma enhanced chemical vapor deposition (MWCVD) technique. The description of the MWCVD reactor used in this work will be given here followed by a brief explanation of the operation of the reactor. The schematic of the reactor (ASTeX 5000 W A5000i model) used for all the synthesis processes in this work is shown in Figure 3.1. This reactor has the similar design and operation procedure as ASTeX 1500W S-1500i model, which are shown in Reference 232. The main difference between them is the maximum power and for this reactor it can reach up to 5 kW, which can significantly increase the temperature and the growth rate of nanostructures during the growth process. The body of the reactor where the reaction takes place consists of water cooled double-skinned stainless steel tube. Substrate on which the reaction takes place and where the structures get grown was placed on a molybdenum table in the chamber. The temperature on the substrate surface can be measured by using an external infrared thermometer through the quartz window on the side. The gases H_2 , N_2 and CH_4 used in this work were high purity commercial products compressed (200 or 300 bar) in gas bottles. Microwave generator was used to generate high frequency (2.45 GHz) microwaves that travel through the wave guide and transfer their energy through the quartz window to finally active

the gas mixture generating plasma slightly over the substrate surface. The plasma generated during the course of this work had a spherical form (diameter of about 2 inch). However, the plasma discharge is not stable at higher microwave power and low reactor pressures. More worse, the plasma tends to jump up to the quartz window of the reactor, which is harmful to the equipment. Figure 3.2²³³ gives approximate values for the operation regime. At too low microwave power levels or too high pressures, the plasma cannot be sustained. If the microwave power are too high for a given pressure, the plasma becomes unstable and jumps to the quartz window. The stable operation is only feasible in the central region of the diagram. Due to the external heat induced by the high power, the centre of the wafer can be heated to different temperatures by varying the microwave powers. Therefore, no additional heating of the substrate is needed and the molybdenum table needs water cooling to avoid any damage by the high temperature.

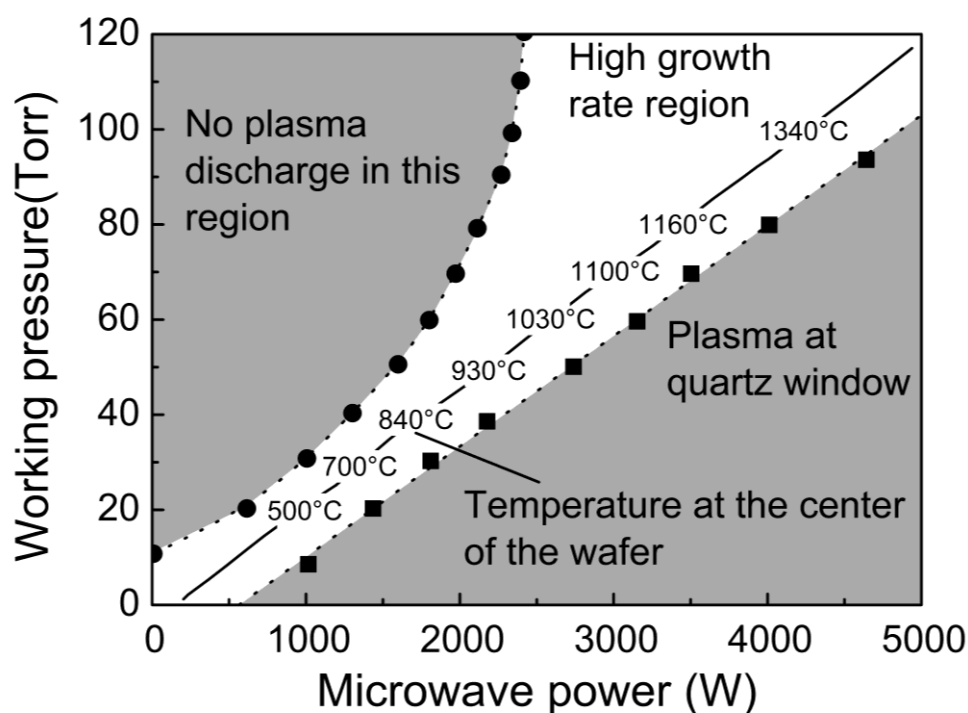


Figure 3.2. Operation regime of ASTeX 5kW MWCVD. The operation is limited to the central region of the diagram.

3.1.2 Procedure

In this section, a brief summary of the experimental procedure used for the novel nanostructures. As we discussed in Chapter 2, catalysts are necessary for the synthesis process of the nanostructures. In the case of CNTs, due to the unknown catalyst system suitable for the synthesis, a mass of attempts were carried on. Different catalysts, such as metal, metal alloys, and

their carbides and nitrides with different physical forms including bulk, thin films and nanoparticles were all utilized. For the bulk catalysts, a pre-treatment of grinding and polishing was needed. For the thin films catalysts, a simple sputtering process was carried on silicon wafers. And catalysts in the form of nanoparticle were bought commercially and dispersed on silicon wafers. In the case of Si_3N_4 nanocones, Fe thin films prepared by simply sputtering of Fe target on silicon wafers were used as catalysts. In the simple sputtering processes, the time determined the thickness of the films, since the voltage and current were kept as constants. The time for all the sputtering processes were 5 min in order to get a very thin film with a thickness of about 100 nm.

As for the gases used for synthesis process, H_2 , N_2 and methane are all commercial products with a high purity of 99.99%. The role of H_2 was to ignite a stable plasma for both the pre-treatment and the synthesis. In the case of CNTs synthesis, N_2 and methane were used because methane worked as the precursor of carbon, while N_2 plasma had a higher energy compared with H_2 . In the case of Si_3N_4 nanocones, N_2 and methane were the precursors of N and carbon, respectively. And the source of silicon was believed to be the silicon wafers.

For each synthesis process, the catalyst was placed on a Mo holder (2 inch in diameter, and 1 cm thick) which was placed on the Mo table of the chamber using Al_2O_3 as a spacer in between. This arrangement can maintain the substrate temperature with a relatively higher temperature, because of the efficient substrate cooling system. The chamber was closed and evacuated to obtain the base vacuum. The pressure and plasma safety interlocks were activated and once the chamber vacuum reaches the required value, which is around 1.0×10^{-2} Torr, H_2 was introduced at a flow rate of 400 sccm (standard cubic centimetre per minute) to about 5 Torr. The microwave power supply was simultaneously switched on and the plasma was then set at 500 W and ignited. The waveguide cavity was tuned using microwave antenna to minimize the reflected microwave power. Subsequently, the gas pressure and the microwave power were increased step by step to reach their set point in about 10 min. During the course of time, the reflected microwave power was tuned to minimum by adjusting the microwave antenna and moving up or down of substrate table. Once all the deposition conditions were set, N_2 was introduced to replace of H_2 to form a plasma. And then CH_4 were introduced into the chamber. At this moment, the synthesis process begins and continues to the required time. To shut down the reactor, CH_4 gas supplies were firstly turned off and then the microwave power was decreased to 1000 W in a step of 200 W and turned off. The H_2 gas supply was re-introduced again for several minutes to cool down the substrate and reactor. At that time, N_2 gas supply was shut down. Once cooled down, the H_2 gas was turned off and the chamber

was evacuated. The sample can be then taken out by stopping the pump and then opening the vent valve.

Because of the totally different processes of synthesizing CNTs and Si₃N₄ nanocones, and the very tiny window for the nanostructures, the detailed parameters during the processes were listed in Chapters 4 and 5 in order to get a more intuitive grasp.

3.2 Characterization tools

3.2.1 Scanning electron microscopy (SEM)

SEM is one of the most frequently used surface morphology characterization methods. In the present work, SEM is mainly used to obtain both in-lens secondary electron images and the back scattered electron images of the morphologies of the catalysts and the as-grown nanostructures. SEM characterization is carried out under a high vacuum (typically 10⁻⁶ Torr). The in-lens image can give information on the appearance or morphology of the sample while the back scattered electron image can give the information of the composition through different contrast. Zeiss Ultra 55 field emission SEM (FESEM) was used for imaging in the present study. The field emission gun is the source of electrons in the microscope and the SEM is operated at an accelerating voltage of 1~3 kV. During the characterization of SEM, the approximate chemical constitution of the catalysts and the as-grown can be achieved by the EDX analysis.

An important characterization by SEM is to gain the morphologies of the individual nanostructure in the copper grid for TEM measurement. Therefore, a special stage which can place and fix the copper grids is needed. And it can be also used for scanning tunneling microscopy.

3.2.2 Transmission electron microscopy (TEM)

The structure of the catalysts and the as-grown nanostructures is also analyzed by using TEM. High resolution TEM (HRTEM) is used to investigate the catalysts, the nanostructures and their interfaces. Selected samples were prepared for TEM analysis and were investigated using a Philips CM200-FEG-UT microscope operating with an acceleration voltage of 200 kV. Standard TEM sample preparation procedure has been followed (in collaboration with Dr. Lei Zhang). The procedure includes mechanical scratching the samples on the catalysts into ethanol (purity as high as 95%) and subsequent dropping the ethanol onto the copper grid by a drip pipe. After minutes of air dry, the copper grid can be used for TEM measurement. A key point for the TEM samples preparation is less ethanol and more nanostructures involved. Definitely,

some of the nanostructures would be destroyed during the process. And there is no more effective means for that.

3.2.3 X-ray diffraction (XRD)

In order to confirm the phase composition of the catalysts and the as-gained nanostructures, X-ray diffraction were performed in the 2θ range of $15-100^\circ$ with a step size of 0.02° . The PW3040 diffractometer from Panalytical X'Pert has been used to carry out the measurement. Cu K α radiation ($\lambda = 1.541874 \text{ \AA}$) was used for the analysis. The X-ray tube was operated at 45 kV and 40 mA. The standard powder diffraction data was used for XRD pattern indexing. And the more information of the catalyst phase were calculated through X-ray diffraction. The interplanar distances of the planes with different Miller indices are of importance for our study.

3.2.4 Micro Raman scattering

Micro Raman scattering is an important and most extensively used technique to analyze nanostructures. It relies on inelastic scattering, Raman scattering, of monochromatic light, usually from a laser in the visible, near infrared, or near ultraviolet range. The laser light interacts with molecular vibrations, phonons or other excitations in the system, resulting in the shifting of the energy of the laser photons.

The Raman measurement in the present study is carried out on a Nicolet Almega XR spectrometer from the company Thermo. An excitation laser wavelength of 532 nm (frequency-doubled Neodymium doped Yttrium Orthovanadate diode pumped solid-state laser (nominal power 25 mW)) was used to obtain Raman spectra. In the present work, high-resolution measurements were carried out between wavelength ranges of 100 to 3300 cm^{-1} employing a 50x objective in the back scattering geometry. In order to determine the detailed information of the peaks in the spectra, a non-linear curve fitting program Peakfit, Jandel Scientific was employed. The peak characteristics (Raman shift, FWHM, intensity and line shape) and the baseline were adjusted for best fit mostly using Lorentzian functions.

3.2.5 Photoluminescence spectroscopy

Photoluminescence spectroscopy is a non-contact, nondestructive method of probing the electronic structure of materials. In essence, Photoluminescence (PL) is a process in which a substance absorbs photons (electromagnetic radiation) and then re-radiates photons. Quantum mechanically, this can be described as an excitation to a higher energy state and then a return to a lower energy state accompanied by the emission of a photon. The period between absorp-

tion and emission is typically extremely short, in the order of 10 nanoseconds. Ultimately, available energy states and allowed transitions between states (and therefore wavelengths of light preferentially absorbed and emitted) are determined by the rules of quantum mechanics.

The PL analysis in the present study is carried out on a F-7000 FL spectrophotometer. An excitation wavelength of 210nm was used to obtain PL spectra. And the photomultiplier tube voltage was 700 V. The range of measurements were carried out between wavelength ranges of 220 to 800 nm. In order to determine the detailed information of the peaks in the spectra, a non-linear curve fitting program Peakfit, Jandel Scientific was employed. The peak characteristics and the baseline were adjusted for best fit mostly using Lorentzian functions.

4 Synthesis of single-chirality multi-wall carbon nanotubes

This chapter presents the results pertaining to the synthesis of single-chirality multi-wall carbon nanotubes. A novel growth process for single-chiral carbon nanotubes will be exhibited.

4.1 Strategies for chirality-controlling growth of carbon nanotubes

Chirally pure CNTs are required for various applications ranging from nanoelectronics to nanomedicine. Up to date, it seems experimentally impossible.

It is well known that chirality controlling for single wall tubes is much easier than that for multi-wall ones. For an individual single wall carbon nanotube, its chirality is determinate, either chiral or achiral. The work still needed is that to get a catalyst which can catalytically grow carbon nanotubes with certain chirality.

While for multi-wall carbon nanotubes, chirality controlling growth goes with more complexity. The first thing is to address the question of the structural relationship between successive cylinders. This has been discussed by Zhang²³⁴ and colleagues and by Reznik²³⁵, who have reached broadly similar conclusions. In their viewpoint, it is assumed that the tubes are concentric, named ‘Russian doll’ rather than ‘scroll-like’ in structure, shown in Fig. 4.1. Experimental electron diffraction patterns of multiwall nanotubes usually show spots from both non-chiral and chiral tubes²³⁶, which could be taken as further evidence for a Russian doll structure, since a ‘scroll’ nanotube would have the same helicity throughout.

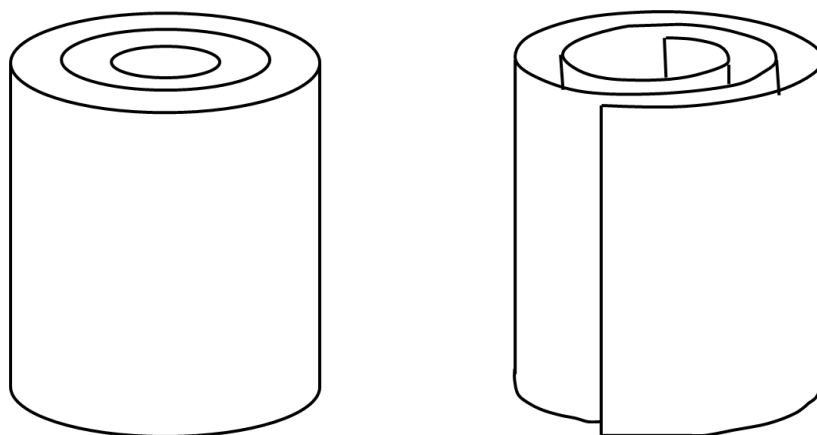


Fig. 4.1. Schematic illustration of ‘Russian doll’ and ‘Scroll-like’ models for multi-wall nanotubes.

A typical diffraction pattern, taken from the work of Zhang et al., is shown in Fig. 4.2. This pattern was recorded from a multiwall nanotube with 18 individual layers and an innermost diameter of 1.3 nm; the incident electron beam is normal to the tube axis. In this pattern the $\{0001\}$ spots which result from the parallel graphene layers perpendicular to the beam can be seen running horizontally on either side of the central spot. The other arrowed spots all correspond to reflections from achiral (i.e. zig-zag or armchair) tubes, and are of the $\{10-10\}$ or $\{11-20\}$ type. The other, weaker reflections are due to chiral tubes. Careful analysis of the spots from chiral nanotubes enables the chiral angle to be determined.

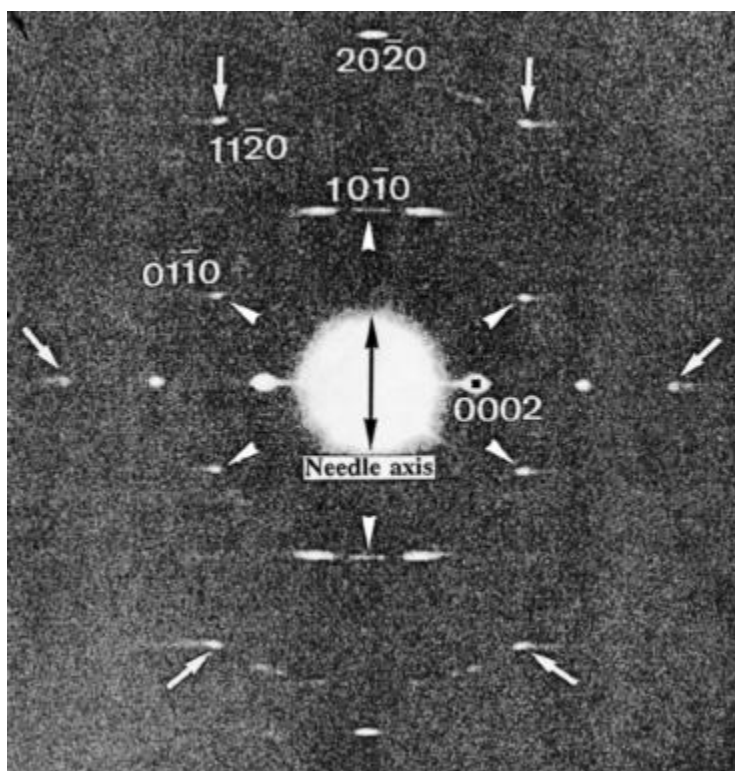


Fig. 4.2. Electron diffraction patterns of a multi-wall nanotube.²³⁶

Another important conclusion got from the diffraction pattern above is that the microstructure of the carbon nanotube is tanglesome. In other words, for an individual multiwall carbon nanotube, the chirality is not single.

Most significant efforts have been directed towards SWCNTs. These efforts can be divided into methods that sort the nanotubes after synthesis and those which seek to produce only nanotubes with a particular chiral angle. Sorting methods have made significant progress using a variety of techniques including wrapping by single-stranded DNA and then separation

by anion exchange chromatography²¹⁷; selective etching by a plasma hydrocarbon reaction²¹⁸; attachment of surfactants and subsequent density gradient ultracentrifugation²¹⁹; precipitation following chemical treatment²²⁰; adsorption of CNTs on agarose and freezing followed by mechanical separation²²¹; and in situ and postsynthesis oxidation²²². DNA sorting techniques have even recently separated CNTs by chiral angle²²³. Often, however, the processing steps involved in these techniques are difficult, reduce yield, and are unsuitable for applications requiring significant quantities of SWCNTs.

Meanwhile, people began to attempt to growing SWCNTs with a particular chiral angle by varying the catalysts or changing the processing parameters. W. Chiang et al.²³⁷ found that the chirality distribution of as-grown SWCNTs could be altered by varying the composition of $\text{Ni}_x\text{Fe}_{1-x}$ nanocatalysts. Precise tuning of the nanocatalyst composition at constant size was achieved by a new gas-phase synthesis route based on an atmospheric-pressure microplasma. They also suggested that the link between the composition-dependent crystal structure of the nanocatalysts and the resulting nanotube chirality supported epitaxial models and could be a step towards chiral-selective growth of SWCNTs. Z. Ghorannevis et al.²²⁸ even utilized the nonmagnetic Au nanoparticles to catalytically synthesize of narrow-chirality distributed single-walled carbon nanotubes. Their research revealed that plasma chemical vapor deposition (PCVD) with the nonmagnetic catalyst under the appropriate H_2 concentration was critical as the methodological element of realizing the narrow-chirality distribution. B. Wang²³⁸ reported the selective growth of bulk SWCNT samples enriched with three different dominant chiralities including (6, 5), (7, 5), and (7, 6) through adjusting the pressure of carbon monoxide on Co-Mo catalysts from 2 to 18 bar.

The efforts above have made the properties of SWCNTs a certain degree improvement, especially the electrical property. However, in fact, they can do nothing more than narrowing the chiral distribution of CNTs.

For multi-wall carbon nanotubes, only a little attention focused on this. Multi-wall CNTs with narrow chiral angles distribution in each layer have been produced by low-temperature plasma-enhanced CVD²³⁹, and pyrolysis of iron phthalocyanine²⁴⁰. The possible chiral angles of such multi-wall CNTs are constrained because the graphene interlayer spacing must be maintained while also allowing the graphene sheet to close itself as a cylinder. Recently, S. W. Pattinson investigated a diverse range of nitrogen sources for their ability to control CNT chi-

ral angle via epitaxial growth from highly ordered catalyst particles²⁴¹. Despite intensive research, the mechanisms by which the chiral angle is influenced are often only partially understood, feature low yields, or otherwise require very specific conditions that would be difficult to reproduce industrially.

From the studies above, we can conclude that catalyst must play a key role during the CNTs growth. And detailed investigation of a single catalyst, and the interfaces between catalyst and the CNTs could give an answer to the controlling growth. Therefore, A systematic study on the own mechanisms is essential to possibly find a gap not ever understood.

In the commonly accepted growth mechanism of carbon nanotube, carbon dissolves into the catalyst and CNTs grow due to the precipitation of excess carbon on or just beneath the metal surface of the catalyst particle. This idea originates from the VLS mechanism suggested by Wagner et al., which was derived to explain the growth of single crystal Si wire²⁴². The schematic is shown in Fig. 4.3. The basic concept is as follows: (i) dissociation of hydrocarbon gas on the surface of the catalyst, (ii) diffusion of carbon atoms through the bulk of the catalyst, and (iii) precipitation of carbon from saturated catalyst particles to form 1D carbon nanostructures. In this model, the catalyst forms a liquid droplet and preferentially adsorbs the growth species from the surrounding vapor, finally growing the CNTs from this supersaturated eutectic liquid. In the case of growth of carbon nanotubes, graphite layers grow out of the liquid Fe-C (Ni-C, Co-C, etc.) eutectic. It is well known that liquid cannot be long-range ordered. Therefore, it is impossible that all the graphite layers can get the same crystallographic structure from the liquid eutectic. Liquid catalyst during the carbon nanotube growth is the possible reason accounting for the rambling structures, which are the most common products in CNTs synthesis processes.

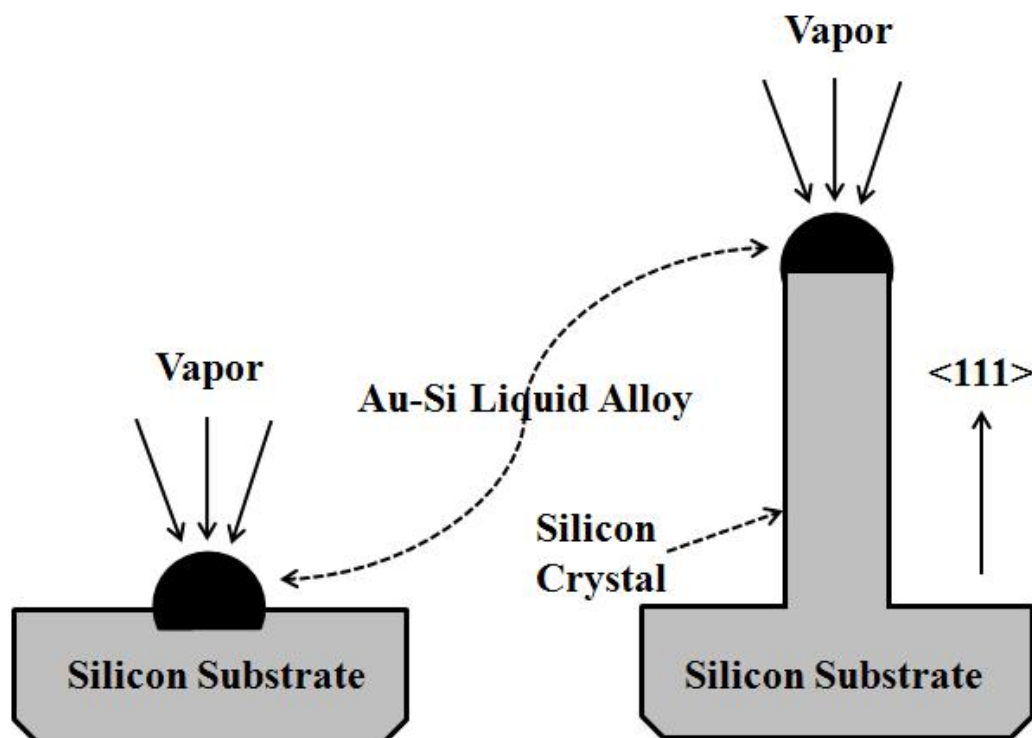


Fig. 4.3. Idealized drawing of VLS mechanism illustrated for growth of a silicon crystal.

Another model, so called “Yarmulke mechanism”, was proposed by H. Dai et al. in 1996, which described the early nucleation of all layers of CNTs²⁴³. Surface energy plays a dominant role for a nanoscale particle. A metal particle only a few nm in diameter contains a very high percentage of surface atoms, creating a tremendous surface energy problem on a per atom basis. An excess of carbon can help to solve this problem by assembling a graphene cap on the particle surface, with its edges strongly chemisorbed to the metal. Since the basal plane of graphite has an extremely low surface energy (10-20 times smaller than most metals), the total surface energy diminishes. Newly arriving carbon will continue to assemble on the surface of the catalytic particle. Then a second cap can form underneath the first, spaced by roughly the interlayer spacing of graphite. As additional caps form, one beneath the other, older caps are forced to lift up by forming a cylindrical tube whose open end remains chemisorbed to the catalytic particle. Nucleation of new (inner) layers will halt once the strain due to increasing curvature of new layers becomes too great. After nucleation, the carbon diffuses either on the surface or through the bulk to the chemisorbed open edges of the nanotube, at which time these new carbon atoms insert into the nanotube network to form the CNTs.

A calculated model by S. Reich et al.²⁴⁴ also illuminates that the importance of the early nucleation. Different from Yarmulke mechanism, S. Reich thinks that some caps forming on the catalyst at the nucleation stage could be favored by their epitaxial relationship to the solid catalyst surface. The chirality-selective growth of nanotubes can be controlled the type of caps. Their *ab initio* calculations suggest that lattice-matched caps and tubes are more stable next to a catalyst surface than non-lattice-matched structures.

Therefore, a possible routine for chiral-controlling growth of CNTs can be deduced as follows:

1. A catalyst is necessary. The catalyst should maintain solid state all through the CNTs growth process;
2. Some planes on a certain axis of the catalyst should have some matching relationships with (002) plane of graphite;
3. Optimized processing parameters.

4.2 Synthesis of single-chirality multi-wall carbon nanotubes

4.2.1 The catalyst selection

In the most cases of CNTs growth, catalyst particles react with carbon atoms to form liquid eutectic, which is mentioned above in VLS mechanism²⁴². However, catalysts in the solid state during the CNTs growth process, is prerequisite for the epitaxial delivery crystalline information occurring on the interfaces of catalysts and CNTs.

As we know, catalysts using for CNTs growth in CVD process exhibit a small dimension in diameter, usually several to tens of nanometers. Due to the little size effect of nanomaterials, the melting point of nanoscale catalysts is much lower than that of bulk. Therefore, pure transport metals and their compounds hardly maintain solid state during CNTs growth processes, which are carried on normally at a temperature higher than 600 °C. Can the catalysts be in other forms, such as carbide, nitride, or others?

An atomic scale in situ environmental transmission electron microscopy (ETEM) observation of the nucleation of single-walled CNTs and multi-wall CNTs in Fe catalyzed CVD followed by continuous growth was carried out by H. Yoshida et al²⁴⁵. Surprisingly, CNTs grow from nanoparticle catalysts (NPCs) of crystalline Fe carbide. Although there is no crys-

talline relationship between the catalyst and the as-grown CNTs, it opens the door to discover the secret behind CNTs growth process utilizing a new form of catalyst.

The reason for non-crystalline relationship between the catalyst and the as-grown CNTs is that during the whole process, the NPCs are structurally fluctuating. Since the NPC remains at nearly the same position on the substrate and deforms only slightly, the observed phenomenon is accounted for by a change in crystal orientation without physically rotating the whole NPC. The structure of smaller NPCs for the growth of SWNTs seems to fluctuate more remarkably. It is well-known that metal nanoparticles fluctuate in vacuum at room temperature²⁴⁶⁻²⁴⁸. The nanoparticles of cementite, which is known to be hard and brittle in iron steels, fluctuate not only in vacuum but under the gas environment at the elevated temperature. Therefore, a continuous and stable delivery of crystalline information could be impossible.

Inspired by the fact above, a principle of catalyst selection is set up as follows:

- Transition metals or their compounds with a high melting point;
- Carbides or nitrides of the potential candidates with a high melting point;
- A set of planes of the potential carbides or nitrides have possible crystalline match with (002) planes of graphite.

After systematic study on the phase diagrams of carbides and nitrides of transition metals and possible addition metals, a kind of carbide of FeCr alloy is confirmed for the following study. The ternary phase diagram of Fe, Cr and C²⁴⁹ is shown in Fig. 4.4. The phase diagram describes the phase changes with the variation of Cr, C content and the temperature. The phases α and γ are solid solution phases. The phases K_1 , K_2 and K_C represent $(Cr,Fe)_{23}C_6$, $(Cr,Fe)_7C_3$ and $(Cr,Fe)_3C$, respectively²⁴⁹. The corresponding solubilities of carbon is 5.6%, 9% and 6.67%²⁴⁸. It can be deduced that with the increasing of C content, the melting point of the corresponding phase rises observably, which could meet the requirement of high melting point catalysts in a carbon rich atmosphere.

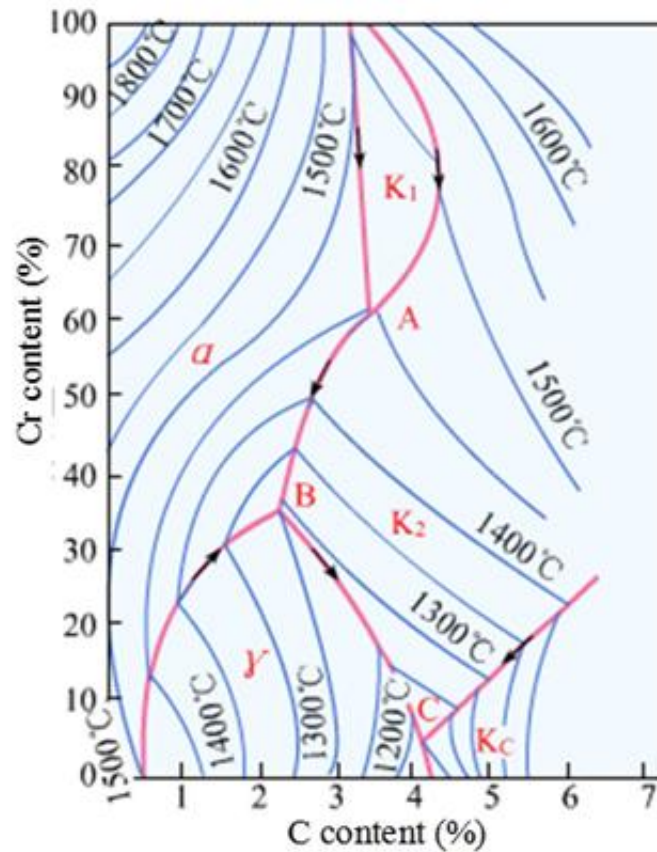


Fig. 4.4. Fe-Cr-C phase diagram.²⁴⁹

4.2.2 The synthesis process

Normally, the synthesis process of nanomaterials is tricky, which has only a very small space for varying processing parameters. Different from synthesis of other forms of materials, such as bulk and films, there are no changes with a certain rule with the changing of processing parameters regularly. Before the goal is achieved, every attempt seems useless. If there must be a role of the works having done, that is excluding that parameter combination.

In the case of the present work, the principle of adjusting the process parameters is firstly to get a high temperature atmosphere, where the high temperature phase FeCr carbide could be formed; secondly, to get a not so high temperature atmosphere, otherwise, the carbide catalyst will melt; at last, a sufficient carbon supply must be ensured. The first two points look like contradictory. However, after summing up the experimental findings, we find that the answer is no. The fact is that once the carbide is formed, it will dissolve more carbons instead of getting melting when the temperature rises up not so much. Simultaneously, the solid car-

bide will act as a catalyst to form CNTs when the temperature keeps constant and the carbon supply is abundant.

Table 4.1 *The processing parameters for CNTs synthesis.*

Microwave power (W)	Gas pressure (Torr)	Methane flow rate (sccm)
700	12, 15, 18	
750	15, 18, 21	
800	17, 20, 23	
850	19, 21, 25	
900	22, 25, 28	
950	22, 25, 28	5, 10, 15, 20, 25, 30, 35, 40, 45
1000	22, 25, 28	
1050	22, 25, 28	
1100	22, 25, 28	
1150	24, 26, 30	
1200	27, 30, 33	

During the concrete operation of CNTs growth in the present work, there are three adjustable parameters: the microwave power, the gas pressure and the methane flow rate. The microwave power affects the temperature of the process. High microwave power can bring high temperature atmosphere. Owing to the basic operating requirement of MWCVD technique, a small adjustable range of gas pressure corresponds to a certain value of microwave power. In the small range, the increase of the gas pressure can condense the plasma sphere to elevate the energy of particles. In the case of the methane flow rate, more methane will make the plasma brighter, indicating increasing system energy. But there is a limit for the amount of methane flow rate, which can be identified intuitively that the bright plasma will get darker, even to

form another plasma sphere. Process over the limit will harm to the MWCVD equipment. Table 4.1 shows the attempts for the synthesis of single-chirality CNTs in the present work, while the nitrogen flow rate was kept as a constant of 45 sccm.

The processing parameters for single-chirality CNTs growth is confirmed as follows shown in Table 4.2. The temperature for the synthesis process is kept constant, 850 °C measured by an infrared thermometer. And the repetition of synthesis process is identified to be good.

Table 4.2. *The processing parameters for single-chirality CNTs growth.*

Pre-treatment	Base pressure ($\times 10^{-2}$ Torr)	1.2-1.8
	Gas flow rate (sccm)	100
	Gas pressure (Torr)	35
	Microwave power (W)	1500
	t (mins)	30
Synthesis process	Gas pressure (Torr)	25
	Gas flow rate (sccm)	CH ₄ : N ₂ = 35 : 45
	Microwave power (W)	1100
	t (mins)	240

Fig. 4.5 shows the by-products in the present work. There are carbon microspheres, carbon microspheres with nanocones, carbon sphere films, carbon chains, carbon nanofibers, carbon nanotube films and amorphous carbon, which may be useful in other fields of research, and will not be further studied here.

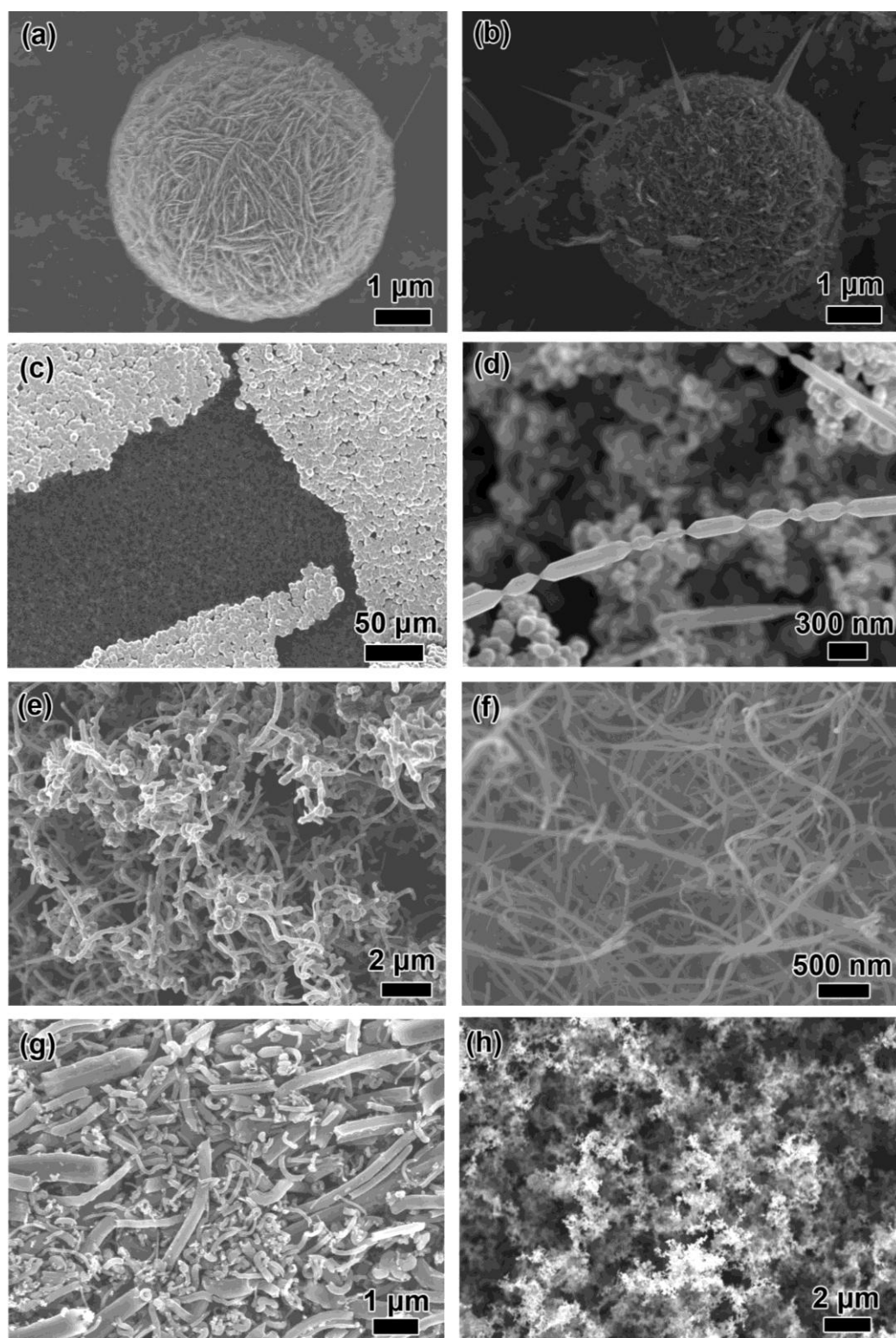


Fig. 4.5. By-products in the present work: (a) carbon sphere; (b) carbon sphere with nanocones; (c) carbon sphere films; (d) carbon chains; (e) and (f) carbon nanofibers; (g) carbon nanotube films; (h) amorphous carbon.

Another remarkable point is that the processing time, 240 min, is much longer than that of less than 30 min reported in the literatures. Systematically analyzing the products of different processing times shown in Fig. 4.6, we find that the synthesis of the catalysts, FeCr carbide, takes almost a half time. What's more, a higher solubility of carbon atoms in that catalyst should also account for the long processing time.

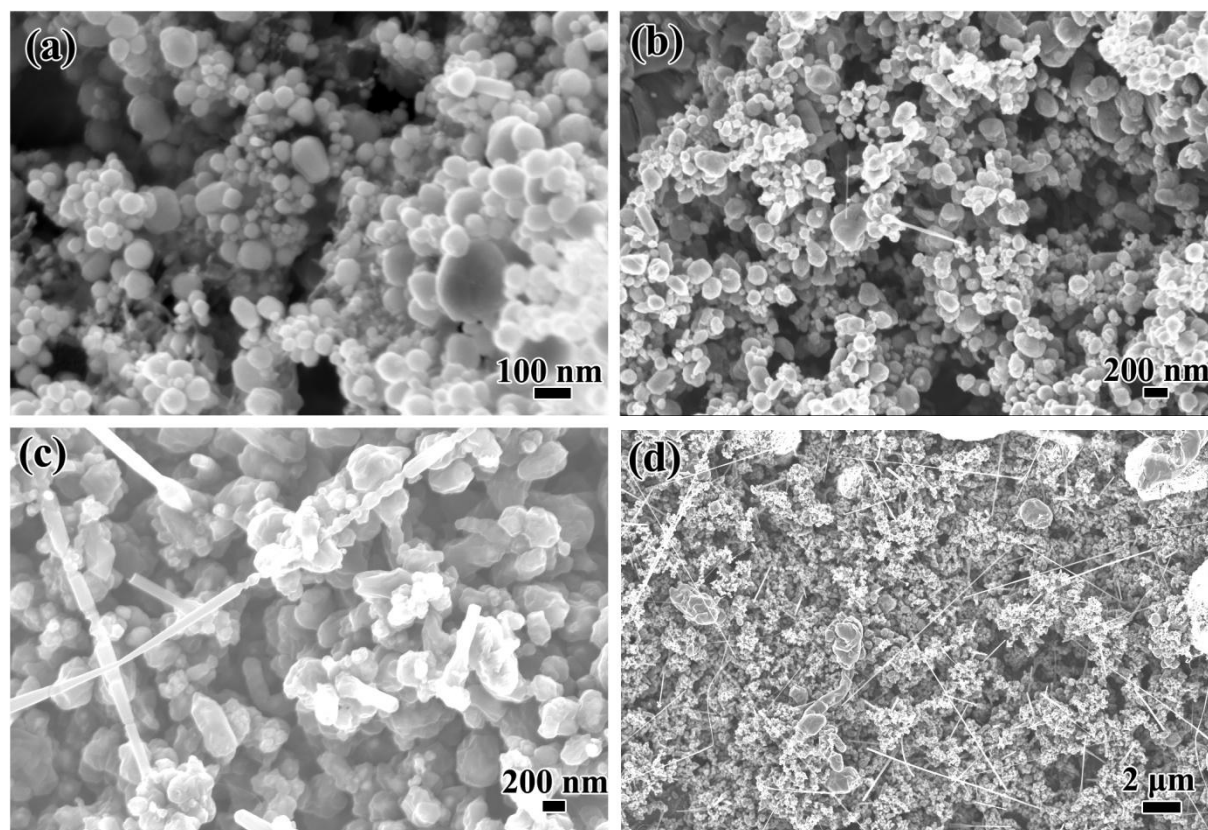


Fig. 4.6. Products of different processing time: (a) 60 min; (b) 120 min; (c) 180 min and (d) 240 min.

4.2.3 The characterization of catalyst

Since catalysts play a key role during the single-chirality CNTs processes, it is necessary to investigate in detail the states of the catalysts, including the composition, phase, morphology before and after the CNTs growth.

As can be seen from Fig. 4.6 (a) and (b), the catalysts exhibit sphere morphology, with a diameter of tens to two hundred nanometers. Not all the catalysts can catalyze the CNTs growth, deduced from Fig. 4.6 (c) and (d). The reason for that is catalysts with certain orien-

tions can make sense for the growth process, which will be discussed in the later sections. And the diameters of CNTs directly depend on those of the catalyst sphere.

Fig 4.7 shows the XRD pattern, electron diffraction (ED) pattern and EDX curve of the catalysts before the growth of CNTs. As discussed above, pure catalyst film can be formed at the processing time of 120mins. It seems that the CNTs will nucleate at next minute. Therefore, the catalysts are chosen for the examination by the techniques mentioned at the beginning of this paragraph. From the XRD pattern shown in Fig. 4.7 (a), we can find that besides the peaks corresponding the substrate, there are peaks corresponding to (420), (202) and (203) planes of the phase $(\text{Cr,Fe})_7\text{C}_3$. The catalysts grow in a random mode, without a preferred orientation. The values of 2θ of the catalyst peaks are a little small than those of standard powder $(\text{Cr,Fe})_7\text{C}_3$ crystal, which can be attributed to the small size effect.

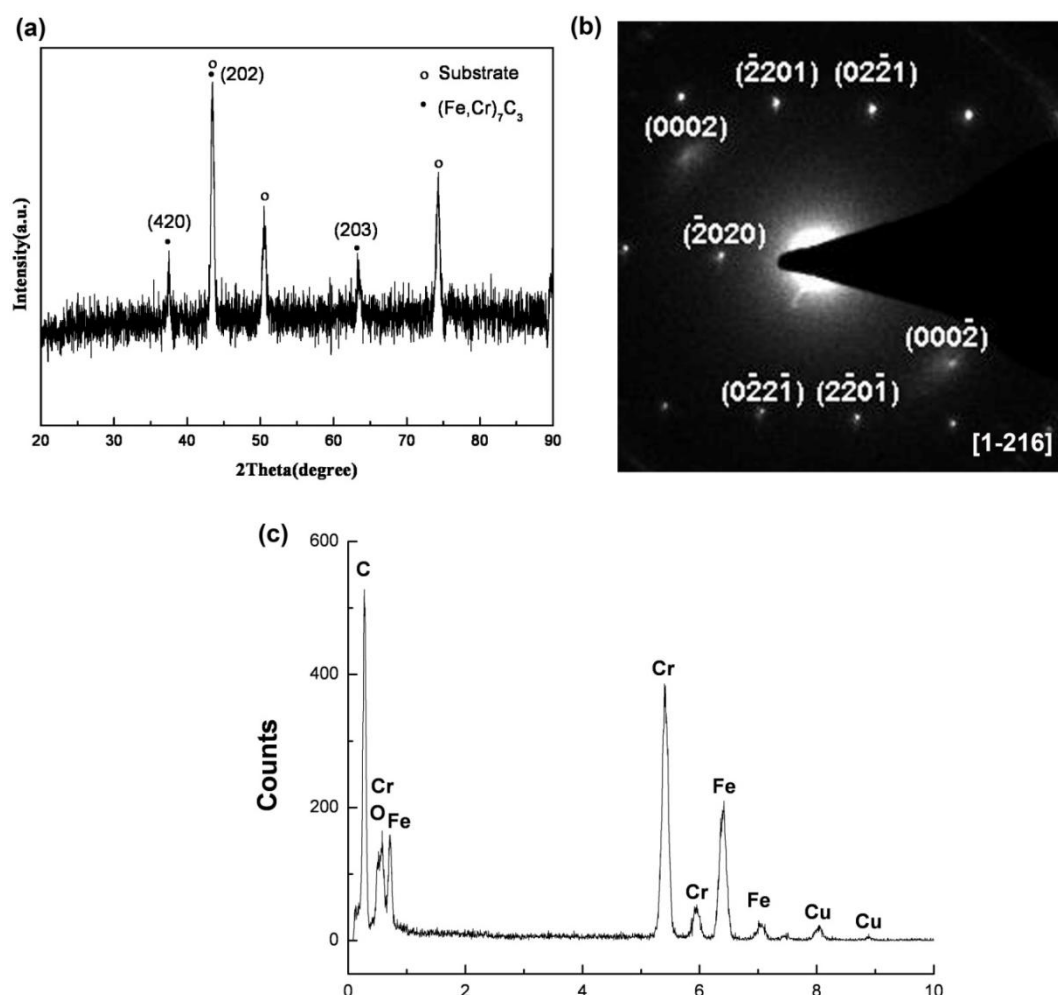


Fig. 4.7. The XRD pattern(a), ED pattern(b) and EDX curve(c) of the catalysts before CNTs growth.

The composition information of the catalyst from Fig. 4.7 (c) and (d) confirms XRD result discussed above. In the EDX curve, the content of carbon mostly comes from carbon film of the copper grid, absorbed particles and the catalyst. Therefore, its value is much higher than the real value in the catalyst. Oxygen and copper can be omitted because they comes from the absorbed particles and copper grid, respectively. The contents of chrome and iron reflect verifiably the composition of the catalysts.

The phase of the catalysts is determined precisely by electron diffraction pattern shown in Fig. 4.7 (b). The pattern was taken under the incident electron beam parallel to the $[-12-16]$ axis of the catalyst. As can be seen from the pattern, every single catalyst is a monocrystal. The planes (-2202) $(02-21)$ and (-2020) can be directly recognized under that axis. Summing up the three facts mentioned we can conclude that the phase of catalysts before CNTs growth is $(\text{Cr,Fe})_7\text{C}_3$. Another remarkable point is that in the pattern there are weak spots forming a circle. We believe that this phenomenon result from the amorphous graphite layers covering the catalyst. Since the catalysts exhibit very small size, the surface energy of the catalyst will be huge. While, the amorphous graphite layers have a rather low surface energy. Therefore, at the carbon rich atmosphere, it is easy that the catalyst is covered by amorphous graphite layers.

The catalysts after the CNTs growth were examined by HR-TEM images and ED patterns. The results are shown in Fig. 4.8. The ED patterns reveal that there are no phase transitions or state changes of the catalysts during the synthesis process. The catalysts maintain the solid $(\text{Cr,Fe})_7\text{C}_3$ phase, which benefits the controll of the CNTs structures. Indeed, we observed that the CNTs grew out from the catalyst. And the catalytic monocrystals exhibit different axial directions to control the CNTs growth, such as $[0001]$ and $[2-1-10]$, shown in Fig. 4.8.

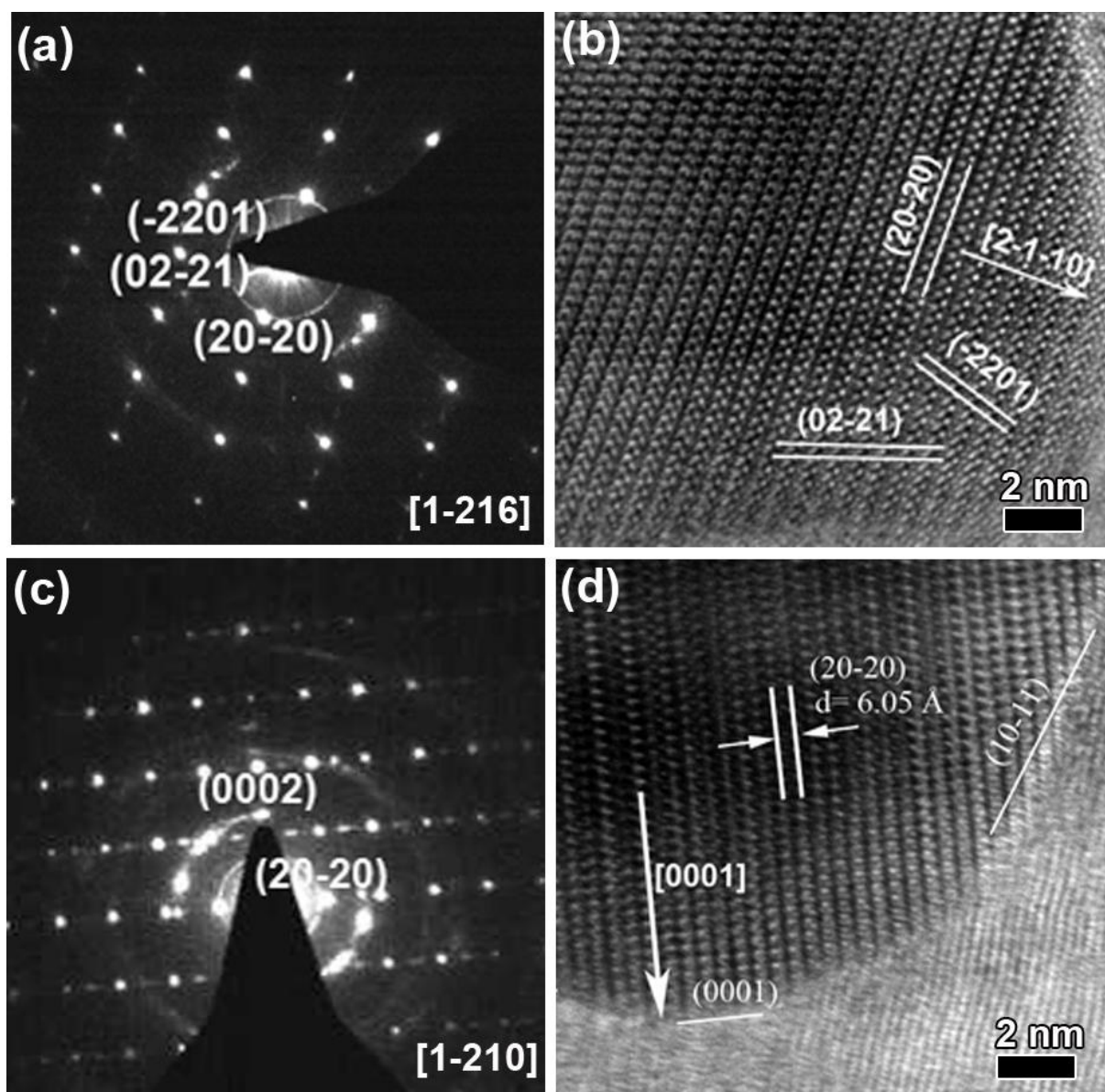


Fig. 4.8. HR-TEM images and ED patterns of the catalysts after CNTs growth.

4.2.4 The characteristic of as-grown carbon nanotubes

Fig. 4.9 shows the as-grown carbon nanotubes at the optimum processing parameters. From the images we can see that the CNTs were grown accompanied by some carbon spheres with a diameter of several micrometers. Detailed investigations indicated that these spheres did not aid to grow CNTs, but acted as signals of the success of the CNTs growth. The CNTs were grown straightly, and with no preferred orientation, which is much different from other reports.

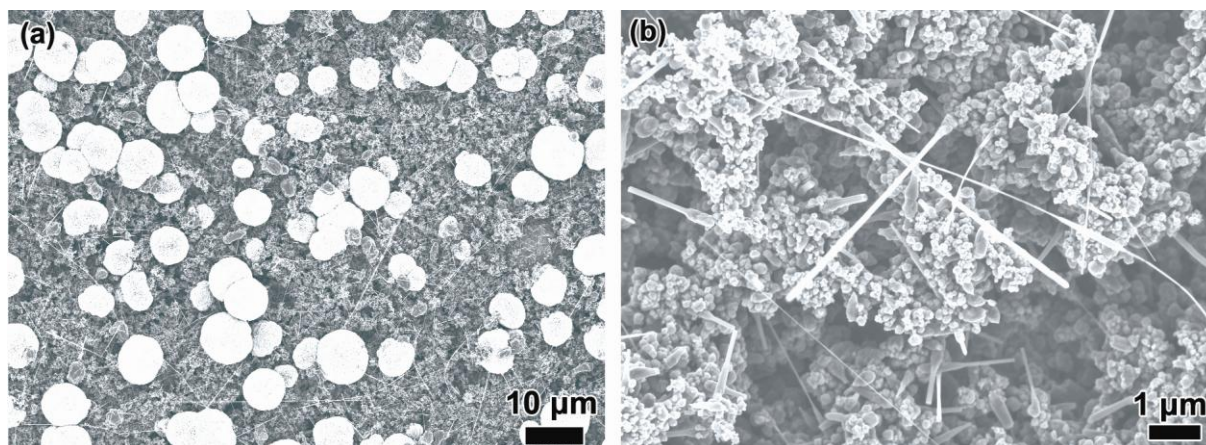


Fig. 4.9. The SEM images of as-grown CNTs at the optimum processing parameters.

The as-grown CNTs have a wide length range, from hundreds nanometers to several micrometers. This could be a circumstantial evidence for the necessity of the catalysts for the growth of CNTs in the present work. Since the formation of catalysts depended on the diffusion of iron and especially chrome atoms to assemble enough sources. For an individual catalyst, the time of its formation could be different from others, which could be the main factor causing the different lengths of CNTs.

The as-grown CNTs have a wide range in diameter, from tens to hundreds nanometers. This phenomenon is also attributed to the different diameter distribution of catalysts. And the thinner diameter CNTs give the opportunity to further study the relationships between the CNTs and catalysts utilizing TEM.

Fig. 4.10 shows the image of an individual CNT grown at the optimum parameters. Through EDX analysis, catalyst particles are observed at the bottom of the CNT, suggesting a catalytic base-growth of the CNTs.

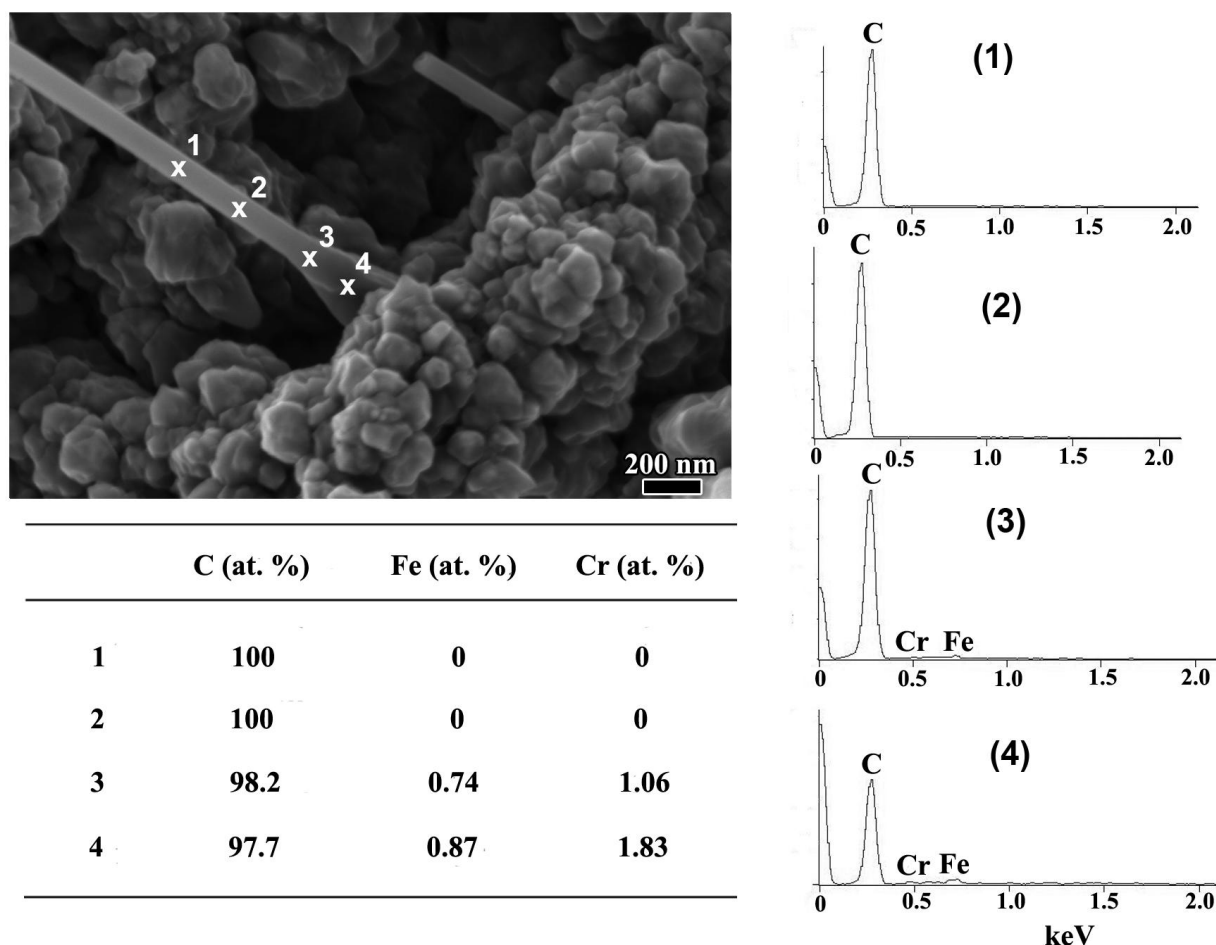


Fig. 4.10. SEM image and EDX analysis of an individual CNT.

The chirality of the as-grown CNTs was determined via electron diffraction technique. Fig. 4.11 shows the typical electron diffraction patterns of the CNTs. And the incident electron beam is normal to the tube axis. Due to the finite size of carbon nanotubes in the radial directions, the electron diffraction spots are elongated perpendicular to the tubule axis and therefore form diffraction layer lines. In all the patterns the $\{000l\}$ spots which result from the parallel graphene layers perpendicular to the beam can be seen running horizontally on either side of the central spot. The other spots of the pattern shown in Fig. 4.11 (a) all correspond to reflections from achiral zig-zag tubes, and are of the $\{10-10\}$. In the patterns shown in Fig. 4.11 (b)-(h), besides the $\{000l\}$ spots, other spots are positioned at the apices of two regular hexagons, indicating a simple chiral property. The single-chirality cannot be deduced since in some cases CNTs with different chiral indices can have the same chiral angle, such as CNTs with the chiral indices (15, 1) and (30, 2). Therefore, it is necessary to identify the chiral in-

dex (m, n) of CNTs and it will be done in the following sections. The chiral angles of the CNTs in the present work are mostly 0° or less than 15° , shown in Fig. 4.11.

A notable morphology feature of the as-grown CNTs is that all the CNTs have faceted surfaces, which was also reported on the tubular graphite cones (TGCs)⁴⁹. Fig. 4.12 shows the faceted CNTs with different helical angles. After examining a good number of CNTs by SEM we found that the helical angles of the CNTs were among the range of $0 - 30^\circ$. However, not CNTs with every angle therein could be gained and most of them were at the certain values. For example, CNTs with a helical angle of 0° , shown in Fig. 4.12 (a) and (b), could be mostly found. CNTs with a small helical angle of less than 15° , shown in Fig. 4.12 (c) and (d) could also be found easily. CNTs with a higher helical angel of more than 15° , shown in Fig. 4.12 (e), could be found for only a few times. Intuitively, there may be a relationship between the extrinsic helical angle and the intrinsic chiral angle. This question will be further studied in latter Chapter 4.4.

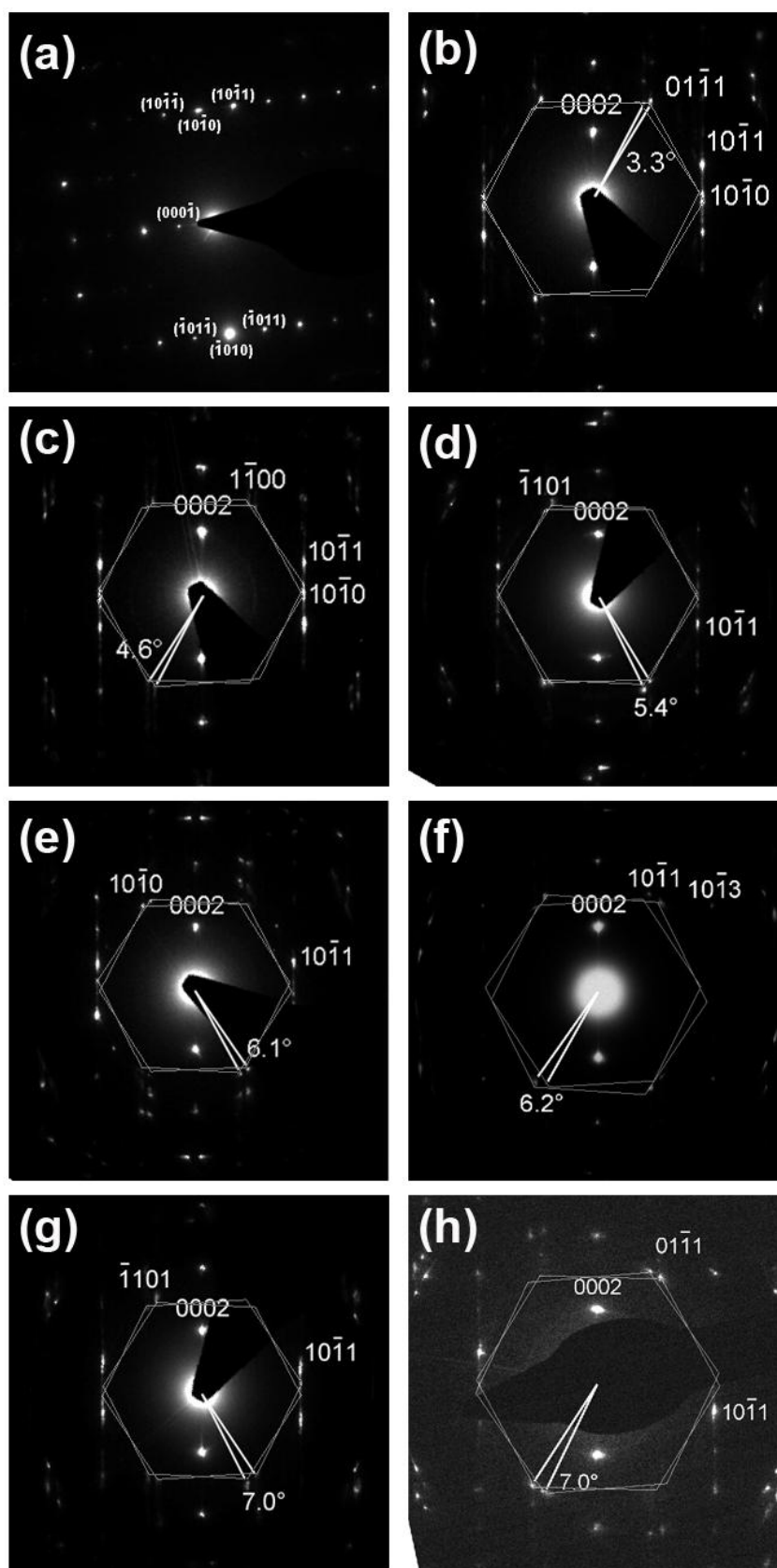


Fig. 4.11. Electron diffraction patterns of as-grown CNTs.

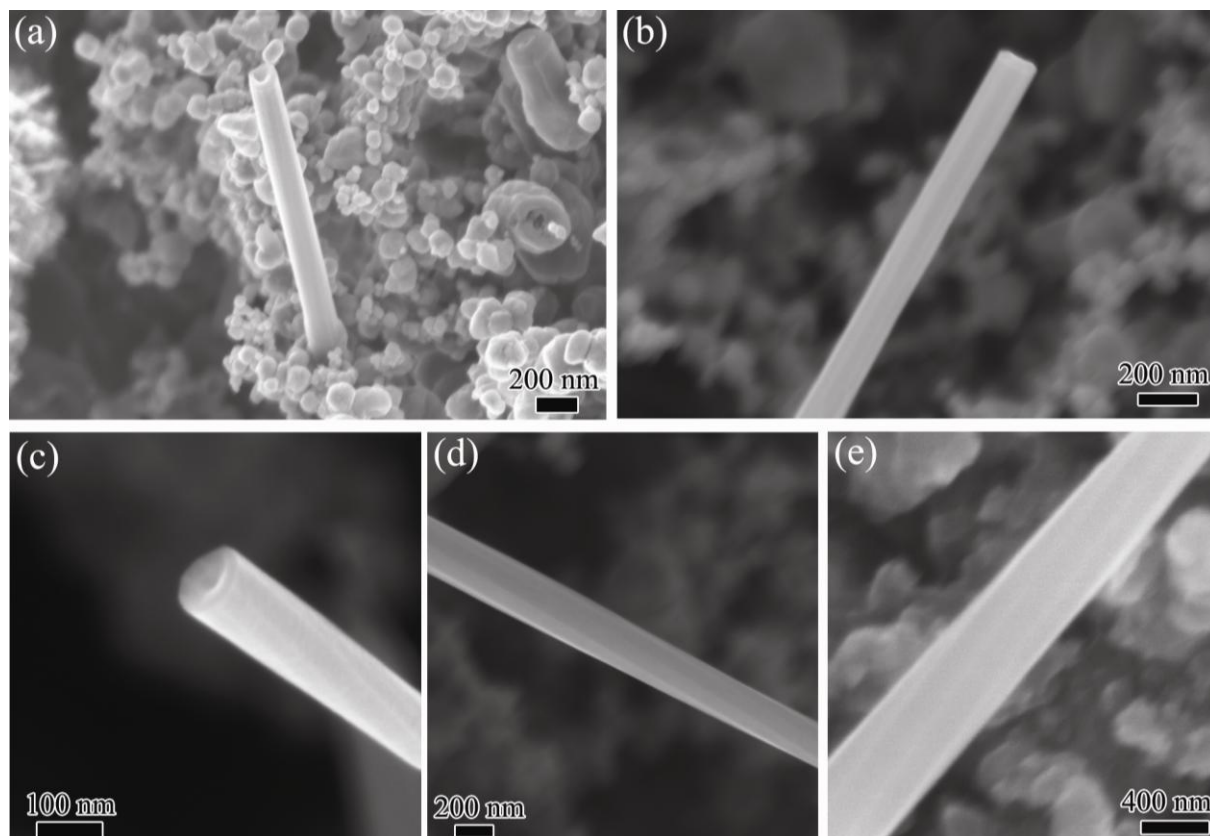


Fig. 4.12. CNTs with different helical angles.

4.2.5 Determination of the chiral indices (m, n) of carbon nanotubes

In the present work we utilize a convenient method to determine the chiral indices (m, n) firstly proposed by L. Qin²⁰⁰, which has been detailed introduced in Chapter 2. Two examples are shown in Fig. 4.13 and the detailed process of the chiral indices determination will be expounded as follows.

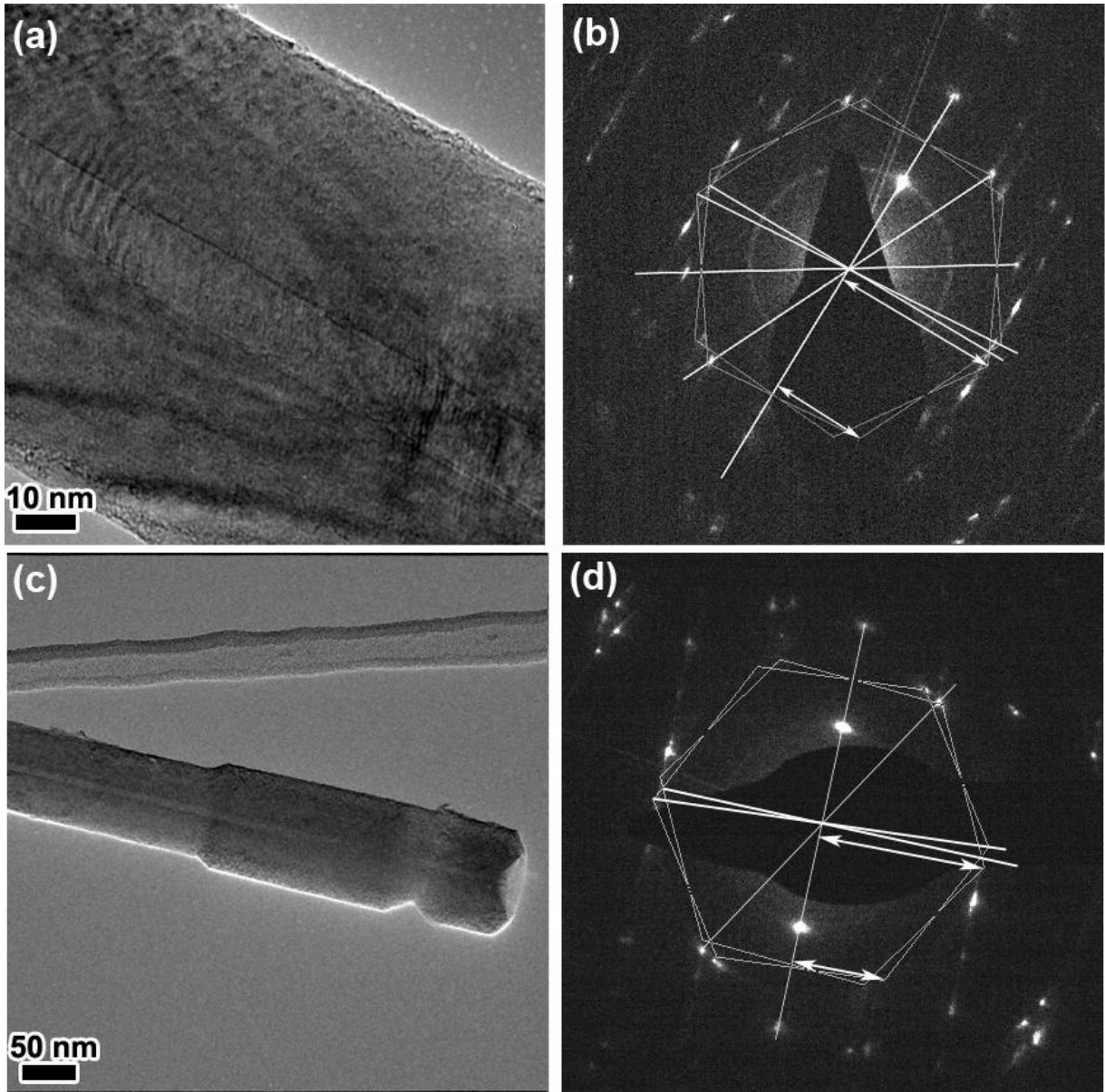


Fig. 4.13. Determination of the chiral indices (m, n) of CNTs.

For the CNT shown in Fig. 4.13(a),

$$\alpha = \tan^{-1}\left(\frac{2D_2 - D_1}{\sqrt{3}D_1}\right) = 4.95^\circ, \quad (4.1)$$

$$\frac{n}{m} = \frac{2D_2 - D_1}{2D_1 - D_2} = \frac{2}{9}, \quad (4.2)$$

indicating the CNT with a diameter of 1.572 nm. But as can be found in Fig. 4.13(a), the diameter of the CNT is far larger than 1.572 nm, and is measured up to 11 nm, nearly 7 times of

1.572. Therefore, the chiral index of the CNT should be confirmed as (63, 14). The case of the determination of chiral index of the CNT shown in Fig. 4.13(c) is similar:

$$\alpha = \tan^{-1}\left(\frac{2D_2-D_1}{\sqrt{3}D_1}\right) = 2.833^\circ, \quad (4.3)$$

$$\frac{n}{m} = \frac{2D_2-D_1}{2D_1-D_2} = \frac{1}{17}, \quad (4.4)$$

indicating the CNT with a diameter of 1.372 nm. And the measured diameter from Fig. 4.13(c) is as large as 8.2 nm, 6 times of 1.372. So the chiral index of the CNT should be (102, 6).

For both of the CNTs above, their simple diffraction patterns should result from CNTs with a certain chiral index, instead of a series of certain chiral indices of (um , un), where u is integers. Since the minimum of the difference of d value of the possible two adjacent layers are 1.572 and 1.372 nm, respectively, much larger than 0.34 nm observed in Fig. 4.8. Therefore, the CNTs synthesized in the present work exhibit a single chirality, which is totally novel in the CNTs research until now and consequently may attract more attention to the multi-wall CNTs due to their high conducting properties compared with single-wall CNTs.

4.3 Single-chirality controlling of multi-wall carbon nanotubes

Successful synthesis of single-chirality multi-wall CNTs is important, while elaboration of the behind detailed mechanism responding for the growth process has a more important meaning toward the CNTs research, which gives a fuller understanding of the CNTs for a more precise controlling of CNT-based nanodevices. To achieve that goal, normally TEM and ED techniques are employed to examine the catalysts, the as-grown CNTs and their interfaces to restore as far as possible what happened during the growth process.

A complete system including a single catalyst and the CNT grown on it is necessary the further mechanism research. But it seems a little difficult for sample preparation, because CNTs always break off or catalysts and the CNTs are separated during scratching the products into ethanol before the copper grids salvage.

For a more higher resolution of the TEM images of the catalysts and CNTs, especially their interfaces, smaller diameters of them are beneficial because of the better transmission of electrons on thinner objects. However, smaller diameters of the catalysts and the CNTs also means weaker diffraction intensity and less adjustability of object zone-axis. Empirically, the

catalyst with a diameter of 50-100 nm and the CNTs grown on it with a diameter of less than 100 nm are the best candidates for the study.

The requirements mentioned above prevent most efforts from the truth discovery. Fortunately, some samples survived. And the behind mechanism was elucidated clearly through the precious examination on them. The following paragraphs will show the elucidations from three aspects of variations of catalysts, the determined interfaces and how to grow a CNT, respectively.

4.3.1 Variations of catalyst

The catalysts directly determining the chirality property of the as-grown multi-wall CNTs are confirmed as $(\text{Cr,Fe})_7\text{C}_3$ carbide. And the state of the catalysts maintains constant during the process of CNTs growth, which is regarded as the key factor to get single-chirality CNTs. The detailed crystalline information of the carbide catalyst is shown as follows, which will be cited during the following discussion. Tables 4.3 lists the lattice constants and the calculated interplanar spacings of the $(\text{Cr,Fe})_7\text{C}_3$ phase are listed in the Appendix II at the back of the thesis.

Table 4.3. The lattice constants of $(\text{Cr,Fe})_7\text{C}_3$ phase.

crystal system	trigonal
space group	$P3_1c$
lattice parameters	$a = b = 13.98 \text{ \AA}, c = 4.523 \text{ \AA}$ $\alpha = \beta = 90^\circ; \gamma = 120^\circ$

The diameter of the catalysts is at the range of tens of nanometers, with no preferred growing orientations, which are concluded above. The morphologies of the catalysts tend to be small spheres or small rods. However, they changed a lot during the catalytically growth of CNTs. Fig 4.14 shows the TEM images of the catalysts morphologies after CNTs growth. As can be seen, at the side where nanotube extrusion (growth) occurs, the catalysts deforms to a sharper pyramid, with a very tiny flat at the end, while, at the opposite side the catalysts changed nothing. What's more, the pyramid is axisymmetric along the axis of the catalysts. In

different samples, the facets of the pyramid have different angles with the axis of the catalysts. The most observed values of the angle are 17° and 43.8° . Specifically, the observed angle indicate to be true unless the zone axis is perpendicular to $[0001]$ of the catalysts. Otherwise, the observed value would be larger than the true one. And it is believed that the nucleation and growth of graphene layers are assisted by the dynamic formation and restructuring of the catalysts. Fig. 4.14 (d) shows the scheme of the deformed catalyst, which was called truncated pyramid

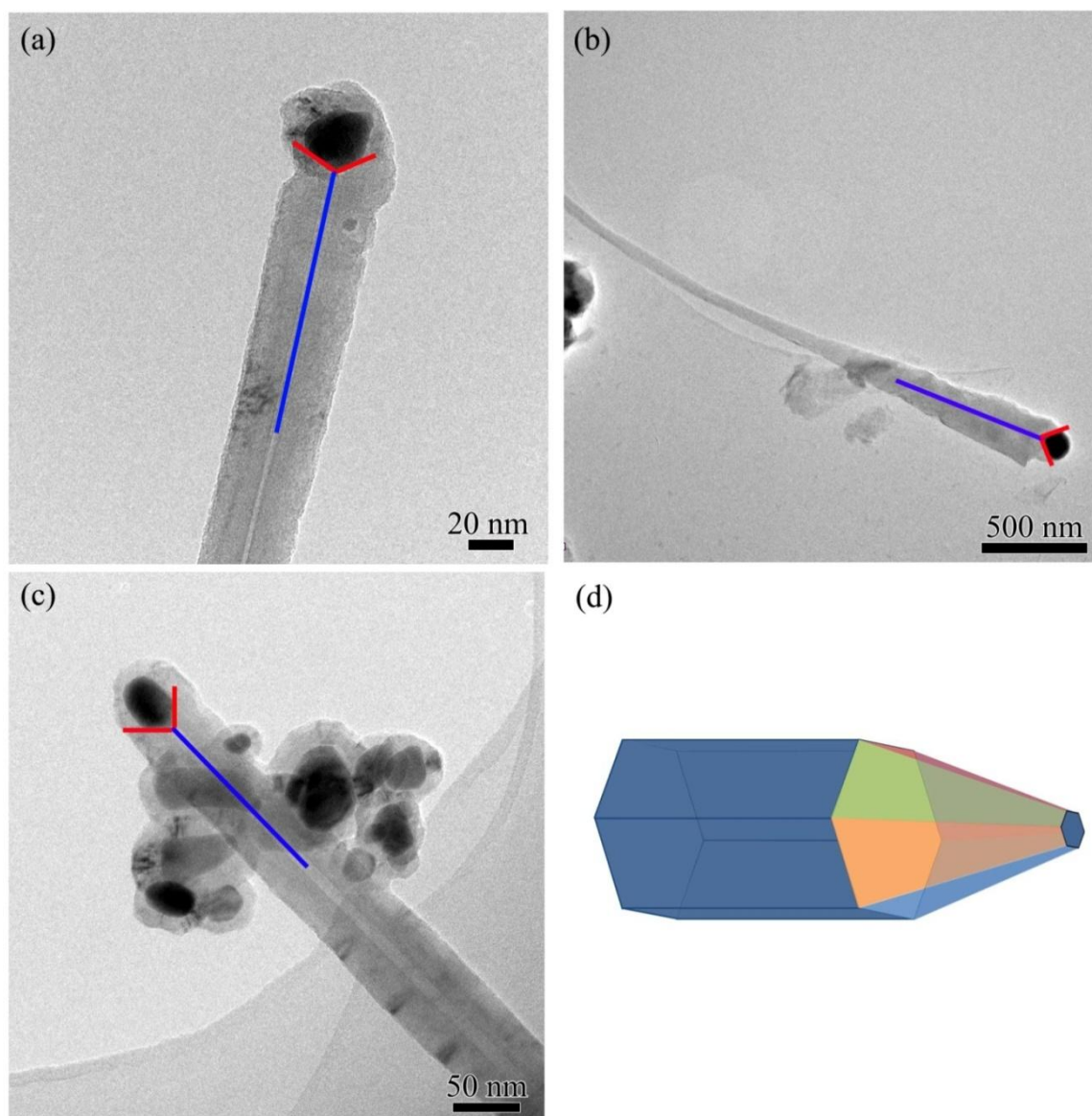


Fig. 4.14. The deformed catalysts after CNTs growth. The red lines and blue lines highlight the deformation of the catalysts and the symmetry axis, respectively.

Detailed HR-TEM images shown in Fig. 4.15 indicated that in the present work the most observed catalysts for the single-chirality multi-wall CNTs growth were grown along their two primary orientations $[0001]$ and $[10-10]$. And for the case of catalyst grown along its $[0001]$ in Fig. 4.15(a), the planes consisting the side walls of the deformed catalysts were confirmed to be $(20-21)$ and (-2021) by examining lattice fringes with a periodicity of 3.6 nm as well as the diffraction patterns shown in Fig. 4.8. According to the spatial symmetry deduced from the space group $P3_1c$ of the catalyst phase, the planes $(02-21)$, (-2201) , $(0-221)$ and $(2-201)$ should also consist the side walls of the truncated pyramid. While for the case of the catalyst grown along its $[10-10]$, shown in Fig. 4.15(b), things got a little rough. Because of the zone axis is not perpendicular to $[0001]$ of the catalyst, the images could not manifest veritably the interaction between the catalysts and the as-grown CNTs. But we could still find the plans $(02-21)$ and (-2201) . Similarly, we can deduce that planes $(20-21)$, (-2021) , $(0-221)$ and $(2-201)$ should all consist the side wall of the deformed catalyst. The TEM images represent two-dimensional projections of the samples, and thus the observations are indicative of graphite layers growth around the catalytic nanocrystals.

Besides the orientation of $[10-10]$, catalysts grown along the orientations of $[-1100]$ and $[0-110]$ would also catalytically grow single-chirality multi-wall CNTs according to the spatial symmetry of space group $P3_1c$. And the chirality of the CNTs should be the same as catalytically by catalysts of $[10-10]$ orientation.

To conclude the discussion above, in the present work, catalysts with orientations $[0001]$, $[10-10]$, $[-1100]$ and $[0-110]$ could catalytically grow single-chirality multi-wall CNTs. And the planes $(20-21)$, $(02-21)$, (-2201) , (-2021) , $(0-221)$ and (2021) play an important role during the process.

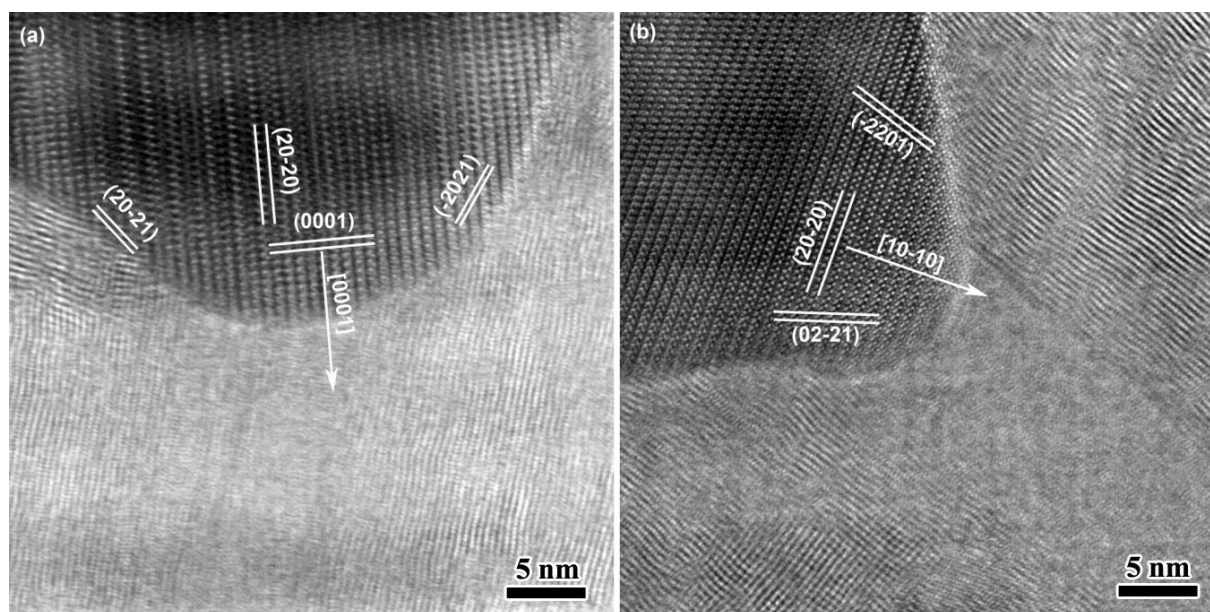


Fig. 4.15. HR-TEM images of the catalysts.

4.3.2 Nucleation of the graphite layers

Compared with the nucleation of single-wall CNTs, that of multi-wall CNTs appears more complex. There is a doubt in front of further study of the nucleation of multi-wall CNTs, which is whether every graphite layer nucleate simultaneously or one layer nucleates first and then other layers nucleate.

An *in situ* observation of the nucleation of carbon nanotubes by the injection of carbon atoms into metal particles²⁵⁰ could give an answer to that doubt. Initially, highly misshapen graphenic network filaments appear to gather in the central hollow core of the tube. A graphene sheet migrates inside the core and when it gets in touch with the FeCo crystal, it becomes attached to the surface. As soon as the metal tip surface is covered by the graphenic structure in the cavity above it, the metal tip, which was formerly flat, appears to deform into an nearly hemispherical dome, and steps develop around the tip. Either simultaneously or shortly thereafter, the dome appears to be covered by a hemispherical graphenic cap (presumably a fullerenic half-cage), whose inner surface fits the dome essentially perfectly. As soon as the metal tip is round, nanotube growth starts because the first carbon layer segregating at the metal dome can form the cap of a tube. Almost immediately, three further graphenic caps form, with interlayer separations close to the standard graphite distance, apparently materializing from the particle tip. The caps then become the tips of multi-wall CNTs, whose walls

extrude from the particle, resulting in incipient formation of a new internal section of the original MWCNT.

The finding above clearly demonstrate that for MWCNTs, one graphene layer nucleates first, then shortly thereafter, other graphene layers nucleate. All layers of the newly forming inner MWCNT segments then grow at exactly the same rate, that is, the inner layers grow at the same rate as the outer layers.

In the present work, the results of determining the chiral indices (m, n) of the as-grown CNTs could also be an evidence explaining the MWCNTs nucleation. The previous discussion in Section 4.2.5 revealed that the chiral property of the CNTs were decided by only one graphene layer, the innermost layer. In other words, once the innermost graphene layer nucleates, the chiral property of the CNTs is determined. The carbon atoms in other graphene layers were arranged according to the principle of that of the innermost layer. The detailed process will be discussed later.

After making clear the nucleation sequences, following is the nucleation of the single-chirality multi-wall CNTs. Deducting from the discussions above, the nucleation of the first graphene layer is crucial for the chirality of the CNTs, which is similar with the nucleation of single wall CNT. About the nucleation, there are two questions raised: 1 the nucleation of CNT is dependent on the certain lattice plain of the catalysts or not; 2 the formation of nucleation is forming an open end or a cap as the end.

For the first question, some believed that the energy difference leading to a particular chirality of nanotubes is so small that there is no reason one chirality should be preferred over another. Furthermore, the catalyst particles often show fluctuations in their structure and orientation. Hence strategies for chirality control in this model may be difficult to achieve²⁴⁰. Instead, they thought that the orientation of the catalyst particles is present because of the preferential growth during nucleation. And these well-defined particles have the capability of surface reconstruction to form close packed surface layers capable of templating graphene layers of primitive structures with zigzag and armchair orientation and with a spatial symmetry which is uniaxial and thus compatible with the nanotube.

But more theoretical and experimental work revealed that the CNTs could extrude from the catalyst particles and have a close relationship with the lattice planes of the catalyst connecting to the as-grown CNTs.

S. Reich, et. al.²⁴⁴ focused on the idea for the chirality-selective growth of nanotubes by controlling the type of caps that form on the catalyst at the nucleation stage. Particular caps could be favored by their epitaxial relationship to the solid catalyst surface and the corresponding tubes grow preferentially. Their *ab initio* calculations results showed that lattice-matched caps and tubes were more stable next to a Ni surface than non-lattice-matched structures. And on Ni (111) plane, Ni-C bonding favored armchair edges by a local lattice matching of neighboring C atoms.

Recently, Y. Li, et. al.²⁵¹ reported their latest results about the chirality-specific growth of single-walled carbon nanotubes on solid alloy catalysts. They showed that single wall CNTs of a single chirality, (12, 6), could be produced directly with an abundance higher than 92 percent when using tungsten-based bimetallic alloy nanocrystals as catalysts, which, unlike other catalysts used so far, have such high melting points that they maintain their crystalline structure during the chemical vapor deposition process. This feature seems crucial because experiment and simulation both suggest that the highly selective growth of (12, 6) single wall CNTs is the result of a good structural match between the carbon atom arrangement around the nanotube circumference and the arrangement of the catalytically active atoms in the plane (0012) of the nanocrystal catalyst.

For the second question, F. Ding, et. al gives an answer by utilizing density functional theory to focus on the adhesion between single-walled CNTs and the catalyst particles from which they grow²⁵². It is found that Fe, Co, and Ni, commonly used to catalyze SWCNT growth, have larger adhesion strengths to MWCNTs than Cu, Pd, and Au and are therefore likely to be more efficient for supporting growth. The calculations also show that to maintain an open end of the SWCNT it is necessary that the CNT adhesion strength to the metal particle is comparable to the cap formation energy of the CNT end. This implies that the difference between continued and discontinued CNT growth to a large extent depends on the carbon-metal binding strength. Therefore, the CNTs catalyzed by Fe, Co and Ni tends to form an open end, while CNTs catalyzed by Cu, Pd and Au are willing to form a cap.

In the present work, multi-wall CNTs were observed to extrude from the nanosized $(\text{Cr, Fe})_7\text{C}_3$ catalysts. Obviously, the adhesion between single-walled CNTs and the catalyst particles is strong and the as-grown CNTs tend to form open end, which coincides with our experiment results. As discussed in Section 4.3.1, the catalysts grow mainly along two orientations: $[0001]$ and $[10-10]$. And consequently the lattice planes on which CNTs extrude from, are different, (0001) and $(10-10)$ planes, respectively. Therefore, the as-grown CNTs have different chiral properties.

For the catalysts with growth orientation along its $[0001]$, the CNTs nucleate on the (0001) plane of the catalysts, and the circle edge is confined in a hexagon which is consist of six intersections of $(20-21)$, $(02-21)$, (-2201) , (-2021) , $(0-221)$ and $(2-201)$ with (0001) . And the CNTs were confirmed to be zigzag tubes, and the chiral index was $(102, 0)$, shown in Fig. 4.16(a) and (b).

For the case of catalysts with growth orientation along its $[10-10]$, the CNTs nucleate on the $(10-10)$ plane of the catalysts, and the circle edge is confined in a hexagon which is also consist of six intersections of $(20-21)$, $(02-21)$, (-2201) , (-2021) , $(0-221)$ and $(2-201)$ with $(10-10)$. And the CNTs were confirmed to be zigzag tubes, and the chiral index was $(105, 10)$, shown in Fig. 4.16(c) and (d).

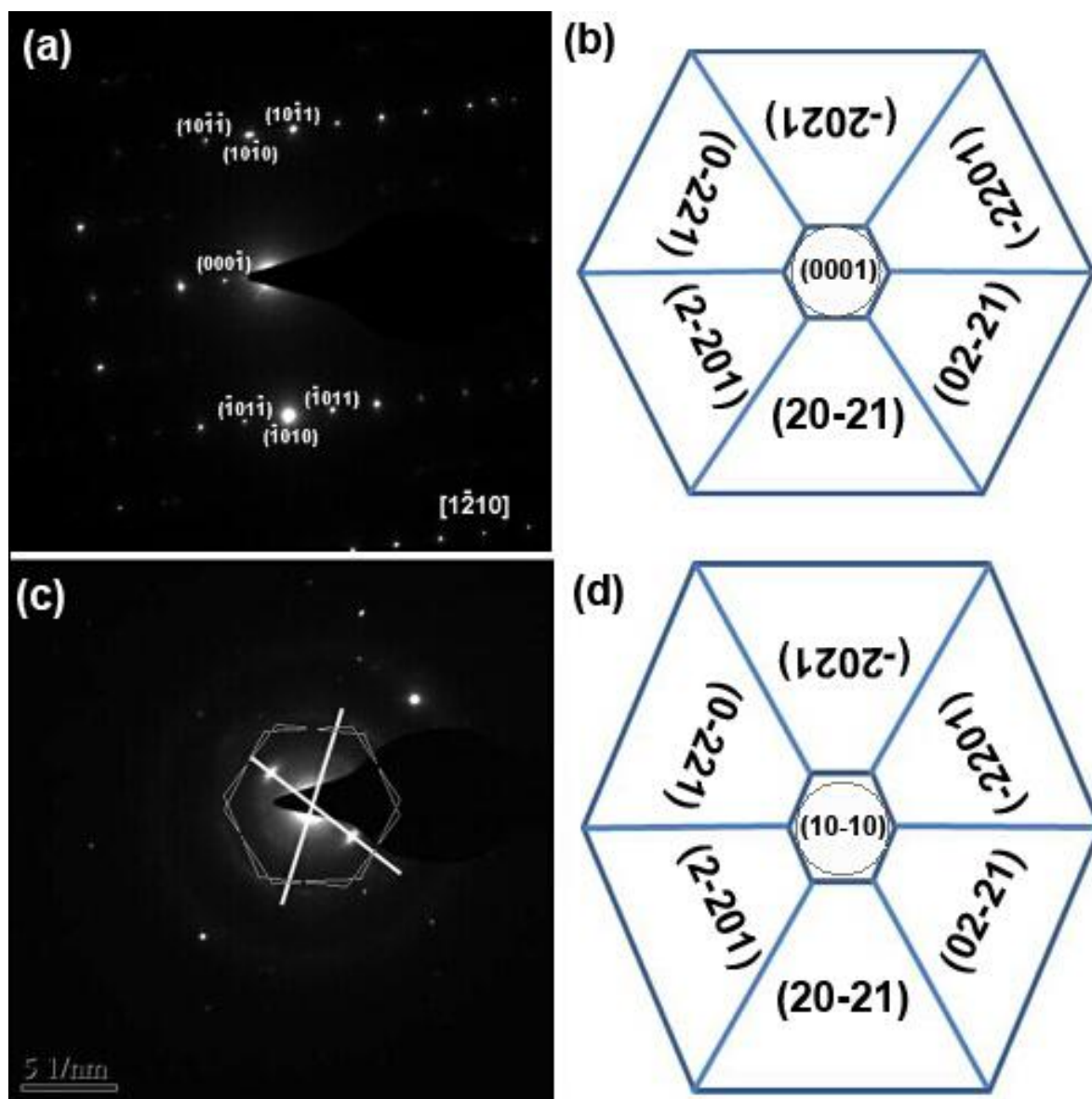


Fig. 4.16. The nucleation of the CNTs on (0001) and $(10-10)$ planes of $(\text{Cr,Fe})_7\text{C}_3$ catalysts.

Once the first graphene layer nucleated, the chiral property of the CNTs would be confirmed. And other layers nucleated shortly thereafter. Normally, the adjacent layers have no structural relationship in the multi-wall CNTs reported before, which, as a consequence, causes the complexity of the chirality. However, all the layers grow according to the chirality confirmed by the earliest graphene layer. Therefore, the as-grown CNTs have a single chirality. And the reason account for this novel phenomena will be discussed in the following section.

4.3.3 Step-site controlling the single-chirality

Step-type sites were firstly found to be most effective where metal atoms were used for dissociation of the reacting molecules for a class of catalytic reactions. And This has also been shown experimentally in several cases²⁵³⁻²⁵⁵.

Normally, on a certain catalyst, there are at least two kinds of active sites for dissociation of the reacting molecules: one associated with certain step sites on the surface, and another associated with the close-packed planes. A theoretical work utilizing density functional theory (DFT) calculations over a Ni(111) surface and over a stepped Ni(211) surface²⁵⁶, indicated that the steps are more reactive than the close-packed surface for most of the elementary steps in the process and atomic carbon has much higher stability on steps than on terrace sites. Therefore, although it should have more surface sites available because there are more facet sites than step sites except for extremely small particles, any nucleation of graphite on the surface of a Ni particle should start at steps.

In the case of the carbon nanostructures synthesis, the step-type sites were firstly observed to act a key role in an atomic-scale imaging of carbon nanofibre growth by catalytic decomposition of methane over a catalyst consisting of Ni nanoclusters supported on MgAl_2O_4 ¹⁸⁴.

As to the growth of single wall CNTs, the step-site was also found to be of significance in the CNTs nucleation period. In the present work, the step-site acted as the nucleation sites for the single chirality multi-wall carbon nanotubes. The HR-TEM images of the interfaces of the catalysts and the as-grown CNTs is shown in Fig. 4.17. And the cases of the catalysts with the orientation of [0001] and [10-10] correspond to Fig. 4.17(a) and (b), respectively.

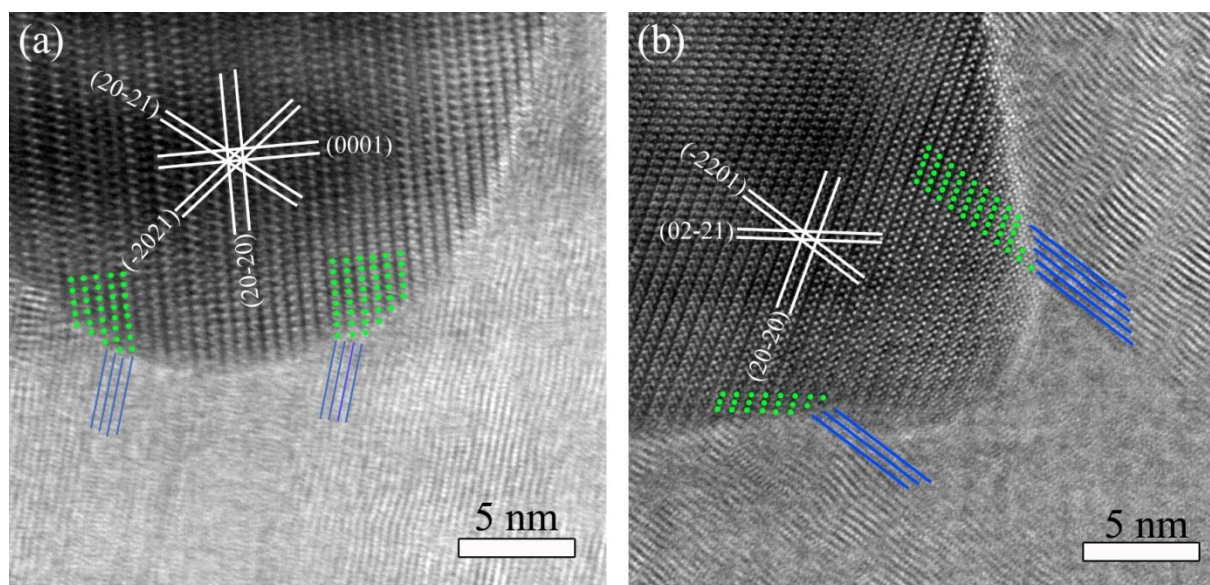


Fig. 4.17. The HR-TEM images of the interfaces of the catalysts and the as-grown CNTs. (a) and (b) correspond to the catalysts with the orientations of $[0001]$ and $[10-10]$, respectively. The green pots highlight the atoms of the catalysts, and the blue lines stand for the graphite layers.

From the pictures above, we can deduct that the graphite layers of the as-grown CNTs extrude out of every monoatomic step site. And the three dimension monoatomic step site is consisted of seven crystal planes of the catalyst. Six of them are the planes discussed in Section 4.3.1. They are $(20-21)$, $(02-21)$, (-2201) , (-2021) , $(0-221)$ and $(2-201)$. And the last one is the basal plane. Through examining all the samples, two most frequent observed are (0001) and $(10-10)$. And this can also be an evidence for the not so large quantity of the CNT products. Since the orientation of the catalyst is random. The catalysts grown with other planes as the basal plane cannot catalyze the growth of the novel CNTs.

The step sites not only acted as the optimum nucleation site for graphite layers, but also determined the single-chirality of the as-grown CNTs. As has been discussed already, for some catalysts, the catalytic single-wall CNTs could have a certain chiral property. In the present work, the discussion above has confirmed that sing-chirality CNTs could be gained on (0001) and $(10-10)$ crystal planes of the catalysts. In other word, single-wall CNTs with a certain chiral angle tend to grown on the certain planes of the catalysts. Because of almost the same growth mechanism on (0001) and $(10-10)$ crystal plane, we select the catalyst with (0001) as its basal plane for discussion.

On the (0001) crystal plane of the catalyst, the first monoatomic step site should be formed before the nucleation of the innermost graphite layer. The position of the nucleation site seems like stochastic. And the step site is consisted of seven crystal planes mentioned before. Shortly after the formation of the step site, a graphite layer nucleated. This layer have a certain chiral property corresponding to the (0001) crystal plane because of less mismatch between the catalyst and the CNTs and lower energy consumption. Based on our observation, the diameter of the innermost layer is more than 5 nm, relatively larger than that of other CNTs reported on the literatures.

The deformation of the catalysts were confirmed rapidly and accomplished at a very short time so that all the graphite layers can grow with nearly the same length to form a tube. Shortly after the formation of the first step site, the second step site formed. To gain the graphite layer with the same chiral property with the innermost layer, two necessary conditions should be met. One is the step site with the basal plane of (0001), while the other is the graphite layers nucleated on these two step sites have a distance of 0.334 nm, which is the nature of the graphite.

The step sites in the present work just met the requirement very well. The interplanar distances of crystal planes (20-21), (02-21), (-2201), (-2021), (0-221) and (2-201) are the same, 0.3623 nm, which is close to the required value of 0.334 nm. From Fig. 4.17, we can see that the graphite layers of the tube were attached to the crystal by forming a strained quasi-coherent interface. The graphite layers were curved close to the interface so that they match the open lattice planes of the catalyst. Owing to interfacial strain, the lattice of the metal appears locally dark, which is known as diffraction contrast from TEM studies of strained-layer epitaxy. Therefore, the difference between the interplanar distances of the catalysts and the graphite could not be a puzzle.

Meanwhile, the same interplanar distances of the crystal planes (20-21), (02-21), (-2201), (-2021), (0-221) and (2-201) could ensure that the lower step site have the same basal plane (0001) with the higher step site. Therefore, it is possible that the graphite layers extruded out of the adjacent step sites have the same chiral properties.

As we know, the chiral property of the single-wall CNTs has a close relationship with its diameter. Normally, the CNTs with different diameters cannot have the same chiral property.

But in our work, the multi-wall CNTs have a single-chirality indeed. The reason for the novel products can be explained as follows.

Firstly, a relatively larger diameter of the hollow interior of the novel CNTs is essential, because of a stronger tolerance of defects compared with that of CNTs with a small diameter. In our previous discussion, we found that the hollow interior of the CNTs were larger than 5 nm and the it could be up to even 10 nm. In this case, a bit larger in the diameter of 0.334 could not cause a big energy consumption, compared with that of the chiral property changing to others of the CNTs on (0001) plane²⁵⁷. Obviously, the increase of the diameter definitely brought in defects. With increasing the number of layers, the more energy resulted from the defects could not be ignored. The tubular morphology changed into facets. Fig. 4.18 shows the possible maximum numbers of the graphite layers exhibiting the tubular morphology we observed. The numbers are several to a dozen. They are relatively minority, compared with the outer tens or even one hundred layers.

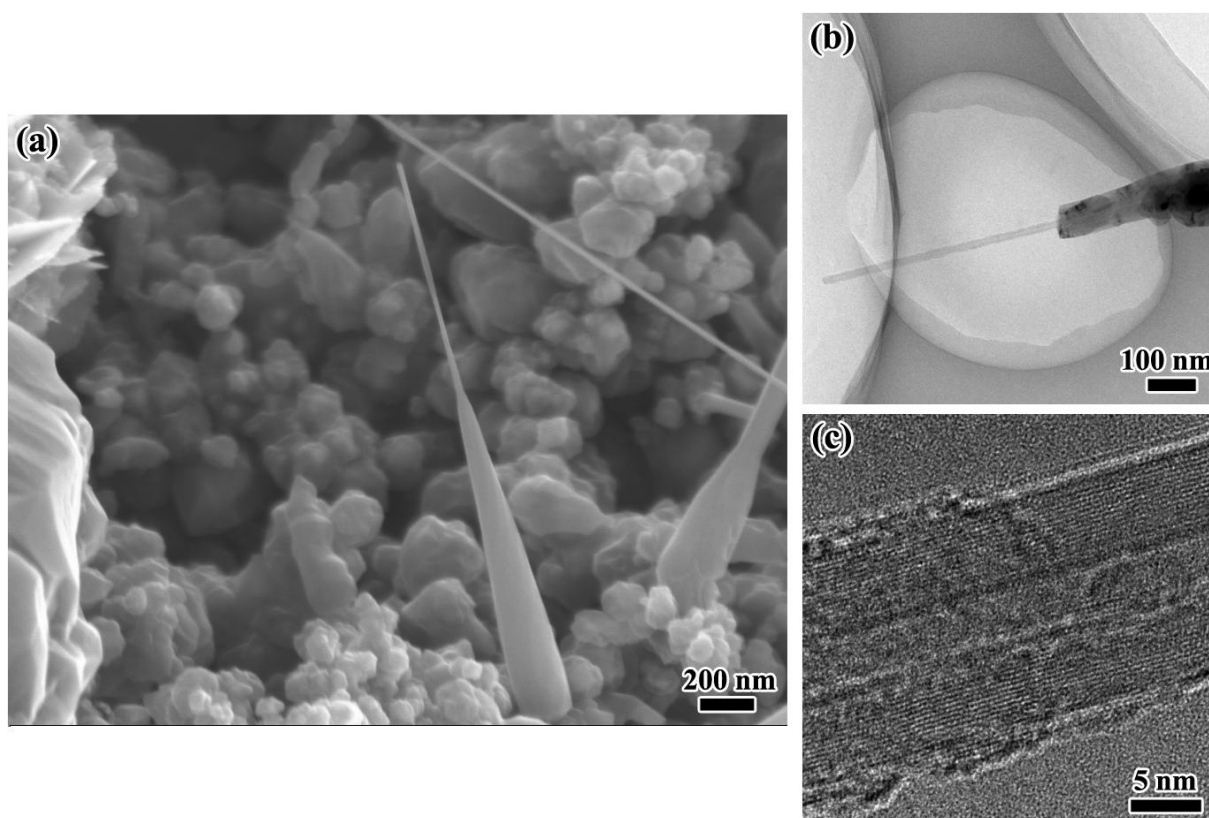


Fig. 4.18. The possible numbers of the graphite layers exhibiting tubular morphology.

Secondly, the stacking of the carbon atoms directly determined the chiral property of the as-grown CNTs. For the inner graphite layers, carbon atoms were stacked consistently according to the means of CNT with a certain chirality, although defects would result in some disorder in axial direction. Consequently, The chirality of those graphite layers is single. But for the outer layers, because the nucleation of them were polylateral but not circle, the stacking of carbon atoms would be more complex.

The results shown in Fig. 4.19 may give us an answer to the complex question mentioned above. Fig. 4.19 shows the SEM images of the side wall and the hollow interior of the zigzag CNT catalyzed by the (0001) plane of the catalyst. From the Fig. 4.19(a), we can see that the adjacent dot spacing is 0.20 nm, and interlayer spacing is 0.334 nm. Dots within one layer do not face directly those of the adjacent layer, but instead stagger roughly 1/3 of 0.20 nm along the axial direction, which shows that adjacent layers are ordered.

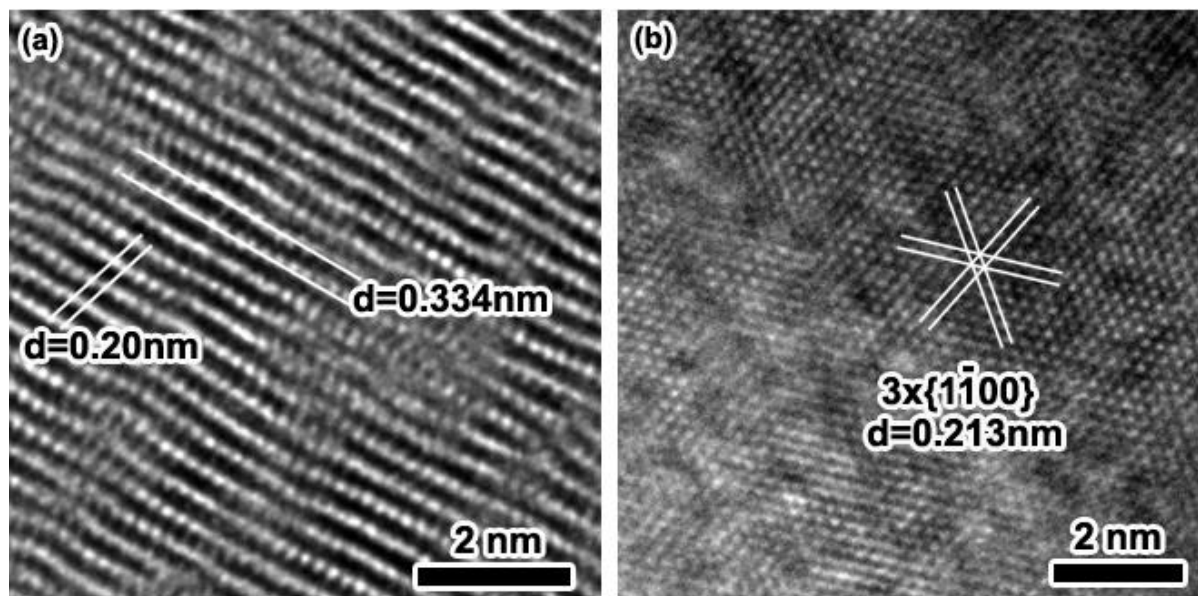


Fig. 4.19. The side wall and hollow interior of the zigzag CNT catalyzed by (0001) plane of the catalyst.

Zigzag nanotubes is one of the two typical types that give rise to separated dots when the incident electron beam is perpendicular to the tube axis. And the other ones are armchair nanotubes. Given that the sp^2 C-C bond length of hexagonal graphite is 0.142 nm, the theoretical values of the distance between two adjacent projective spots of a zigzag tube is 0.213 nm. The experimental value of about 0.21 nm coincides quite well with that of the zigzag tube,

and the $1/3$ of 0.21 nm stagger of adjacent layers coincides with ABAB. . . stacking of cylindrical graphite sheets.

From Fig. 4.19(b), hexagonal patterns are observed at the central region with interstripe spacing of about 0.21 nm. The patterns also coincide with those of graphite when the incident electron beam is along its c-zone axis. When an AB unit of the layers in a bulk graphite crystal is viewed along its c axis, all sites occupied by carbon atoms can be divided into two groups: one group of sites is occupied by one atom and another by two atoms. These sites with two atoms will contribute to the pattern of the hexagonal network in the images. In the present case, although the graphite layers of the CNTs' wall are cylindrical, a slice of graphite layers can be deemed flat. Thus, a hexagonal pattern can always be observed in the central region only if the cylindrical graphite layers are ABAB. . . stacking and the incident electron beam is perpendicular to the cone axis, especially when the outer graphite layers have small curvature.

Consequently, all the graphite layers of the as-grown zigzag CNT should have the ordered stacking sequence, namely, ABAB.... Otherwise, the separated dots staggering roughly $1/3$ of 0.20 nm along the axial direction and the hexagonal patterns in the hollow interior of the CNT would not be observed at all. In other words, the carbon atoms of all the graphite layers from innermost to outermost are stacked orderly. As a result, the whole layers should have the same chirality.

Owing to the increasing of the number of graphite layers, the defects resulting from the larger and larger diameter could not be ignored. Therefore, the morphology of the CNTs tends to be faceted. According to the SEM observation, shown in Fig. 4.20, the facets were either orthostatic or helical. And normally the numbers of the facets of a CNT is 6, 8, or 12. In retrospect, this phenomenon should be attributed to the nucleation of the graphite layers. When the number of the graphite layers exceeded the possible maximum, normally several to a dozen, the nucleation of the new layers tended to be facets. As the interfaces of the new layer and the catalyst should be the projection of six planes of (20-21), (02-21), (-2201), (-2021), (0-221) and (2-201) on the basal plane of the catalyst. Those six lines were the new positions for the nucleation of new graphite layers. After nucleation, carbon atoms stacked with the same means as the atoms in the inner layers, either orthostatic or helical. The formed facets exhibited either orthostatic or helical morphology.

Another point should be mentioned is that with the increasing of the layer number, some crystal planes with high indices would be joined in as the positions for the nucleation of new layers with the six planes mentioned above. Therefore, the number of the facets for a CNT could be more than 6. According to the symmetry, there would be two or six more planes which could also be the new position. As a result, the number of the facets could be 6, 8 or 12, which coincide well with our observation.

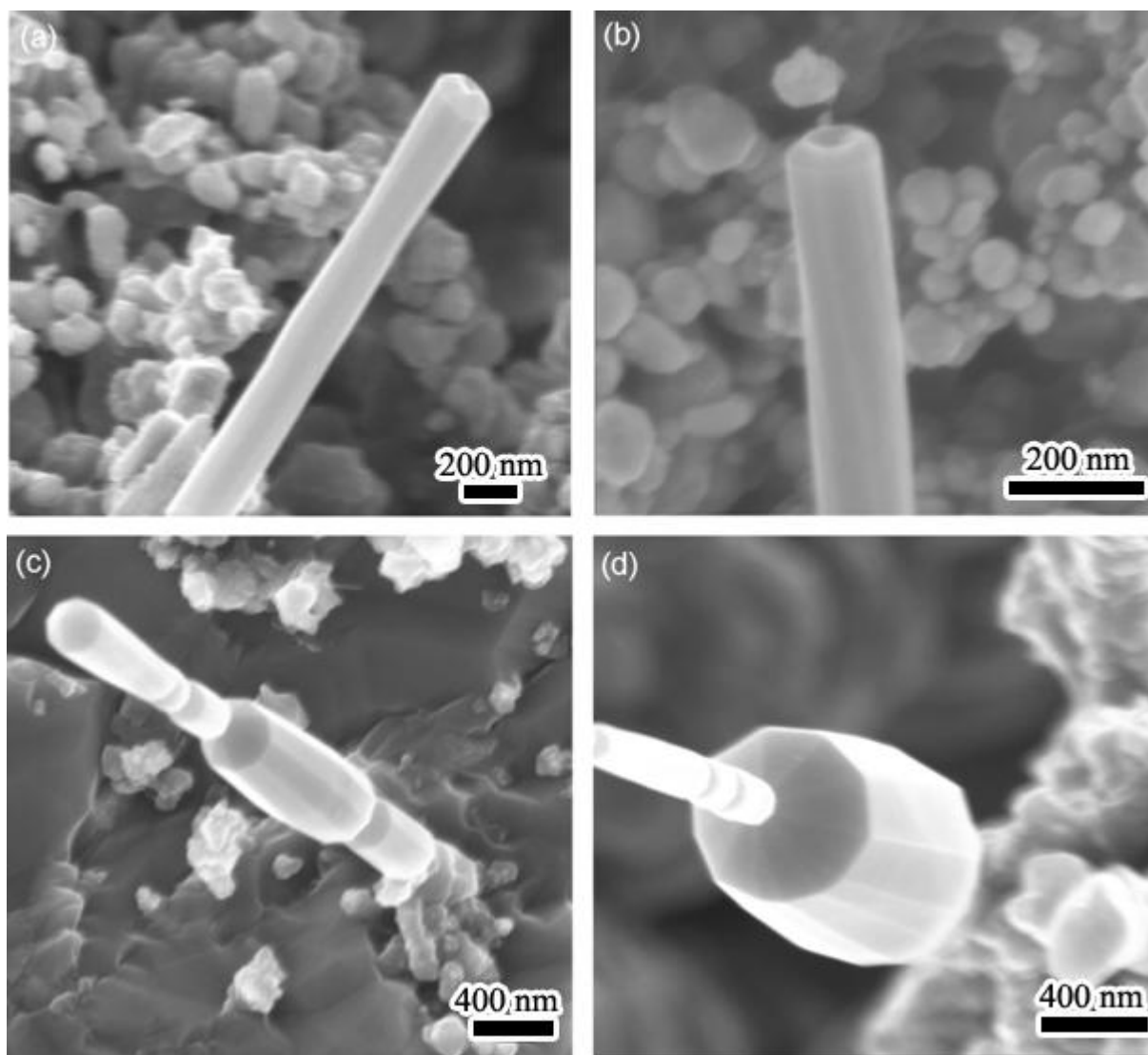


Fig. 4.20. The CNTs with different facets. The number of facets for (a), (b), (c) and (d) are 6, 8, 8 and 12, respectively.

Summing up the discussion above, we can conclude the process of the nucleation of the novel CNTs as follows: firstly, at the basal plane of the catalyst, there would be a monoatomic

step site stochastically, and the innermost layer nucleated, subsequently, the second step site formed shortly after, and the second layer nucleated, and then more and more step sites formed, following with the nucleation of more and more graphite layers. With the increasing of the layers, the morphology tended to be facets. When the monoatomic sites of catalysts were used up, the nucleation of the CNTs ended. Fig. 4.21 shows the schema of the process above. Because of the carbon rich atmosphere, the CNTs would be covered by some amorphous graphite layers. But those layers did not affected the instinct of the CNTs.

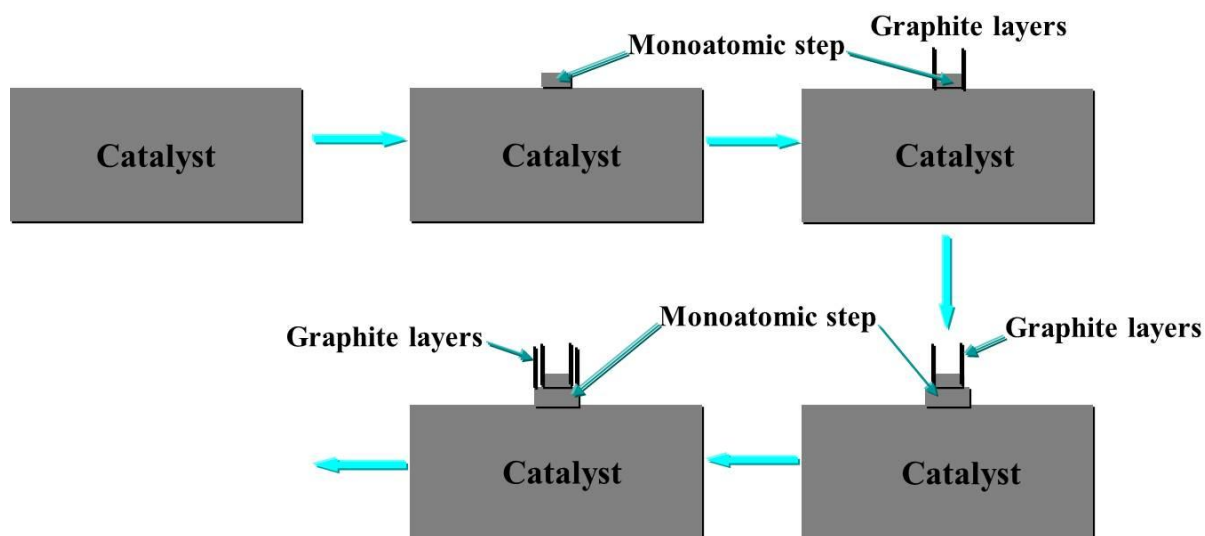


Fig. 4.21. The assumption of the nucleation of graphite layers.

4.3.4 Growing into long tubes

Following the nucleation of the CNTs, with sufficient carbon source, the CNTs would grow along the axis to long tubes. Normally, there are two possible scenarios to explain this growth process.

One is the surface diffusion model. If we assume the supply of carbon atoms by diffusion on the interface of the catalysts and the CNTs, the nucleation and growth of a single graphite layer could happen, but it is difficult to see how such a process could explain the clear evidence obtained in this study that many concentric nanotubes sprout simultaneously and grow at the same rate. As the supply of carbon atoms comes from outside, the atoms would have to penetrate the outer shells of the growing tube to reach the inner shells. The barrier for the migration of carbon atoms through graphene shells by site exchange is 2.3 eV²⁵⁰ (the energy barrier for penetration through closed hexagons without atom exchange would be 10 eV,

which is prohibitively high). Because of the clear direct contact between the growing graphene cylinders and the crystal, there would always be a rather large energy barrier preventing any tunneling of carbon atoms towards the inner shells. Hence, surface diffusion of carbon atoms along the catalyst–tube interface is certainly possible, but one would expect such a mechanism to result in preferential growth of the outermost layers of the new MWNT sections.

Another possibility is the carbide model. Before the nucleation of CNTs, the metal particles have adsorbed enough carbon atoms to form a high-melting-point carbide. And with the increasing of the chamber temperature, the carbon solubility will rise up and more carbon atoms will be adsorbed as the source of the CNTs growth, which has been discussed above. In the bottom-growth process, the catalysts at the root with sufficient carbon source could support all the graphite layers grow at the same rate. Simultaneously, the catalysts will adsorb more carbon atoms from the ambient. These two processes not only ensure the sufficient carbon sources, but also maintain the stability of the catalyst until the growth process stops.

4.4 The ‘visible’ chirality

In section 4.2, we showed the SEM images of the morphology of the novel CNTs. From Fig. 4.12 we can conclude that the growth of the facets of the CNTs have two mode: one is parallel growth, and the other is helical growth. For the former mode, the arrises of the facets are parallel to the axis, namely, the angle between the arrises and the tube axis is 0° . While, for the latter mode, obviously, that angle is no longer 0° , but a certain value of degree. No matter in which mode the CNTs grow, for a certain CNT, the value of the angle is single, which is in accordance with the discussion in section 4.3.

Carefully investigating of the values of the angle, for most tubes, the values are small, 0 or 4~5. For some cases, the value are larger. But examining all the tubes we gained, the values of the angle are in the range of 0 to 30. The fact above raises a question: is it possible that the morphological helix angle and the instinctive chiral angle may have a relationship? If so, the efficient of utilizing CNT-based nanodevices will be dramatically promoted. Since TEM measurement is up to now the only way to check the chirality property of the gained CNTs although it needs much time and effort to spend.

Fig. 4.22 shows the morphological helix of the carbon nanomaterials prepared under the same conditions. A remarkable phenomenon is that during the CNTs growth process, the state of some catalysts were not stable mainly in the aspect of dimension. As a result, the products catalyzed by these catalysts have different morphology, such as nanocones and the nanochains consisting with several nanocones. Fortunately, these products give us the chance to investigate the consecutiveness of the helical morphology.

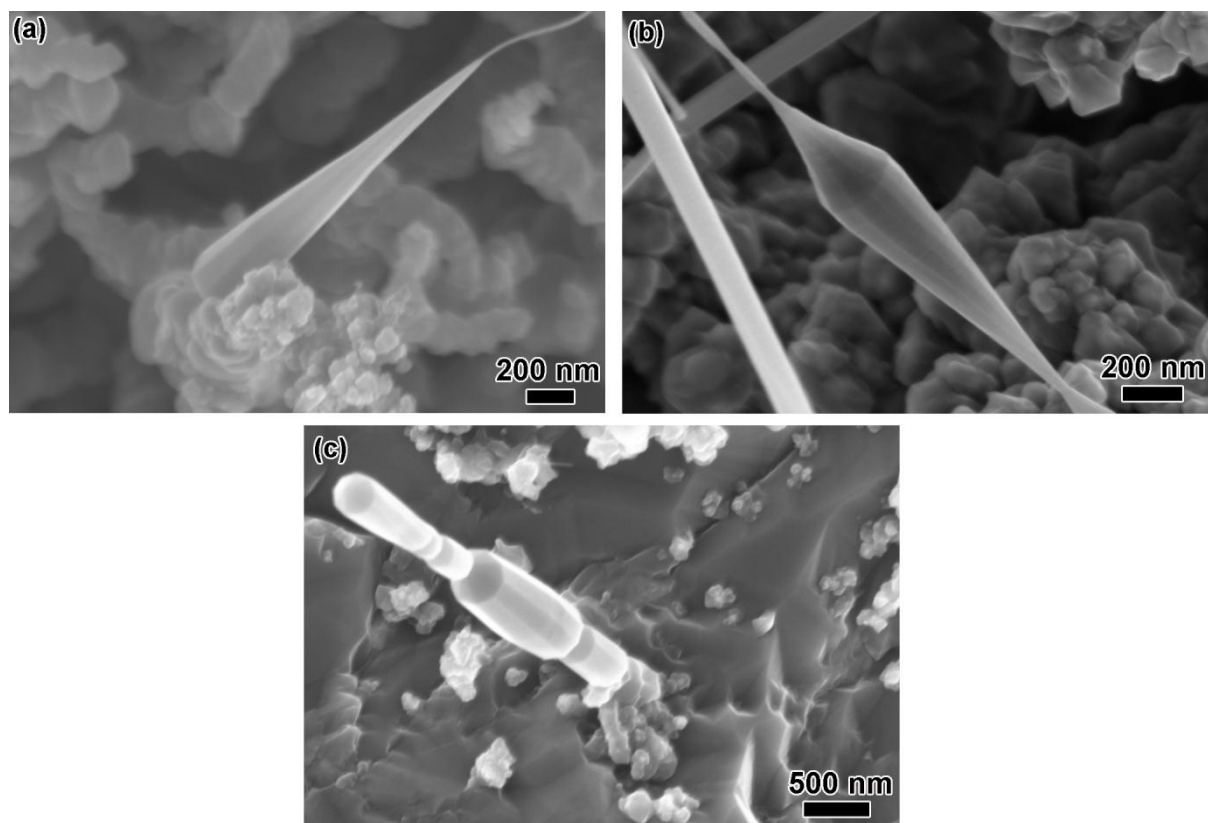


Fig. 4.22. *The morphological helix of the carbon nanomaterials.*

From Fig. 4.22 we can see that the helix morphology is continuous, from the bottom to the top, and from the inner to the outer of the as-grown CNTs. And the helical angles maintain the same for a certain CNT. The helix morphology is the instinct property. As we discussed above, the helix morphology is attributed to the means of carbon atoms stacking. And the latter is determined by the chirality of the graphite layers. Therefore, the helix morphology is relevant with the instinctual chirality of the CNTs.

The facets and the helix morphology induced by the chirality of the CNTs could make the instinctual chirality ‘visible’. The helical angle of the facets could be possible to represent the

chirality of the CNTs. The combined results of SEM images of single CNTs and the corresponding SAED patterns, shown in Fig. 4.23, confirmed that relationship. From Fig. 4.23 (a) and (c), the most common two kinds of CNTs gained in the present work have orthostatic and helical facets. And the helical angle for the latter is 4.5° . The corresponding chiral angles of the two CNTs are 0 and 4.5° , respectively. The helical angles of the facets equal to the corresponding chiral angle of the CNTs.

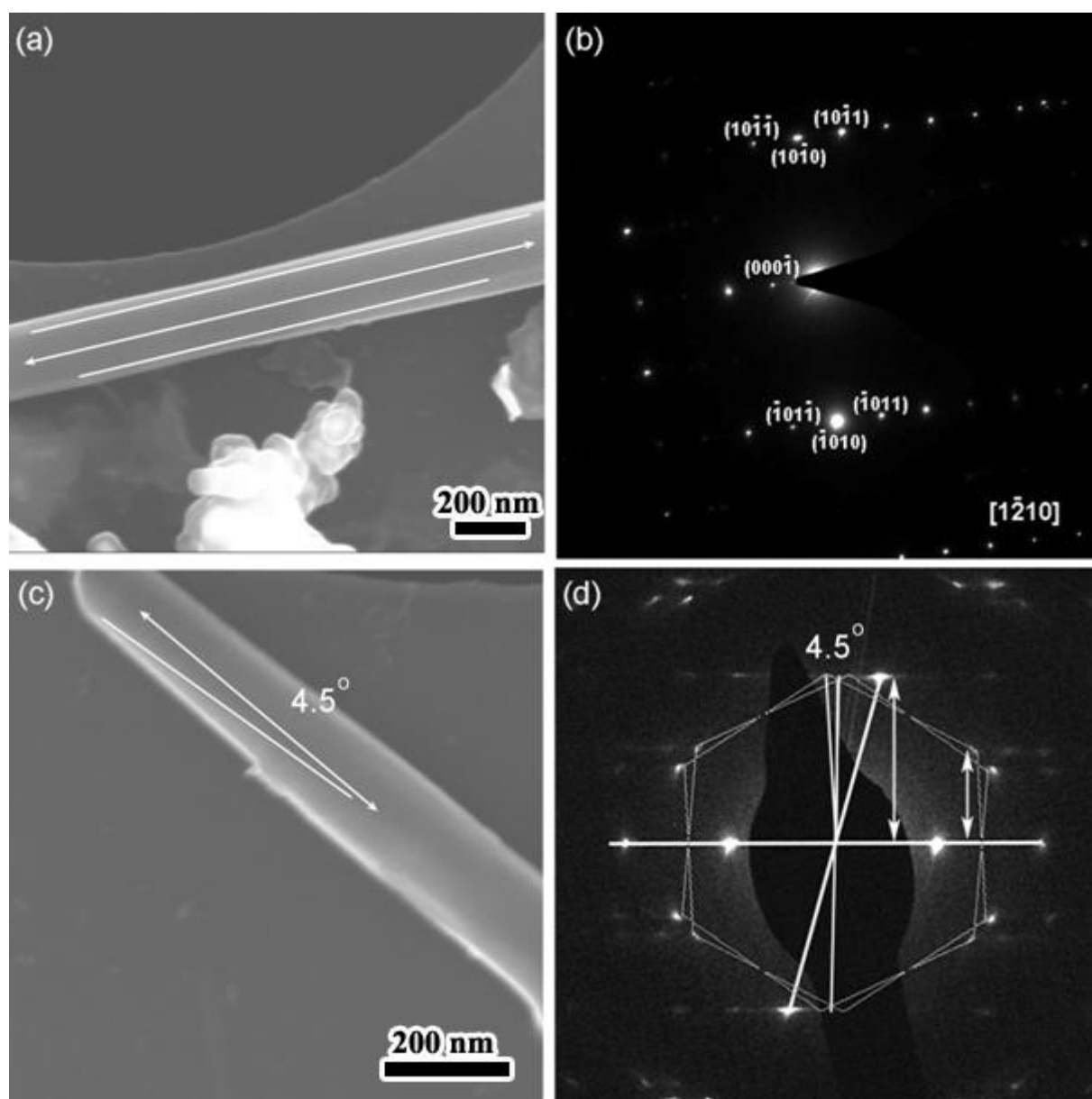


Fig. 4.23. The SEM images of single CNTs and the corresponding SAED patterns of the CNTs. The white lines without arrows highlight the edges of the facets, while the lines with arrows highlight the axes of the tubes.

For all the CNTs, once nucleation happens, the chirality would be determined. In the present work, the nucleation of the graphite layers is determining the carbon atoms arrangement in the circle, which posited to the monoatomic step site and connected with the basal plane of the catalyst. As is believed that, no matter what kind of chirality the CNTs have, the arrangement of carbon atoms during the elongation of the tubes should be the same. Supposed that all the carbon atoms in the circle connected the latter carbon atoms in the means of an armchair mode to form the network of the tube.

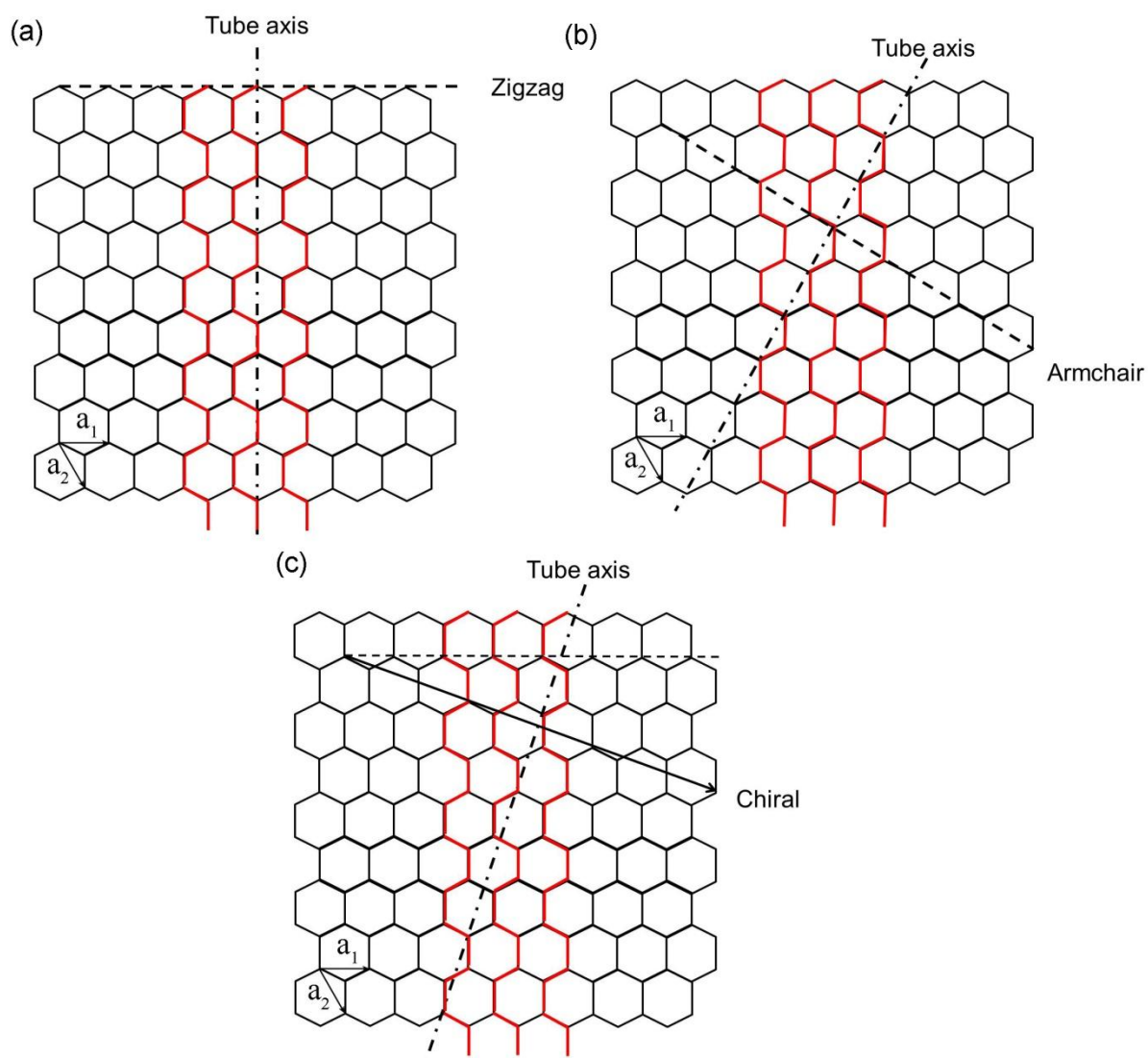


Fig. 4.24. The schematic relationship of morphological helix and the instinctual chirality.

As to a tubular-shape structure, some geometrical relationships can be deal with in a two-dimensional plane. For zigzag nanotubes, a circle of zigzag arrangement of carbon atoms formed after nucleation. The carbon atoms connected the latter atoms in the means of an armchair model. With the increasing of the graphite layers, the facets formed. We suppose that the armchair mode was like the red lines shown in Fig. 4.24(a). With the increasing of the graphite layers, the outer layers turned to be faceted, which was discussed above. The armchair mode would force the arrises of two facets parallel to the tube axis, forming the orthostatic facets, namely helical angel of 0° .

For armchair and chiral nanotubes, the cases turned more complex. The armchair mode would bring a helical facets obviously. According to sample geometrical calculation, we can get that the arrises of the facets would have a certain angle with the tube axes, which equal to the value of the chiral angle.

To sum up, the instinctual chirality make the helical facets of the CNTs in morphology, which is also the result of compromise of keeping the single chirality of CNTs. According to the observation, the visible helical angle of the CNTs equals to the corresponding chiral angle. The armchair model of carbon atoms connecting to the latter atoms coincide well with the result we got. In a word, in the present work, the helical angels represent the instinctual chiral angles and the chirality of the CNTs is 'visible'.

4.5 Raman Spectra Analysis of single-chirality multi-wall carbon nanotubes

Raman spectroscopy is one of the most powerful tools developed for the structural characterization of carbon based materials, such as diamond, carbon nanotube, fullerene, graphene and graphite etc.²⁵⁸⁻²⁶⁵. In particular, it can distinguish the type (multi-wall, metal or semi-conducting single-wall) of CNTs based on the low-frequency radial breathing modes (RBMs) and the unique profile or line-shape of split G bands. While for multi-wall carbon nanotubes, because of the large diameter of the outer tubes and because they contain an ensemble of carbon nanotubes with diameters ranging from small to very large, most of the characteristic differences that distinguish the Raman spectra in SWCNTs from the spectra for graphite are not so evident in MWCNTs. The Raman spectroscopy of MWCNTs has not been well investigated up to now. Thus some new features observed only in MWCNT might be expected. In this

section we investigated the novel single-chirality multi-wall carbon nanotubes utilizing Raman spectra analysis, in order to get the specific features for them.

The group theory for carbon nanotubes predicts that there are 15 or 16 Raman-active modes at $k=0$ for all armchair (m, m) , zigzag $(m, 0)$, and chiral (m, n) ($m \neq n$) nanotubes^{266,267}. The number of Raman-active modes does not depend on the number of carbon atoms in the unit cell, which is given in Chapter 2. A simple explanation for why we get almost the same number of Raman modes for any nanotube is as follows: For lower Raman frequencies, the vibrations can “see” only the cylindrical surface, while for higher Raman frequencies, the vibrations see only the local sp^2 -bond structure of graphite, which is the same for any nanotube.

Fig. 4.25 shows a Raman spectrum taken from an individual CNT. It can be observed that there are specific peaks for the novel CNTs: a low-frequency RBM mode at 270 cm^{-1} , a high frequency G band at around $1588 \pm 2\text{ cm}^{-1}$ and two defect-related peaks: a D band at 1360 cm^{-1} and a D' band at 1620 cm^{-1} . In the following paragraphs, we will discuss RBM peak, G band peak and D band peak, respectively.

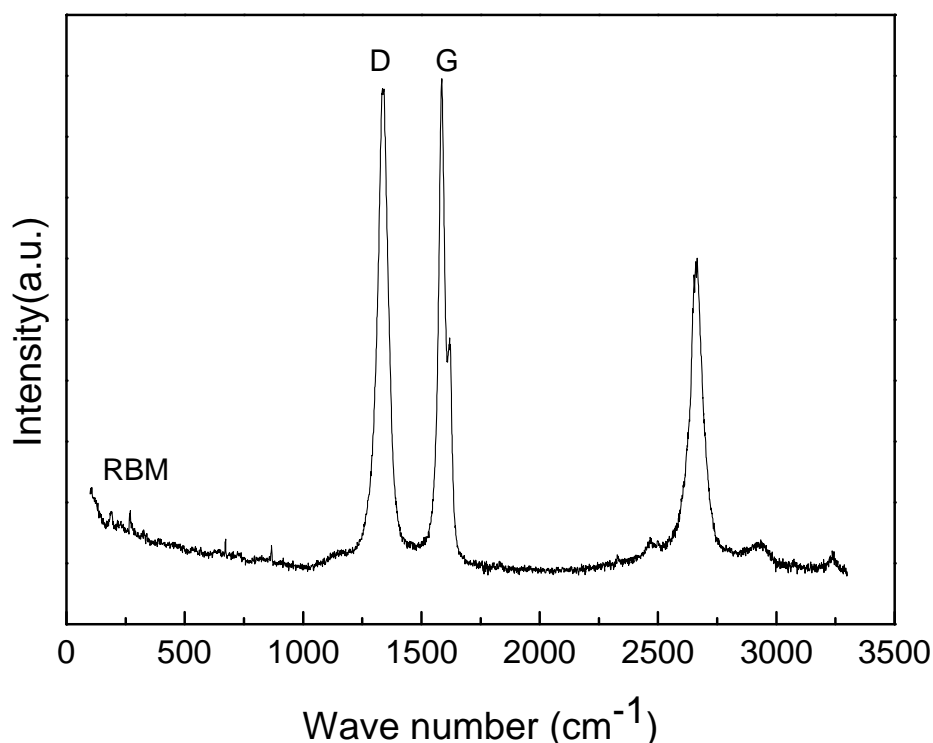


Fig. 4.25. Raman spectra taken from an individual CNT.

The radial breathing mode

The RBM can be used to study the nanotube diameter (d_t) through its frequency (ω_{RBM}), to probe the electronic structure through its intensity (I_{RBM}) and to perform an (m , n) assignment of a single isolated SWNT from analysis of both d_t and I_{RBM} .

The RBM Raman features correspond to the coherent vibration of the C atoms in the radial direction, as if the tube were “breathing”. These features are unique to carbon nanotubes and occur with frequencies ω_{RBM} between 120 and 350 cm^{-1} for SWNTs for diameters in the range $0.7\text{nm} < d_t < 2\text{ nm}$ ²⁶⁸. These RBM frequencies are therefore very useful for identifying whether a given carbon material contains SWCNTs, through the presence of RBM modes, and for characterizing the nanotube diameter distribution in the sample through use of the relation $\omega_{\text{RBM}} = A/d_t + B$, where the A and B parameters are determined experimentally^{269,270}.

Whereas for MWCNTs, the RBM Raman feature associated with a small diameter inner tube (less than 2 nm) can sometimes be observed when a good resonance condition is established^{271,272}, but this is not the usual result, since the RBM signal from large diameter tubes is usually too weak to be observable and the ensemble average of inner tube diameter broadens the signal.

In the present work, a peak with weak intensity was found at a lower frequency of 270 cm^{-1} , shown in Fig. 4.26. And we also regarded it as RBM peak, although the diameter of the inner tube in our products was far more than 2 nm. We attributed the presence of RBM peak to the single chirality of the MWCNTs. The single chirality graphite layers could be treated as many SWCNTs with a single chirality and definitely defects as well. For SWCNTs, single chirality determined the same frequency of the RBM peak. Although large diameter weakened the intensity of RBM peak for each layer, the intensity of RBM peak could be strengthened because of the superposition of peak intensities of all the graphite layers. And the presence of RBM peak was also found in single-chirality TGCs with a larger diameter inner tube.

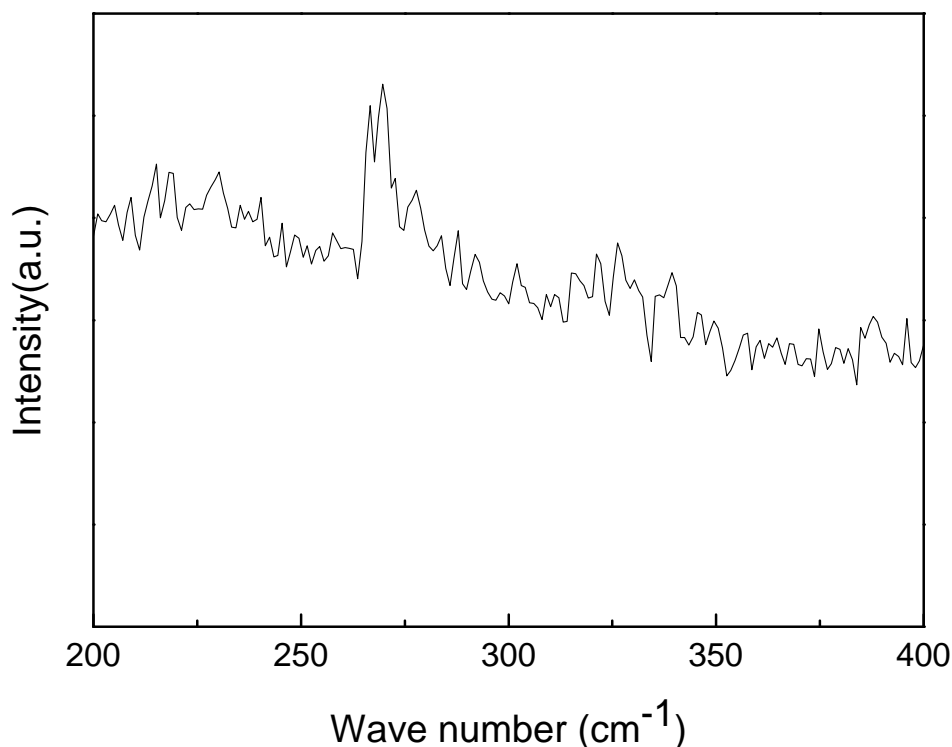


Fig. 4.26. The RBM peak of the novel CNT.

G band

The G-band in graphite involves an optical phonon mode between the two dissimilar carbon atoms A and B in the unit cell²⁶⁸. The corresponding mode in SWCNTs bears the same name. Contrary to the RBM, the G band in SWCNTs shows a more complex spectral feature due to the curvature induced symmetry-breaking effect in the Brillouin zone of SWCNTs. Both theoretical calculation and experimental measurements show that the G band of SWCNTs consists of six Raman-active modes with the symmetry of A(A_{1g}), E₁(E_{1g}) and E₂(E_{2g})^{273,274}. All of these are not always visible or distinguishable, and strongly dependent on the different growth methods used to prepare samples. Usually, in a majority of samples two featured peaks appear: a higher-frequency (ω_G^+) sub-peak at about 1591 cm⁻¹ and a lower-frequency (ω_G^-) sub-peak in the range of 1500 to 1587 cm⁻¹, associated with atomic vibrations along the axis and circumference of CNTs, respectively. Semiconducting and metallic nanotubes are found to have a similar Lorentzian line-shape and an identically narrow FWHM line-width of 6-15 cm⁻¹ for the ω_G^+ peak. A remarkably different line-shape and a dissimilar

FWHM line-width are observed for the ω_G^- peak, i.e., a Lorentzian line-shape with narrow FWHM line-width for semiconducting SWCNTs and a Breit-Wigner-Fano line-shape with broad FWHM line-width for metallic SWCNTs, due to different surface plasmon coupling^{273,274}.

Whereas the $G^+ - G^-$ splitting is large for small diameter SWCNT tubes, the corresponding splitting of the G band in MWCNTs is both small in intensity and smeared out due to the effect of the diameter distribution within the individual MWCNTs, and because of the variation between different tubes in an ensemble of MWCNTs in typical experimental samples. Therefore the G-band feature predominantly exhibits a weakly asymmetric characteristic line shape, with a peak appearing close to the graphite frequency of 1582 cm^{-1} .²⁷⁵

The present G band observed from our novel CNTs is also made of a high-frequency sub-peak and a low-frequency sub-peak, shown in Fig. 4.27. Two sub-peaks may have identical origins as those of SWCNTs, i.e. atomic vibrations along the axis and circumference of CNTs, respectively. The high-frequency sub-peak located at 1589 cm^{-1} is in agreement with those observed for SWCNTs. And the low-frequency sub-peak located at 1575 cm^{-1} has a Lorentzian line-shape with narrow FWHM line-width, indicating a semiconducting property.

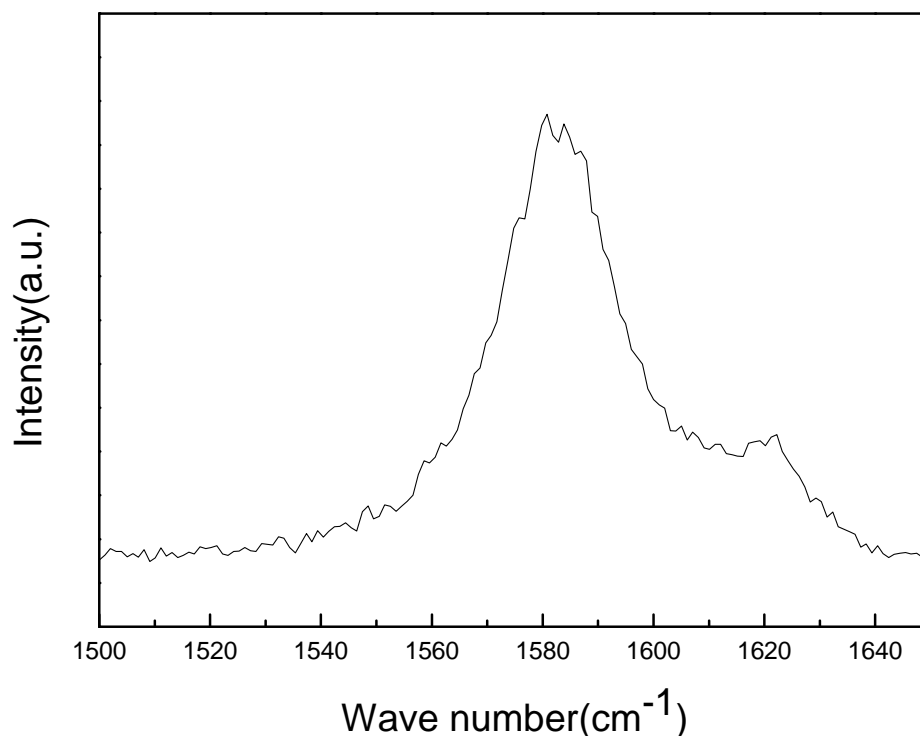


Fig. 4.27. The splitted G band of the novel CNT.

D band

In carbon materials, there are several weak Raman signals whose phonon frequencies change with changing laser excitation energy^{260,276-279} which is called “dispersive” behavior. A typical example of this feature is the D-band at 1350 cm^{-1} whose frequency changes by 53 cm^{-1} as a result of changing the laser energy by 1 eV. Both in graphite and in SWCNTs, the D-band is due to one-phonon, second-order Raman scattering processes. Thus for graphite, the D-band spectra can be fitted to two Lorentzians.

A random D-band intensity variation is observed from one nanotube to another, consistent with the identification of the D-band in carbon nanotubes with defects. To date, there has been no systematic study of the various dependences that influence the D-band intensity.

In the present work, from Fig. 4.32, a D-band peak located at about 1350 cm^{-1} with a relatively high intensity. Both of Shang and Tan reported single-chirality tubular graphite cones with no D-band or a very weak D-band existing in the Raman spectra. However, we believe

that the presence of D-band is reasonable. There are two kinds of defects which can result in the D-band. One is the poor crystallinity of the as-grown CNTs. And the other is the defects caused during the nucleation period which is the result of compromise for single-chirality of all the graphite layers. This is instinctual for single-chirality MWCNTs and dominates the presence of D-band.

To conclude, for single-chirality multi-wall carbon nanotubes, a weak RBM peak, a relatively obvious D-band and a splitted G-band all were present in the Raman spectra of an isolated MWCNT. And these peaks are instinctual for single-chirality MWCNT and can be envisaged as a fingerprint for single-chirality of tubular carbon nanomaterials.

5 Synthesis and photoluminescence property of silicon nitride nanocones

1D nanostructures (wires, tubes, belts, cones and ribbons) are expected to play an important role in the fabrication of nanoscale devices.²⁸⁰⁻²⁸⁷ The utilization of nanoscale materials inevitably requires full control of the structure, size, shape, and the assembly mechanisms, because the intrinsic properties of nanomaterials are determined by their structures, that is, size, shape, composition, and crystallinity.²⁸⁸⁻²⁹⁰

In recent few years, nanocones have emerged as a new kind of one dimensional nanostructure which is superior to nanotubes, nanowires, and nanobelts in some aspects^{48,49}. For example, it is found that nanocones are more potential candidates for scanning probes and field emitters due to their radial rigidity, which eliminates the poor signals and noise caused by mechanical or thermal vibration²³⁰. However, to date the obtained nanocones are still restricted to a very few members such as carbon²³¹, boron nitride²⁹¹, silicon carbide²⁹², aluminum nitride²⁹³ and zinc oxide²⁹⁴ due to the difficulty in preparation.

Si₃N₄ is an advanced material and usually two types of structural modifications exist, namely, metastable, low-temperature-phase trigonal α -Si₃N₄, and stable hexagonal β -Si₃N₄. Si₃N₄ is one of the most important technical ceramics owing to its interesting properties, such as high strength at high temperatures, low density, good resistance to corrosion, wear, thermal shock and creep, excellent chemical stability, and so forth. These properties favor Si₃N₄ as a suitable material for a wide range of technical applications, especially for high-temperature engineering applications.

In this chapter, we report the successful synthesis of β -Si₃N₄ nanocones via a chemical vapor deposition technique, and the growth mechanism and the quantum size affected photoluminescence property of this novel nanomaterial are briefly discussed.

5.1 Synthesis of β -silicon nitride nanocones

The catalyst is crucial for the nanomaterials synthesis process. In this work, we utilized Fe thin films as catalyst, which were prepared by magnetic sputtering on silicon wafers. The thickness of the thin films was 100 nm.

Table 5.1 *The processing parameters for silicon nitride nanocones synthesis.*

Microwave power (W)	Gas pressure (Torr)	Gases flow rate (sccm)
700	12, 15, 18	
750	15, 18, 21	
800	17, 20, 23	
850	19, 21, 25	
900	22, 25, 28	
950	22, 25, 28	
1000	22, 25, 28	
1050	22, 25, 28	
1100	22, 25, 28	Methane flow rate = 5, 10, 15, 20, 25, 30, 35, 40, 45, while nitrogen flow rate keeps 45 sccm.
1150	24, 26, 30	
1200	27, 30, 33	
1250	27, 30, 33	
1300	27, 30, 33	
1350	27, 30, 33	
1400	27, 30, 33	
1450	27, 30, 33	
1500	27, 30, 33	
1550	30, 33, 36	
1600	30, 33, 36	

Similar with the synthesis of single-chirality multi-wall CNTs, there is a narrow space for adjusting the process parameters to get what we want. During the concrete operation of nanocones growth in the present work, there are three adjustable parameters: the microwave power, the gas pressure and the flow rate ratio of methane and nitrogen. The microwave power affects the temperature of the process. High microwave power can bring high temperature atmosphere. Owing to the basic operating requirement of MWCVD technique, a small adjustable range of gas pressure corresponds to a certain value of microwave power. In the small range, the increase of the gas pressure can condense the plasma sphere to elevate the energy of particles. In the case of the flow rate ratio of methane and nitrogen, different ratios lead to products with different content of carbon and nitrogen. Before the synthesis process, a pre-treatment utilizing hydrogen plasma with a gas pressure and the microwave power of 35 Torr and 1500 W, respectively, was needed for purification and preheating the substrates. Table 5.1 shows the attempts for the synthesis of β -silicon nitride nanocones in the present work.

The processing parameters for β -silicon nitride nanocones growth is confirmed as follows shown in Table 5.2. The temperature for the synthesis process is kept as constant, 1100 °C measured by an infrared thermometer. And the repetition of synthesis process is identified to be good.

Table 5.2. The processing parameters for β -Si₃N₄ nanocones growth.

Pre-treatment	Base pressure ($\times 10^{-2}$ Torr)	1.2-1.8
	Hydrogen flow rate (seem)	100
	Gas pressure (Torr)	35
	Microwave power (W)	1500
	t (mins)	30
Synthesis process	Gas pressure (Torr)	30
	Gas flow rate (sccm)	CH ₄ : N ₂ = 15 : 45
	Microwave power (W)	1500
	t (mins)	120

5.2 Characterization of β -silicon nitride nanocones

Fig. 5.1 shows field emission scanning electric microscopy images of a number of β - Si_3N_4 nanocones. As can be seen from the Fig. 5.1(a), the nanocones are only grown on the field with Fe thin films, forming a boundary on the substrates, indicating the crucial role of the catalyst during the growth process. From the enlarged images of Fig. 5.1 (b)-(d), we can find that the roots of nanocones have a wide range in diameter, from several hundreds nanometers up to 1 μm . And the tips vary from several to tens of nanometers. The average length is about 500-600 nanometers and the average tip apex angle is 3-5°. The shape of the nanocones is determined by the ratio of axial and radial (R_a and R_r) growth rates, and the cones are obtained when R_a/R_r is constant.

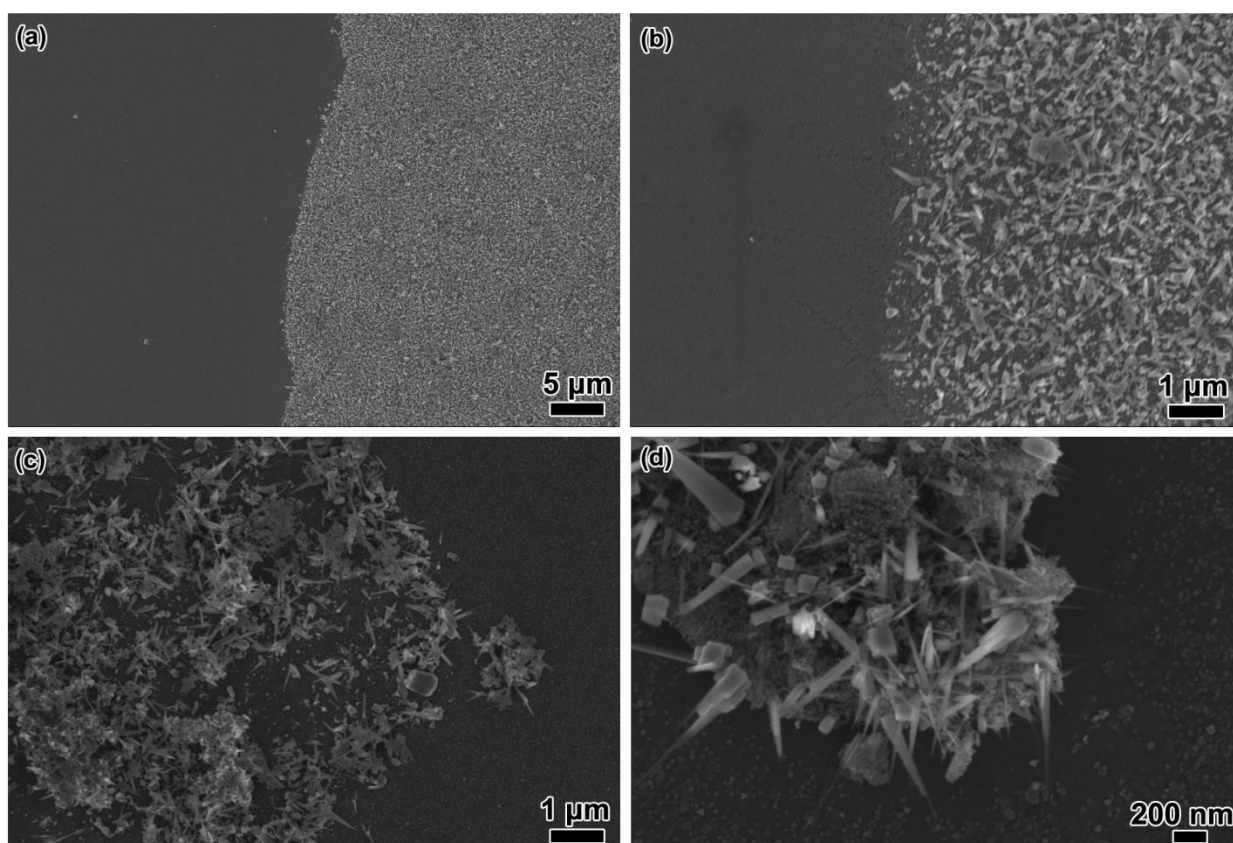


Fig. 5.1. The field emission SEM images of β - Si_3N_4 nanocones.

As can be seen from the TEM images shown in Fig. 5.2, all the β - Si_3N_4 nanocones possess a straight and homogeneous morphology. The uneven brightness of black and white in the TEM image indicates a good crystal structure. As expressed in the Fig. 5.2, the selected area electron diffraction pattern recorded from a nanocone shows clear diffraction spots which suggest a good crystalline nature corresponding to hexagonal β - Si_3N_4 . Otherwise, the (001) face is confirmed and thus indicates a main growth orientation of $\langle 001 \rangle$.

An insight into an individual nanocone is revealed from the high-resolution transmission electron microscopy lattice images, which are shown in Fig. 5.3. The interplanar spacing of 0.29 nm corresponds well to the lattice direction of β - Si_3N_4 [001]. Furthermore, it is observed that the lattice fringes are perpendicular to the cone axes, indicating a [001] growth orientation as marked by the arrow in Fig. 5.3(a) and (b). The SAED and HR-TEM analyses both demonstrate that the β - Si_3N_4 nanocone is crystalline and structurally uniform.

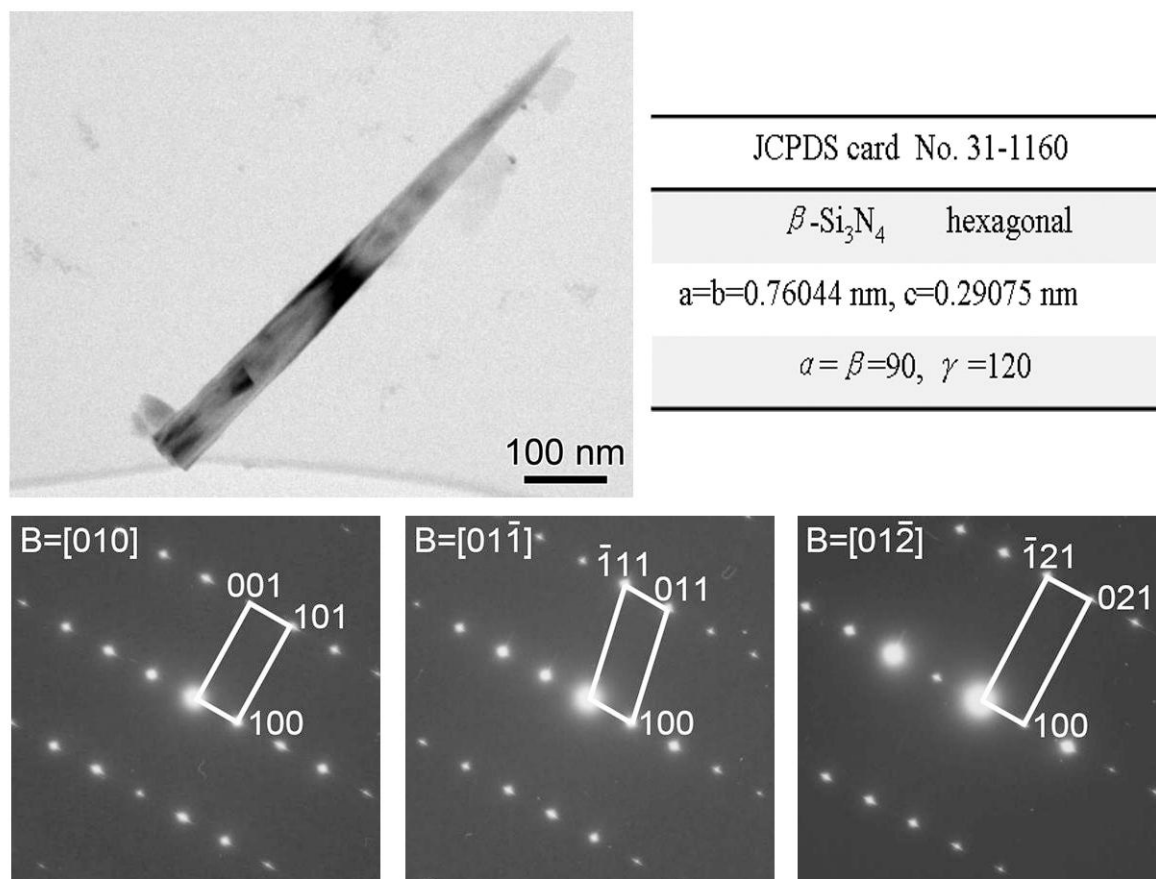


Fig. 5.2. The TEM image and the SAED patterns of β - Si_3N_4 nanocones.

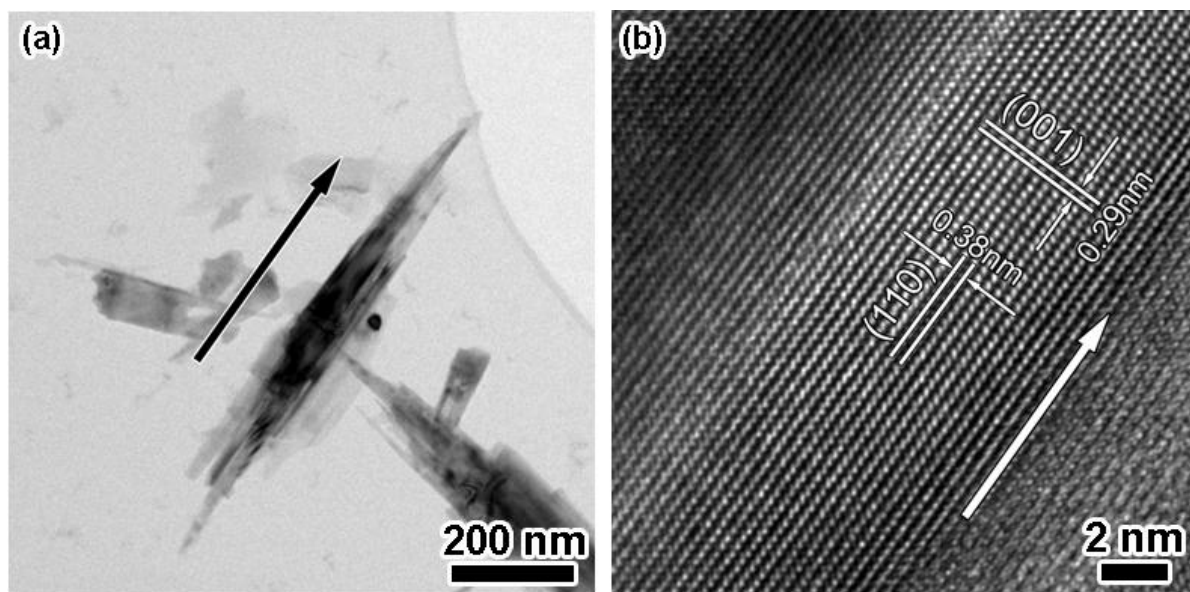


Fig. 5.3. The TEM images of β - Si_3N_4 nanocones. The cone grows with an orientation of $[001]$.

Fig. 5.4 shows the HR-TEM images of the tips of β - Si_3N_4 nanocones. The clear lattice fringes further confirmed the high quality of the Si_3N_4 nanocrystals. In addition, the surface of a β - Si_3N_4 nanocone is clean, with a thin oxide shell of diameter less than 2 nm, which coincide well with the small amount of Oxygen in EDX results. Usually, the oxygen remaining in the chamber during the growth process will slightly oxidize the nanocones. The tiny tip with a high quality in crystalline indicated a good performance of this novel nanocones in the future applications.

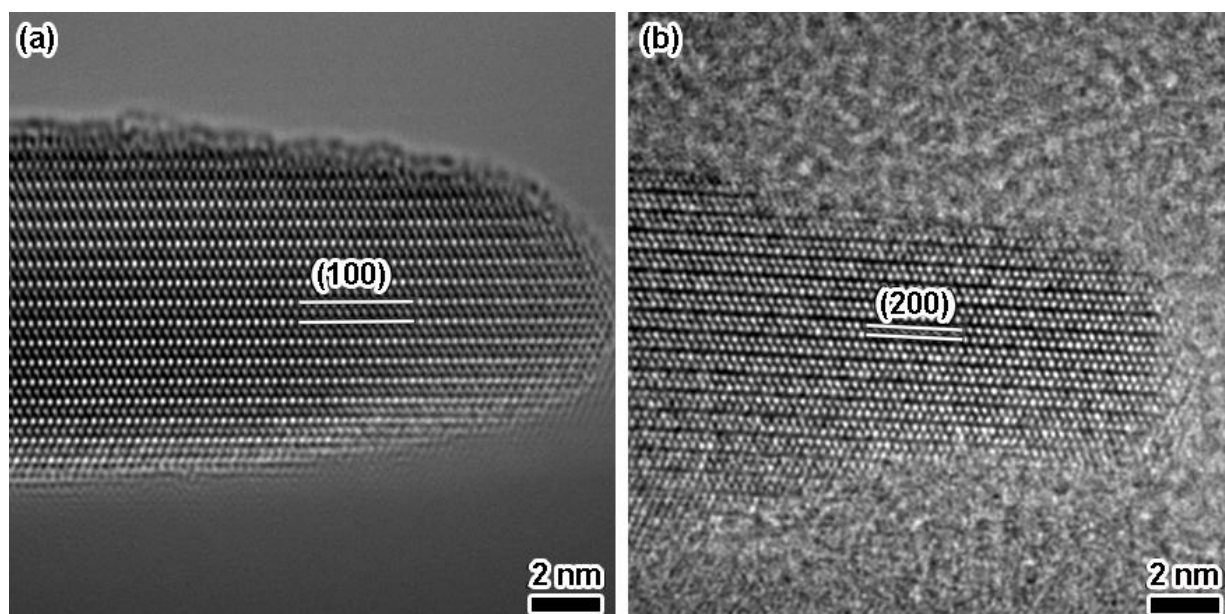


Fig. 5.4. The HR-TEM images of the tips of β - Si_3N_4 nanocones.

The crystal structure of the sample is investigated by X-ray diffraction. Displayed in Fig. 5.5 are XRD patterns of the as-prepared sample. As can be seen from the patterns, peaks with 2θ values of 32.8, 35.2, 38.4, 50.5, 61.7 and 95.0 are well consistent with the planes of (101), (210), (111), (301), (002) and (601) of the standard hexagonal cell of β - Si_3N_4 with the lattice constants of $a = 0.7604$ and $c = 0.2907$ nm (JCPDS card No. 33-1160), respectively. Obviously, no other phases of Si_3N_4 such as α - Si_3N_4 or impurities are detected, indicating a high purity of β - Si_3N_4 phase. The strong intensity and narrow width of the peaks also present a good crystal structure, as shown in HR-TEM images. Besides the β - Si_3N_4 phase, one peak of Si with a strong intensity is synchronously found in the XRD pattern, which originates from the silicon wafer substrate.

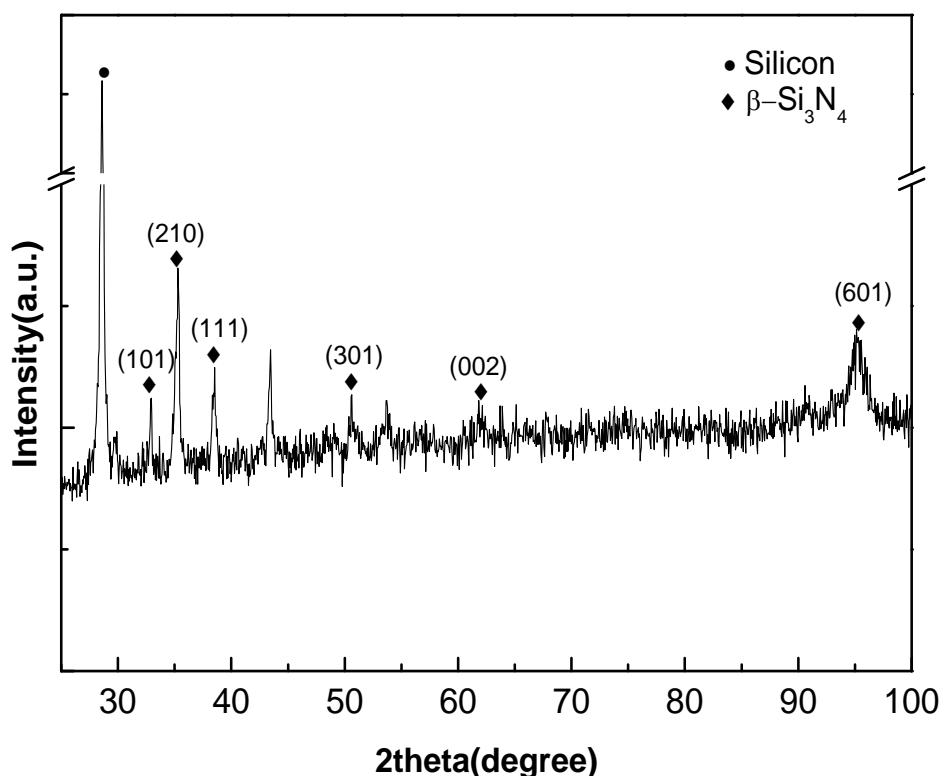


Fig. 5.5. XRD patterns of the as-grown samples.

5.3 Growth mechanism of β -silicon nitride nanocones

As has been mentioned, Fe was used as a catalyst and played a crucial role during the experimental process. As is well known, if no Fe is used the product will be silicon carbide thin film, shown in Fig. 5.6(a). The thin films were not very dense, but smooth and homogeneous. Here we planned a contrastive experiment, which was carried out without Fe thin films on the

silicon wafers, while some Fe particles could be gained from the sputtering from the metal chamber. The results were investigated in detail and shown in Fig. 5.6.

The products were mainly SiC thin films, which was confirmed by the results of EDX. While, some bright lines were observed from low-resolution SEM images, which were shown in Fig. 5.6(b). The lines were several micrometers long. And they were arranged either parallel or perpendicular to each other, which may attribute to the silicon wafers that have a basal plane of (100). Detailed examining the composition of the bright lines by EDX, shown in Fig. 5.7, revealed the present of Fe. The distribution of Fe was not uniform, which could be deducted by the analysis of points on the bright lines. On the bright lines we found the nucleation of a kind of nanomaterials, which was shown in Fig. 5.6(c), (e) and (f). In Fig. 5.6(f), the small nanomaterial was denoted by an arrow. The EDX results confirmed that the nanomaterial were silicon nitride nanomaterials. The disparity of the EDX results and the stoichiometry result from that the EDX results came from the nanomaterial and the silicon substrate. And the latter should be accounted for more percentage.

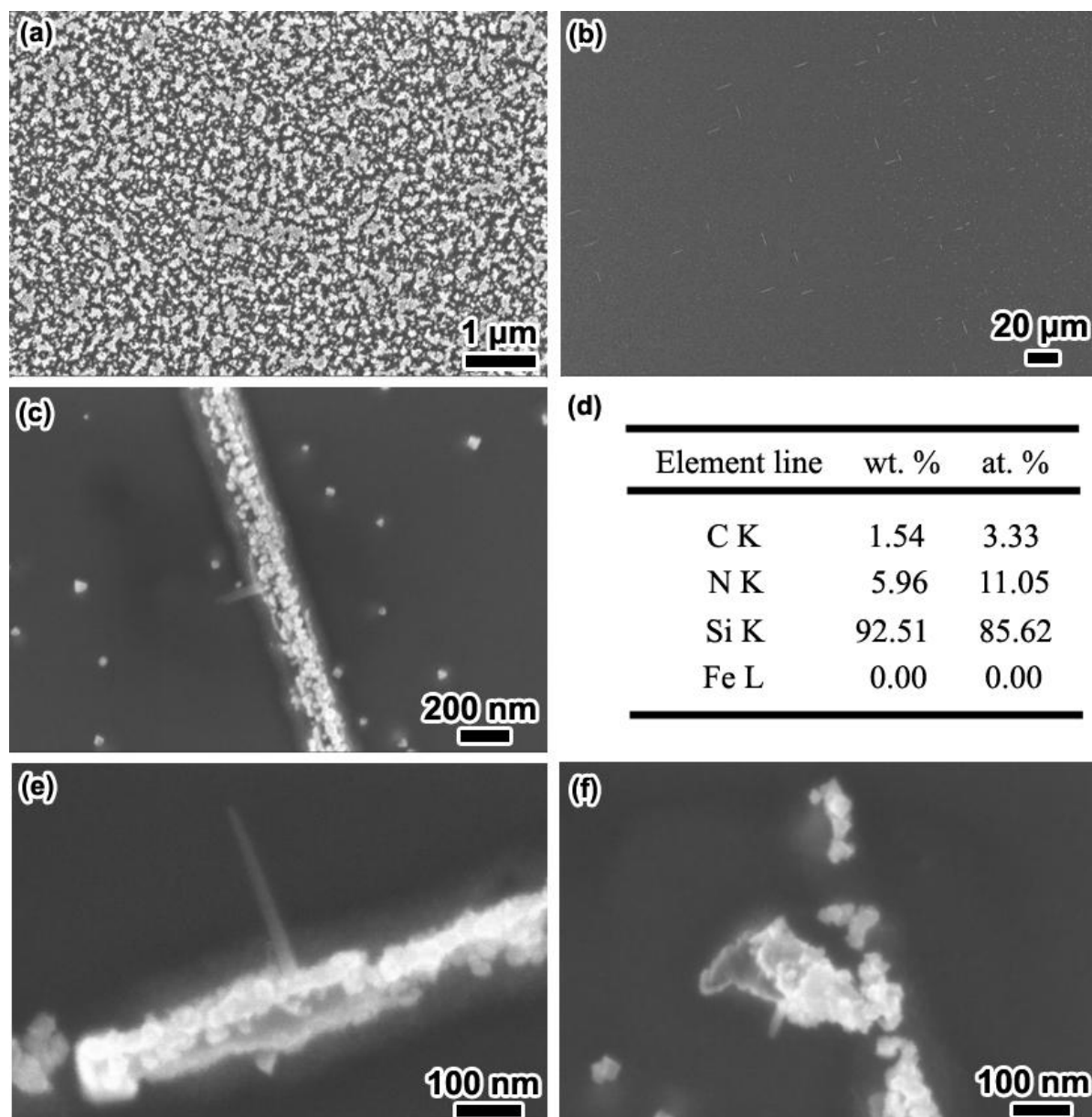


Fig. 5.6. The role of Fe on the growth of β - Si_3N_4 nanocones.

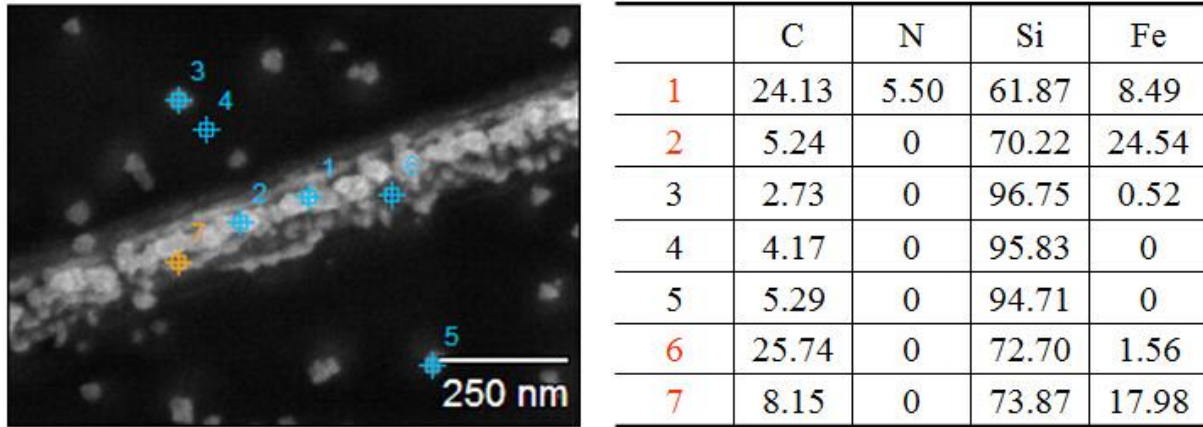
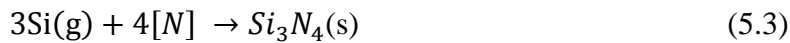
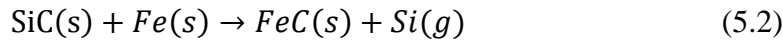
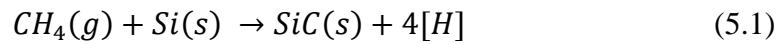


Fig. 5.7. The EDX analysis of the nucleation of β - Si_3N_4 nanocones.

On the basis of the experimental results, a novel growth model for synthesizing β - Si_3N_4 nanocones is suggested. In this mode, methane can easily act with silicon wafers to form silicon carbide thin films. The presence of Fe would destroy the balance of the formation of the film. Instead, Fe atom would deprive C atoms from Si to form a FeC alloy. The Si atoms, which lost the bonding C atoms, will easily bond with nitrogen plasma to form the final products. The corresponding reaction formula is listed as below:



As to the formation of the cone morphology, an interesting fact should be noted first, which is that all Si_3N_4 cones keep their cone shaped structure with nearly the same apex angle no matter when and where the growth is terminated. Thus the cone growth can be reasonably divided into axial and radial directions, respectively, as the schematic in Fig. 5.8. The root-based radial growth is a process of continuous nucleation of new layers outside the inner layers. A layer-by-layer growth model can describe this continuous formation of additional sheets along the radial direction. Simultaneously, the axial growth elongates the formed sheets along the axial direction and keeps the as-formed sticking sequence. The conical shape of the cones was controlled by the axial growth rate and the radial growth rate. Here obviously the former is much larger than the latter, resulting in the very sharp tips of the cones.

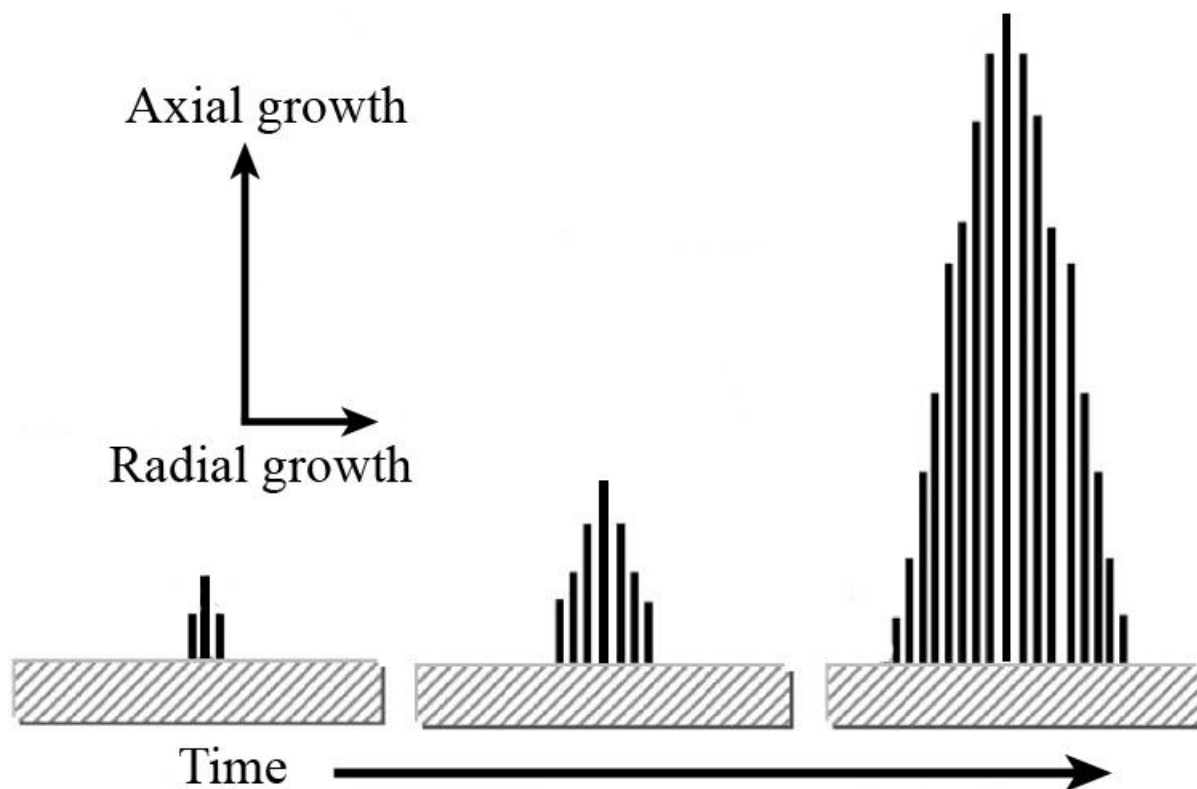


Fig. 5.8. The schematic of the formation of a cone.

5.4 Photoluminescence property of β -silicon nitride nanocones

Although Si_3N_4 nanomaterials have been investigated a lot, the products gained were almost α - Si_3N_4 or mixtures of α - Si_3N_4 with a small amount of β - Si_3N_4 . As is known, except for the reported β - Si_3N_4 nanowires, few single-crystalline β - Si_3N_4 nanomaterials with other morphologies have been reported so far.

For the photoluminescence of the reported β - Si_3N_4 nanowires, no PL spectrum from crystalline Si_3N_4 is observed. The weak peaks appearing between 400 and 600 nm are believed to derive from existing defects and impurities in the sample. In these experiments, photoluminescence was not observed, confirming a good crystalline structure.

But the photoluminescence property of nanocones, exhibits much different from that of nanostructures with other morphologies. For nanocones and nanocones related nanostructures, like nanosaws, owing to the unique structure, the density of defects such as vacancy and dangling bonding is huge, resulting in a special feature in photoluminescence.

Previous studies^{295,296} have demonstrated that Si-Si and N-N bonds and silicon and nitrogen dangling bonds are four types of defects in silicon nitride. The Si-Si bond forms a σ state and an empty σ^* state, which are separated by 4.6 eV for stoichiometric silicon nitride^{295,296}.

The Si dangling bond (K^0 center) forms a gap state around the midgap. The K^0 center is known to be amphoteric and exists in both negatively and positively charged states^{295,296}. Additionally, there are two nitrogen defect states giving rise to levels within the gap, namely N_4^+ and N_2^0 , which have been calculated to be near the conduction and valence band, respectively^{295,296}. Both N_4^+ and N_2^0 can form energy levels with the trap depth of 1.3-1.5 eV from the Si-Si band edges^{295,296}. The presence of silicon and nitrogen dangling bonds has been confirmed by analysis of ^{29}Si and ^{14}N hyperfine spectra, respectively²⁹⁷.

Fig. 5.9(a) shows the results of the photoluminescence spectra of Si_3N_4 nanocones. And the fitting curves are shown in Fig. 5.9(b). From 5.9 and 5.10 we can see that there are four peaks in the PL spectra, located at 313, 364, 398 and 470 nm, respectively. According to the defects discussed above, the dominating peaks both at 313 nm and 364 nm arise from σ^* and N_4^+ to the valence band, respectively. The other PL peak at 470 nm are due to the recombination between Si-Si σ^* level and Si^0 level, while the peak at 398 nm may also arise from N_4^+ to the valence band. However, the PL peaks at about 550 nm to 580 nm, corresponding to an energy gap of 2.15 to 2.27 eV are missing, which, as specific features for conventional Si_3N_4 nanomaterials^{295,296}, are due to recombination processes at the silicon dangling bond.

The wavelength of the dominating peaks decreasing from 550 nm to 313 nm indicating that, the violet emission or even ultraviolet emission are specific for Si_3N_4 nanocones. These nanocones have potential applications in violet-light emitting devices.

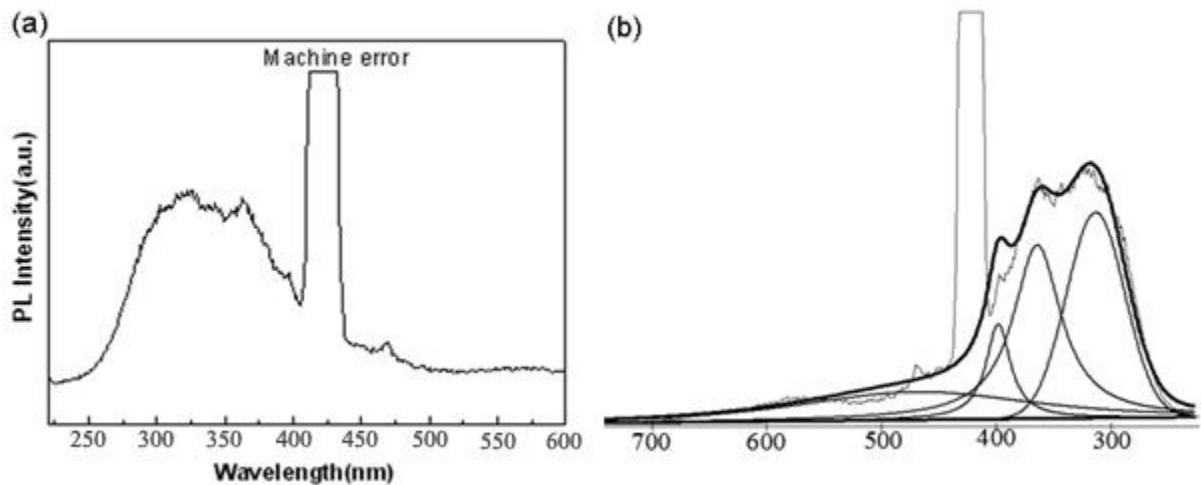


Fig. 5.9. The PL spectra and the fitting curves of Si_3N_4 nanocones.

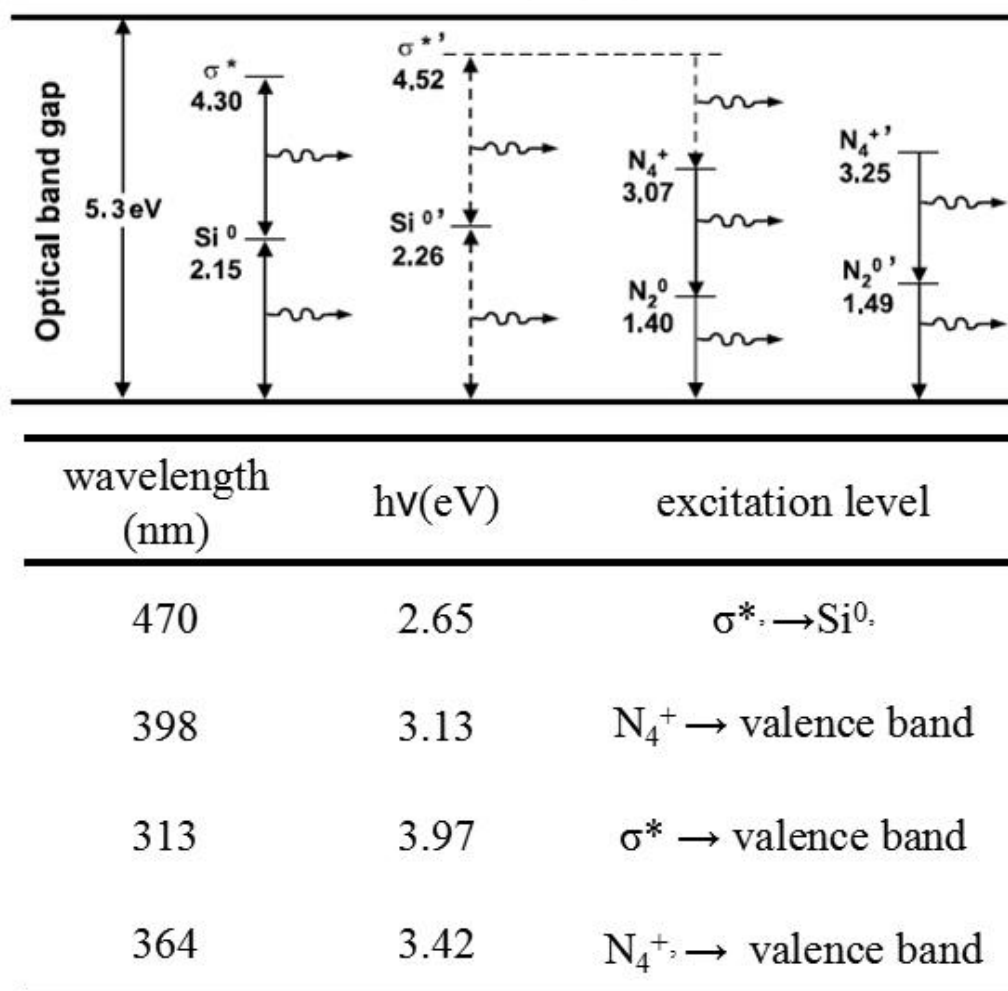


Fig. 5.10. The defects in the Si_3N_4 nanocones deducted from PL spectra.

6 Conclusions

This thesis has presented the research work that was carried out to synthesize novel single-chirality multi-wall carbon nanotubes and β -silicon nitride nanocones via a microwave plasma enhanced chemical vapor deposition technique. The work has been composed by two parts: 1) controlling the growth of single-chirality multi-wall carbon nanotubes by utilizing a new catalyst $(\text{Cr,Fe})_7\text{C}_3$ and exploiting the interactions between the catalysts and the as-gained CNTs; 2) synthesis of β - Si_3N_4 nanocones and investigation of the photoluminescence property.

In the case of growth of single-chirality multi-wall carbon nanotubes, a catalyst with high melting point is crucial to access to the final goal. Through a mass of attempts, a kind of carbide, $(\text{Cr,Fe})_7\text{C}_3$ was confirmed to be active to catalyze the growth of single-chirality MWCNTs. Additional, a relatively large solution of carbon in the catalyst and the trigonal crystal structure of the catalysts were also benefit for the CNTs growth process. The optimum experimental parameters for the growth of CNTs were as follows: gas pressure at 25 Torr, gases flow rate ratio of CH_4 and N_2 at 35:45 sccm, and the microwave power at 1100 W. The growth time is 4 hours and the growth temperature is kept at 850 °C.

Systematic investigation by SEM, TEM and ED indicated that all the CNTs gained had a single chirality. And the most common values of the chiral angle is 0 and 4.5. Detailed examination showed that the catalysts are single-crystalline. And the catalysts deformed to form monoatomic step site during the process. When a first monoatomic step site formed, the innermost graphite layer nucleated. Shortly after that, the second step site formed and the second layer nucleated. No new layers nucleated when one side of the catalyst were covered by the graphite layers and no new step formed. During the forming monoatomic step site and graphite layers nucleation, we found that the monoatomic step site played a key role for single-chirality of all the graphite layers. Firstly, the monoatomic step site was the best position for graphite layers nucleation. Secondly, a step site consisted of a basal plane and six side planes. The basal planes determined the chirality of the graphite layers. For the case of chiral angle of 0, the basal plane is (0001), while, the basal plane of (10-10) is for chiral angle of 4.5°. The six side walls were confirmed to be (20-21), (02-21), (-2201), (-2021), (0-221) and (2-201). The interplanar distances are all the same, 3.623nm, which is close to the distance of adjacent graphite layers 3.34 nm. A strained quasi-coherent interface between the catalysts and the CNTs could ignore the slight difference of the distance. And the adjacent layers extruding from the step sites could have a distance of 3.34 nm. Thirdly, duo to the symmetry of the

structure of catalyst: six side planes have the same interplanar distances and the atomic distribution, the latter atomic step site have the same basal plane with the former one, which forced all the graphite layers with the same chirality. Defects were definitely existed because of the graphite layers with the same chirality but different diameters. With the increasing of layers, the new layer would tend to be tubular with facets, which was coincide with the SEM observation.

The single-chirality MWCNTs with facet morphology gave the chance to connect the morphological helical angles with the instinctual chiral angles. SEM images of individual CNTs and the corresponding ED patterns confirm this relationship. The morphological helical angles equal to the corresponding chiral angle of the CNTs. Thus the chirality of the novel CNTs in this thesis is 'visible'. In order to explain this significant discovery, an armchair model for carbon atoms to connect with latter carbon atoms is proposed. The Raman spectra of the CNTs were also studied intensively. A weak RBM peak, a relatively strong D-band peak and a splitted G-band peak are instinctual for single-chirality MWCNT and can be envisaged as a fingerprint for single-chirality of tubular carbon nanomaterials.

In the case of β - Si_3N_4 nanocones, a thin Fe film of about 100 nm thick was used as catalysts. And the optimum experimental parameters for the growth of CNTs were: gas pressure at 30 Torr, gas flow rate ratio of CH_4 and N_2 at 15:45 sccm, and microwave power at 1500 W. The time for growth process is 120 minutes and the temperature was kept at 1100 °C. The mechanism for β - Si_3N_4 nanocones was investigated by a contrastive experiment. Without Fe catalyst, the product would be SiC thin films. After Fe atoms taking part in, Fe atoms will rob C atoms to form FeC alloy. Then the dangling Si would act with nitrogen plasma to form the final products. The cone growth can be reasonably divided into axial and radial directions, respectively. The root-based radial growth is a process of continuous nucleation of new layers outside the inner layers. A layer-by-layer growth model can describe this continuous formation of additional sheets along the radial direction. Simultaneously, the axial growth elongates the formed sheets along the axial direction and keeps the as-formed sticking sequence. The conical shape of the cones was controlled by the axial growth rate and the radial growth rate. And obviously the former is much larger than the latter, resulting in the very sharp tips of the cones. At last, the photoluminescence property of β - Si_3N_4 nanocones was studied compared with conventional Si_3N_4 nanomaterials. Normally, Si-Si and N-N bonds and silicon and nitrogen dangling bonds are four types of defects in silicon nitride. Different from conventional Si_3N_4 nanomaterials, which have a dominating exciting wavelength of 550 nm, the wavelength of the dominating peaks decreasing to 313 nm indicating that, the violet emission

or even ultraviolet emission are specific for Si_3N_4 nanocones. These nanocones have potential applications in violet-light emitting devices.

7 References

- [1] Kaenzig, W. *Phys. Rev.* **1955**, 98, 549.
- [2] Smolensky, G. A.; Agranovskaya, A. I.; Popov, S. N. Isupov, V. A. *Sov. –Tech. Phys.* **1958**, 3, 1981.
- [3] <http://nano.xerox.com/nanotech/feynman.html>
- [4] Kubo, R. *J. Phys. Soc. Jpn.* **1962**, 17, 975.
- [5] <http://emuch.net/html/201110/3751142.html>
- [6] <http://emuch.net/html/201109/3655247.html>
- [7] www.materialsvIEWSchina.com/2012/08/more-robust-dna-nanotechnology-help/
- [8] www.thethirdmedia.com/Article/201001/show216771c45p1.html
- [9] Iijima, S. *Nature* **1991**, 354, 56.
- [10] Walther, D.; Cooke, D.G.; Shersten, C.; Hajar, M.; Freeman, M.R.; Hegmann, F.A. *Phys. Rev. B*, **2007**, 76, 125408.
- [11] Streiffer, S.K.; Fong, D.D. *MRS Bulletin*, **2009**, 34, 832.
- [12] Kaur, S.; Thakur, A.K.; Choudhary, A.; Bawa, S.S.; Biradar, A.M.; Annapoorni, S. *Appl. Phys. Lett.*, **2005**, 87, 102507.
- [13] Yamamoto, T.; Sato, Y.; Tanaka, T.; Hayashi, K.; Ikuhara, Y.; Sakuma, T. *J. Mater. Sci.*, **2005**, 40, 881.
- [14] Pertsev, N.; Kukhar, V.G.; Kohlstedt, H.; Waser, R. *Phys. Rev. B*, **2003**, 67, 054107.
- [15] Xu, X.; Nishimura, T.; Hirosaki, N.; Xie, R.; Zhu, Y.; Yamamoto, Y.; Tanaka, H. *J. Am. Ceram. Soc.*, **2005**, 88, 934.
- [16] Huang, S.; Ganesan, P.; Park, S.; Popov, B.N. *J. Am. Chem. Soc.*, **2009**, 131, 13898.
- [17] Ditlbacher, H.; Lamprecht, B.; Leitner, A.; Aussenegg, F.R. *Optics Lett.*, **2000**, 25, 563.
- [18] Tong, W.; Tao, N.; Wang, Z.; Lu, J.; Lu, K. *Science*, **2003**, 299, 686.

-
- [19] Lu, L.; Shen, Y.; Qian, L.; Lu, K. *Science*, **2000**, 287, 1463.
- [20] Shen, Q.; Chen, L.; Goto, T.; Hirai, T.; Yang, J.; Meisner, G.P.; Uher, C. *Appl. Phys. Lett.*, **2001**, 79, 4165.
- [21] Lotfi, H.; Shafii, M.B. *Inter. J. Ther. Sci.*, **2009**, 48, 2215.
- [22] Cao, G. Nanostructures and nanomaterials. Imperial College Press. 2004.
- [23] Zhang, S. *Mater. Today*, **2003**, 6, 20.
- [24] Lee, J.; Park, K.; Kang, M.; Park, I.; Kim, S.; Cho, W.; Han, H.; Kim, S. *J. Cryst. Growth*, **2003**, 254, 423.
- [25] Park, J.; Gu, L.; von Maltzahn, G.; Ruoslahti, E.; Bhatia, S.N.; Sailor, M.J. *Nature Mater.*, **2009**, 8, 331.
- [26] Andreazza, P.; Andreazza-Vignolle, C.; Rozenbaum, J.P.; Thomann, A.L.; Brault, P. *Surf. Coat. Tech.*, **2002**, 151-152, 122.
- [27] Amendola, V.; Meneghetti, M. *Phys. Chem. Chem. Phys.*, **2009**, 11, 3805.
- [28] Henry, C. Nanomaterials and nanochemistry. Springer press. 2007.
- [29] Hulteen, J.C.; Martin, C.R. *J. Mater. Chem.*, **1997**, 7, 1075.
- [30] Abello, S.; Perez-Ramirez, J. *Adv. Mater.*, **2006**, 18, 2436.
- [31] Mackenzie, J.D.; Bescher, E.P. *Acc. Chem. Res.*, **2007**, 40, 810.
- [32] Li, W.; Yuan, J.; Shen, X.; Gomez-Mower, S.; Xu, L.; Sithambaram, S.; Aindow, M.; Suib, S.L. *Adv. Func. Mater.*, **2006**, 16, 1247.
- [33] Bahadur, H.; Srivastava, A.K.; Sharma, R.K.; Chandra, S. *Nanoscale Res. Lett.*, **2007**, 2, 469.
- [34] Sun, S. *Adv. Mater.*, **2006**, 18, 393.
- [35] Zheng, M.; Jagota, A.; Strano, M.S.; Santos, A.P.; Barone, P.; Chou, S. G.; Diner, B.A.; Dresselhaus, M.S.; McLean, R.S.; Onoa, G.B. *Science*, **2003**, 302, 1545.
- [36] Zhang, G.Y.; Qi, P.F.; Wang, X.R.; Lu, Y.R.; Li, X.L.; Tu, R.; Bangsaruntip, S.; Mann, D.; Zhang, L.; Dai, H.J. *Science*, **2006**, 314, 974.
- [37] Arnold, M.S.; Green, A.A.; Hulvat, J.F.; Stupp, S.I.; Hersam, M.C. *Nat. Nanotechnol.*, **2006**, 1, 60.

- [38] Voggu, R.; Rao, K.V.; George, S.J.; Rao, C.N.R. *J. Am. Chem. Soc.*, **2010**, *132*, 5560.
- [39] Tanaka, T.; Jin, H.; Miyata, Y.; Fujii, S.; Suga, H.; Naitoh, Y.; Minari, T.; Miyadera, T.; Tsukagoshi, K.; Kataura, H. *Nano Lett.*, **2009**, *9*, 1497.
- [40] Yu, B.; Hou, P.X.; Li, F.; Liu, B.L.; Liu, C.; Cheng, H.M. *Carbon*, **2010**, *48*, 2941.
- [41] Tu, X.; Manohar, S.; Jagota, A.; Zheng, M. *Nature*, **2009**, *460*, 250.
- [42] Harutyunyan, R.A.; Chen, G.; Paronyan, T.M.; Pigos, E.M.; Kuznetsov, O.A.; Hewaparakrama, K.; Kim, S.M.; Zakharov, D.; Stach, E.A.; Sumanasekera, G.U. *Science*, **2009**, *326*, 116.
- [43] Hong, G.; Zhang, B.; Peng, B.; Zhang, J.; Choi, W.; Choi, J.; Kim, J.; Liu, Z. *J. Am. Chem. Soc.*, **2009**, *131*, 14642.
- [44] Ding, L.; Tselev, A.; Wang, J.Y.; Yuan, D.N.; Chu, H.B.; McNicholas, T.P.; Li, Y.; Liu, J. *Nano Lett.*, **2009**, *9*, 800.
- [45] Loebick, C.Z.; Podila, R.; Reppert, J.; Chudow, J.; Ren, F.; Haller, G.L.; Rao, A.M.; Pfefferle, L.D. *J. Am. Chem. Soc.*, **2010**, *132*, 11125.
- [46] Ghorannevis, Z.; Kato, T.; Kaneko, T.; Hatakeyama, R. *J. Am. Chem. Soc.*, **2010**, *132*, 9570.
- [47] Qu, L.T.; Du, F.; Dai, L.M. *Nano Lett.*, **2008**, *8*, 2682.
- [48] Muradov, N.; Schwitter, A. *Nano Lett.*, **2002**, *2*, 673.
- [49] Zhang, G.Y.; Jiang, X.; Wang, E.G. *Science*, **2003**, *300*, 472.
- [50] Kroto, H. W.; Heath, J. R.; O'Brien, S. C.; Curl, R. F.; Smalley, R. E. *Nature*, **1985**, *318*, 162.
- [51] Baggott, J. Perfect symmetry: the accidental discovery of buckminsterfullerene, Oxford University Press, 1994.
- [52] Aldersey-Williams, H. The most beautiful molecule, Aurum Press, London, 1995.
- [53] Kroto, H. W. *Rev. Mod. Phys.*, **1997**, *69*, 703.
- [54] Smalley, R. E. *Rev. Mod. Phys.*, **1997**, *69*, 723.
- [55] Iijima, S.; Ichihashi, T. *Nature*, **1993**, *363*, 603.
- [56] Bethune, D. S.; Kiang, C. H.; de Vries, M. S.; Gorman, G.; Savoy, R.; Vasquez, J;

- Beyers, R. *Nature*, **1993**, 363, 605.
- [57] Oberlin, A; Endo, M; Koyama, T. *J. Cryst. Growth*, **1976**, 32, 335.
- [58] Terrones, M. *Annu. Rev. Mater. Res.* **2003**, 33, 419.
- [59] Iijima S. *Mater. Sci. Eng. B*, **1993**, 19, 172.
- [60] Iijima S., Ajayan, P.M.; Ichihashi, T. *Phys. Rev. Lett.* **1992**, 69, 3100.
- [61] Ebbesen, T.W.; Ajayan, P.M. *Nature*, **1992**, 358, 220.
- [62] Cheng, H.; Li, F.; Su, G.; Pan, H.; He, L.; Sun, X.; Dresselhaus, M. *Appl. Phys. Lett.*, **1998**, 72, 3282.
- [63] Guo, T.; Nikolaev, P.; Thess, A.; Colbert, D.T.; Smalley, R.E. *Chem. Phys. Lett.*, **1995**, 243, 49.
- [64] Laplaze, D.; Bernier, P.; Maser, W.; Flamant, G.; Guillard, T.; Loiseau, A. *Carbon*, **1998**, 36, 685.
- [65] Hsu, W.; Terrones, M.; Hare, J.; Terrones, H.; Kroto, H.; Walton, D. *Chem. Phys. Lett.*, **1996**, 262, 161.
- [66] Mukul, K.; Yoshinori, A. *J. Nanosci. Nanotech.*, **2010**, 10, 3739.
- [67] Dresselhaus, M. S.; Dresselhaus, G.; Saito, R. *Carbon*, **1995**, 33, 883.
- [68] Dresselhaus, M. S.; Dresselhaus G.; Eklund, P. C. *Science of fullerenes and carbon nanotubes*, Academic Press, San Diego, 1996.
- [69] Saito, R.; Fujita, M.; Dresselhaus, G.; Dresselhaus, M.S. *Phys. Rev. B*, **1992**, 46, 1804.
- [70] Saito, R.; Fujita, M.; Dresselhaus, G.; Dresselhaus, M.S. *Appl. Phys. Lett.*, **1992**, 60, 2204.
- [71] Harris, P. J. F. *Carbon nanotubes and related structures New Materials for the Twenty-first Century*. Cambridge University Press, 2010.
- [72] Jishi, R. A.; Dresselhaus, M. S.; Dresselhaus, G. *Phys. Rev. B*, **1993**, 47, 671.
- [73] Jishi, R. A.; Inomata, D.; Nakao, K.; Dresselhaus, M. S.; Dresselhaus, G. *J. Phys. Soc. Japan*, **1994**, 63, 2252.
- [74] Subramoney, S.; Ruoff, R.S.; Lorents, D.C.; Malhotra, R. *Nature*, **1993**, 366, 637.

- [75] Lambert, J.M.; Ajayan, P.M.; Bernier, P.; Planeix, J.M.; Brotons, V. *Chem. Phys. Lett.*, **1994**, 226, 364.
- [76] Ajayan, P.M.; Lambert, J.M.; Bernier, P.; Barbedette, L.; Colliex, C.; Planeix, J.M. *Chem. Phys. Lett.* **1993**, 215, 509.
- [77] Journet, C.; Maser, W.K.; Bernier, P.; Loiseau, A.; de la Chapelle, M.L. *Nature*, **1997**, 388, 756.
- [78] Saito, Y.; Tani, Y.; Miyagawa, N.; Mitsushima, K.; Kasuya, A.; Nishina, Y. *Chem. Phys. Lett.*, **1998**, 294, 593.
- [79] Huang, H.J.; Kajiura, H.; Tsutsui, S.; Hirano, Y.; Miyakoshi, M. *Chem. Phys. Lett.*, **2001**, 343, 7.
- [80] Guo, T.; Nikoleav, P.; Rinzler, A.G.; Tomanek, D.; Colbert, D.T.; Smalley, R.E. *J. Phys. Chem.*, **1995**, 99, 10694.
- [81] Terrones, M. Production and characterization of novel fullerene-related materials: nanotubes, nanofibers and giant fullerenes. PhD thesis. Univ. Sussex. 1997.
- [82] Thess, A.; Lee, R.; Nikolaev, P.; Dai, H.; Petit, P. *Science*, **1996**, 273, 483.
- [83] Schuetzenberger, P.; Schuetzenberger, L. *C. R. Acad. Sci.*, **1890**, 111, 774.
- [84] Audier, M.; Coulon, M.; Oberlin, A. *Carbon*, **1980**, 18, 73.
- [85] Tibbets, G. *J. Cryst. Growth*, **1984**, 66, 632.
- [86] Dai, H.J.; Rinzler, A.G.; Nikolaev, P.; Thess, A.; Colbert, D.T.; Smalley, R.E. *Chem. Phys. Lett.*, **1996**, 260, 471.
- [87] Kukovecz, A.; Konya, Z.; Nagaraju, N.; Willems, I.; Tamasi, A.; Fonseca, A. *Phys Chem Chem Phys*, **2000**, 2, 3071.
- [88] Perez-Cabero, M.; Rodriguez-Ramos, I.; Guerrero-Ruiz, A. *J. Catal.*, **2003**, 215, 305.
- [89] Sen, R.; Govindaraj, A.; Rao, C.N.R. *Chem. Phys. Lett.*, **1997**, 267, 276.
- [90] Ermakova, M.A.; Ermakov, D.Y.; Chuvilin, A.L.; Kuvshin, G.G. *J. Catal.*, **2001**, 201, 183.
- [91] Pan, S.S.; Xie, Z.W.; Chang, B.H.; Sun, L.F.; Zhou, W.Y.; Wang, G. *Chem. Phys. Lett.*, **1999**, 299, 97.
- [92] Ivanov, V.; Nagy, J.B.; Lambin, P.; Lucas, A.; Zhang, X.F.; Bernaerts, D. *Chem. Phys.*

- Lett.*, **1994**, 223, 329.
- [93] Venegoni, D.; Serp, P.; Feurer, R.; Kihn, Y.; Vahlas, C.; Kalck, P. *Carbon*, **2002**, 40, 1799.
- [94] Hernadi, K.; Fonseca, A.; Nagy, J.B.; Bernaer, D.; Fudala, A.; Lucas, A.A. *Zeolites*, **1996**, 17, 416.
- [95] Fonseca, A.; Hernadi, K.; Nagy, J.B.; Bernaerts, D.; Lucas, A.A. *J. Mol. Catal. A: Chem.*, **1996**, 107, 159.
- [96] Cui, H.; Zhou, O.; Stoner, B.R. *J. Appl. Phys.*, **2000**, 88, 6072.
- [97] Wang, Y.H.; Lin, J.; Huan, C.; Chen, G.S. *Appl. Phys. Lett.*, **2001**, 79, 680.
- [98] Cho, Y.S.; Choi, G.S.; Hong, S.Y.; Kim, D. *J. Cryst. Growth.*, **2002**, 243, 224.
- [99] Duesberg, G.S.; Graham, A.P.; Liebau, M.; Seidel, R.; Unger, E.; Kreupl, F. *Nano Lett.*, **2003**, 3, 257.
- [100] Fan, S.; Chapline, M.G.; Franklin, N.R.; Tombler, T.W.; Cassell, A.M.; Dai, H. *Science*, **1999**, 283, 512.
- [101] Fan, S.; Liang, W.; Dang, H.; Franklin, N.R.; Tombler, M.G.; Chapline, T.W. *Physica E*, **2000**, 8, 179.
- [102] Hernadi, A.; Fonseca, K.; Nagy, J.B.; Bernaerts, D.; Lucas, A.A. *Carbon*, **1996**, 34, 1249.
- [103] Hernadi, K.; Fonseca, A.; Nagy, J.B.; Siska, A.; Kiricsi, I. *Appl. Catal. A*, **2000**, 199, 245.
- [104] Klinke, C.; Bonard, J.M.; Kern, K. *Surf. Sci.*, **2001**, 492, 195.
- [105] Mayne, M.; Grobert, N.; Terrones, M.; Kamalaka, R.; Ruehle, M.; Kroto, H.W. *Chem. Phys. Lett.*, **2001**, 338, 101.
- [106] Maroto Valiente A.; Navarro Lopez P.; Rodriguez Ramos I.; Guerrero Ruiz, A.; Li, C.; Xin, Q. *Carbon*, **2000**, 38, 2003.
- [107] Pan, Z.W.; Xie, S.S.; Chang, B.H.; Wang, C.Y.; Lu, L.; Liu, W. *Nature*, **1998**, 394, 631.
- [108] Sacco, A.; Thacker, P.; Chang, T.N.; Chiang, A.T.S. *J. Catal.*, **1984**, 85, 224.
- [109] Zhang, Z.J.; Wei, B.Q.; Ramanath, G.; Ajayan, P.M. *Appl. Phys. Lett.*, **2000**, 77, 3764.

- [110] Cheng, H.M.; Li, S.F.; Pan, G.; Pan, H.Y.; He, L.L.; Sun, X. *Appl. Phys. Lett.*, **1998**, *72*, 3282.
- [111] Li, Y.; Kim, W.; Zhang, Y.; Rolandi, M.; Wang, D.; Dai, H. *J. Phys. Chem. B*, **2001**, *105*, 11424.
- [112] Cheung, C.L.; Kurtz, A.; Park, H.; Lieber, C.M. *J. Phys. Chem. B*, **2002**, *106*, 2429.
- [113] Nikolaev, P.; Bronikowski, M.; Bradley, R.; Rohmund, F.; Colbert, D.; Smith, K. *Chem. Phys. Lett.*, **1999**, *313*, 91.
- [114] Zhu, S.; Su, C.H.; Cochrane, J.C.; Lehoczky, S.; Cui, Y.; Burger, A. *J. Cryst. Growth*, **2002**, *234*, 584.
- [115] Hayashi, T.; Ahm Kim Y.; Matoba, T.; Esaka, M.; Nishimura, K.; Tsukada, T. *Nano Lett.*, **2003**, *3*, 887.
- [116] Hongo, H.; Yudasaka, M.; Ichihashi, T.; Nihey, F.; Iijima, S. *Chem. Phys. Lett.*, **2002**, *361*, 349.
- [117] Kim, W.; Choi, H.C.; Shim, M.; Li, Y.; Wang, D.; Dai, H. *Nano Lett.*, **2002**, *2*, 703.
- [118] Zhang, Y.; Li, Y.; Kim, W.; Wang, D.; Dai, H. *Appl. Phys. A*, **2002**, *74*, 325.
- [119] Satishkumar, B.C.; Govindaraj, A.; Sen, R.; Rao, C.N.R. *Chem. Phys. Lett.*, **1998**, *293*, 47.
- [120] Ago, H.; Komatsu, T.; Ohshima, S.; Kuriki, Y.; Yumura, M. *Appl. Phys. Lett.*, **2000**, *77*, 79.
- [121] Hsu, C.M.; Lin, H.L.; Cgabg, C.H.; Kuo, C.T. *Thin solid films*, **2002**, *420-421*, 225.
- [122] Ago, H.; Murata, K.; Yumura, M.; Yotani, J.; Uemura, S. *Appl. Phys. Lett.*, **2003**, *82*, 811.
- [123] Bower, C.; Zhu, W.; Jin, S.; Zhou, O. *Appl. Phys. Lett.*, **2000**, *77*, 830.
- [124] Jeong, S.H.; Hwang, H.Y.; Lee, K.H.; Jeong, Y. *Appl. Phys. Lett.*, **2001**, *78*, 2052.
- [125] Terrones, M.; Grobert, N.; Olivares, J.; Zhang, J.P.; Terrones, H.; Kordatos, K. *Nature*, **1997**, *388*, 52.
- [126] Terrones, M.; Grobert, N.; Zhang, J.P.; Terrones, H.; Olivares, J.; Hsu, W.K. *Chem. Phys. Lett.*, **1998**, *285*, 299.
- [127] Chhowalla, M.; Teo, K.B.K.; Ducati, C.; Rupesinghe, N.L.; Amaratunga, G.A.J.;

- Ferrari, A.C. *J. Appl. Phys.*, **2001**, 90, 5308.
- [128] Marty, L.; Bouchiat, V.; Bonnot, A.M.; Chaumont, M.; Fournier, T.; Decossas, S. *Microelectron Eng.*, **2002**, 61–62, 485.
- [129] Colomer, J.F.; Bister, J.F.; Willems, I.; Konya, Z.; Fonseca, A.; Van Tendeloo, G. *Chem. Commun.*, **1999**, 14, 1343.
- [130] Colomer, J.F.; Stephan, C.; Lefrant, S.; Van Tendeloo, G.; Willems, I.; Konya, Z. *Chem. Phys. Lett.*, **2000**, 317, 83.
- [131] Yudasaka, M.; Kikuchi, R.; Matsui, T.; Yoshimasa, O.; Yoshimura, S. *Appl. Phys. Lett.*, **1995**, 67, 2477.
- [132] Teo, K.B.K.; Chhowalla, M.; Amaratunga, G.A.J.; Milne, W.I.; Hasko, D.G.; Pirio, G. *Appl. Phys. Lett.*, **2001**, 79, 1534.
- [133] Ren, Z.F.; Huang, Z.P.; Xu, J.W.; Wang, J.H.; Bush, P.; Siegal, M.P. *Science*, **1998**, 282, 1105.
- [134] Choi, Y.C.; Shin, Y.M.; Lee, Y.H.; Lee, B.S.; Park, G-S.; Choi, W.B. *Appl. Phys. Lett.*, **2000**, 76, 2367.
- [135] Huang, Z.P.; Xu, J.W.; Ren, Z.F.; Wang, J.H.; Siegal, M.P.; Provencio, P.N. *Appl. Phys. Lett.*, **1998**, 73, 3845.
- [136] Jiao, J.; Seraphin, S. *J. Phys. Chem. Solids*, **2000**, 61, 1055.
- [137] Kukovitsky, E.F.; Lvov, S.G.; Sainov, N.A.; Shustov, V.A.; Chernozatonskii, L.A. *Chem. Phys. Lett.*, **2002**, 355, 497.
- [138] Nolan, P.E.; Lynch, D.C.; Cutler, A.H. *J. Phys. Chem. B*, **1998**, 102, 4165.
- [139] Siegal, M.P.; Overmyer, D.L.; Provencio, P.P. *Appl. Phys. Lett.*, **2002**, 80, 2171.
- [140] Teo, K.B.K.; Chhowalla, M.; Amaratunga, G.A.J.; Milne, W.I.; Pirio, G.; Legagneux, P. *J. Vac. Sci. Technol. B*, **2002**, 20, 116.
- [141] Valentini, L.; Kenny, J.M.; Lozzi, L.; Santucci, S. *J. Appl. Phys.*, **2002**, 92, 6188.
- [142] Wright, A.C.; Xiong, Y.; Maung, N.; Eichhorn, S.J.; Young, R.J. *Mater. Sci. Eng. C*, **2003**, 23, 279.
- [143] Yudasaka, M.; Kikuchi, R.; Ohki, Y.; Ota, E.; Yoshimura, S. *Appl. Phys. Lett.*, **1997**, 70, 1817.

-
- [144] Zhang, W.D.; Wen, Y.; Tjiu, W.C.; Xu, G.Q.; Gan, L.M. *Appl. Phys. A*, **2002**, 74, 419.
- [145] Seidel, R.; Duesberg, G.S.; Unger, E.; Graham, A.P.; Liebau, M.; Kreupl, F. *J. Phys. Chem. B*, **2004**, 108, 1888.
- [146] Baek, Y-G.; Honda, S-I.; Ikuno, T.; Ohkura, S.; Katayama, M.; Hirao, T. *Jpn. J. Appl. Phys.*, **2003**, 42, 579.
- [147] Yang, Y.; Hu, Z.; Tian, Y.J.; ,Lu, Y.N.; Wang, X.Z.; Chen, Y. *Nanotechnology*, **2003**, 14, 733.
- [148] Wang, J.G.; Liu, C.J.; Zhang, Y.P.; Zhu, X.L.; Yu, K.L.; Zou, J. *Mol. Simult.*, **2003**, 29, 667.
- [149] Cassel, A.M.; McCool, G.C.; Tee, N.H.; Koehne, J.E.; Chen, B.; Li. *J. Appl. Phys. Lett.*, **2003**, 82, 817.
- [150] Chen, B. Parker, G.; Han, J.; Meyyappan, M.; Cassell, A.M. *Chem. Mater.*, **2002**, 14, 1891.
- [151] Maruyama, S.; Kojima, R.; Miyauchi, Y.; Chiashi, S.; Kohno, M. *Chem. Phys. Lett.*, **2002**, 360, 229.
- [152] Murakami, Y.; Miyauchi, Y.; Chiashi, S.; Maruyama, S. *Chem. Phys. Lett.*, **2003**, 374, 53.
- [153] Willems, I.; Konya, Z.; Colomer, J.F.; Van Tendeloo, G.; Nagaraju, N.; Fonseca, A. *Chem. Phys. Lett.*, **2000**, 317, 71.
- [154] Dai, H. Rinzler, A.G.; Nikolaev, P.; Thess, A.; Colbert, D.T.; Smalley, R.E. *Chem. Phys. Lett.*, **1996**, 260, 471.
- [155] Kong, J.; Cassel, A.M.; Dai, H. *Chem. Phys. Lett.*, **1998**, 292, 567.
- [156] Thess, A.; Lee, R.; Nikolaev, P.; Dai, H.; Petit, P.; Robert, J. *Science*, **1996**, 273, 483.
- [157] Mann, D.; Javey, A.; Kong, J.; Wang, Q.; Dai, H. *Nano Lett.*, **2003**, 3, 1541.
- [158] Tsai, S.H.; Chao, C.W.; Lee, C.L.; Shih, H.C. *Appl. Phys. Lett.*, **1999**, 74, 3462.
- [159] Thomann, A.L.; Salvétat, J.P.; Breton, Y.; Vignolle, C.; Brault, P. *Thin Solid Films*, **2003**, 428, 242.
- [160] Vajtai, R.; Kordas, K.; Wei, B.Q.; Bekesi, J.; Leppavuori, S.; George, T.F. *Mater. Sci. Eng. C*, **2002**, 19, 271.

- [161] Li, Y.; Liu, J.; Wang, Y.; Wang, Z.L. *Chem. Mater.*, **2001**, *13*, 1008.
- [162] Cassel, A.M.; Raymakers, A.; Kong, J.; Dai, H. *J. Phys. Chem. B*, **1999**, *103*, 6484.
- [163] Cui, H.; Eres, G.; Howe, J.Y.; Piretzky, A.; Varela, M.; Geohegan, D.B. *Chem. Phys. Lett.*, **2003**, *374*, 222.
- [164] Delzeit, L.; Chen, B.; Cassel, A.; Stevens, R.; Nguyen, C.; Meyyappan, M. *Chem. Phys. Lett.*, **2001**, *348*, 368.
- [165] Franklin, N.R.; Li, Y.; Chen, R.J.; Javey, A.; Dai, H. *Appl. Phys. Lett.*, **2001**, *79*, 4571.
- [166] Hafner, J.H.; Bronikowski, M.J.; Azamian, B.R.; Nikolaev, P.; Rinzler, A.G.; Colbert, D.T. *Chem. Phys. Lett.*, **1998**, *296*, 195.
- [167] Harutyunyan, A.R.; Pradhan, B.K.; Kim, U.J.; Chen, G.; Eklund, P.C. *Nano Lett.*, **2002**, *2*, 525.
- [168] Hornyak, G.L.; Grigorian, L.; Dillon, A.C.; Parilla, P.A.; Jones, K.M.; Heben, M.J. *J. Phys. Chem. B*, **2002**, *106*, 2821.
- [169] Su, M.; Zheng, B.; Liu, J. *Chem. Phys. Lett.*, **2000**, *322*, 321.
- [170] Su, M.; Li, Y.; Maynor, B.; Buldum, A.; Lu, J.P.; Liu, J. *J. Phys. Chem. B*, **2000**, *104*, 6505.
- [171] Zheng, B.; Li, Y.; Liu, J. *Appl. Phys. A*, **2002**, *74*, 345.
- [172] Yoon, Y.J.; Bae, J.C.; Baik, H.K.; Cho, S.J.; Lee, S.J.; Song, K.M. *Chem. Phys. Lett.*, **2002**, *366*, 109.
- [173] Ago, H.; Ohshima, S.; Uchida, K.; Yumura, M. *J. Phys. Chem. B*, **2001**, *105*, 10453.
- [174] Ago, H.; Ohshima, S.; Uchida, K.; Komatsu, T.; Yumura, M. *Physica B*, **2002**, *323*, 306.
- [175] Alvarez, W.; Kitiyanan, B.; Borgna, A.; Resasco, D. *Carbon*, **2001**, *39*, 547.
- [176] Herrera, J.E.; Balzano, L.; Borgna, A.; Alvarez, W.E.; Resasco, D.E. *J. Catal.*, **2001**, *204*, 129.
- [177] Herrera, J.E.; Resasco, D.E. *J. Catal.*, **2004**, *221*, 354.
- [178] Kitiyanan, B.; Alvarez, W.E.; Harwell, J.H.; Resasco, D.E. *Chem. Phys. Lett.*, **2000**, *317*, 497.

-
- [179] Lan, A.; Iqbal, Z.; Aitouc, A.; Libera, M.; Grebel, H. *Appl. Phys. Lett.*, **2002**, *81*, 433.
- [180] Liao, X.Z.; Serquis, A.; Jia, Q.X.; Peterson, D.E.; Zhu, Y.T. *Appl. Phys. Lett.*, **2003**, *82*, 2694.
- [181] Murakami, Y.; Miyauchi, Y.; Chiashi, S.; Maruyama, S. *Chem. Phys. Lett.*, **2003**, *377*, 49.
- [182] Tang, S.; Zhong, Z.; Xiong, Z.; Sunu, L.; Liu, L.; Lin, J. *Chem. Phys. Lett.*, **2001**, *350*, 19.
- [183] Chen, P.; Zhang, H.B.; Lin, G.D.; Hong, Q.; Tsai, K.R. *Carbon*, **1997**, *35*, 1495.
- [184] Hu, Y.H.; Ruckenstein, E. *J. Catal.*, **1999**, *184*, 298.
- [185] Lueking, A.; Yang, R.T. *J. Catal.*, **2002**, *206*, 165.
- [186] Flahaut, E.; Govindaraj, A.; Peigney, A.; Laurent, C.; Rousset, A.; Rao, C. *Chem. Phys. Lett.*, **1999**, *300*, 236.
- [187] Flahaut, E.; Peigney, A.; Laurent, C.; Rousset, A. *J. Mater. Chem.*, **2000**, *10*, 249.
- [188] Wagner, R.S.; Ellis, W.C. *Trans AIME*, **1965**, *233*, 1053.
- [189] Tibbetts, G.G. *J. Cryst. Growth*, **1984**, *66*, 632.
- [190] Baker, R.T.K. *Carbon*, **1989**, *27*, 315.
- [191] Kanzow, H.; Ding, A. *Phys. Rev. B*, **1999**, *60*, 11180.
- [192] Rostrup-Nielsen, J.R.; Trimm, D.L. *J. Catal.*, **1977**, *48*, 155.
- [193] Dupuis, A.C. *Prog. Mater. Sci.*, **2005**, *50*, 929.
- [194] Ajayan, P.M.; Ebbesen, T.W. *Rep. Prog. Phys.*, **1997**, *60*, 1025.
- [195] Charlier, J.C.; Iijima, S. *Topics Appl. Phys.*, **2001**, *80*, 55.
- [196] Vinciguerra, V.; Buonocore, F.; Panzera, G.; Occhipinti, L. *Nanotechnology*, **2003**, *14*, 655.
- [197] Maiti, A.; Brabec, C.J.; Bernholc, J. *Phys. Rev. B: Rapid Commun.*, **1997**, *55*, 6079.
- [198] Shibuta, Y.; Maruyama, S. *Chem. Phys. Lett.*, **2003**, *382*, 381.

- [199] Helveg, S.; Lopez-Cartes, C.; Sehested, J.; Hansen, P.L.; Clausen, B.S.; Rostrup-Nielsen, J.R. *Nature*, **2004**, 427, 426.
- [200] Qin, L.-C. *Rep. Prog. Phys.*, **2006**, 69, 2761.
- [201] Weiss, L.; Engelhardt, T. *Z. Anorg. Chem.*, **1910**, 65, 38.
- [202] Turkdogan, E.T.; Bills, P.M.; Tippet, V.A. *J. Appl. Chem.*, **1958**, 8, 296.
- [203] Lang, J. *Nato Asi Series E: Appl. Sci.*, **1977**, 23, 89.
- [204] Riley, F.L. *J. Am. Ceram. Soc.*, **2000**, 83, 245.
- [205] Hardie, D.; Jack, K.H. *Nature*, **1957**, 180, 332.
- [206] Thompson, D.S.; Pratt, P. I. *Science of Ceramics*. Academic Press, New York, 1967.
- [207] Bando, Y. *Acta Crystallogr., Sect. B: Struct. Sci., B*, **1983**, 39, 185.
- [208] Billy, M.; Labbe, J. C.; Selvaraj, A.; Roult, G. *Mater. Res. Bull.*, **1983**, 18, 921.
- [209] Wild, S.; Grieveson, P.; Jack, K.H. *Special Ceramics*. British Ceramic Research Association, Stoke-on-Trent, U.K., 1972.
- [210] Shi, G.; Zhang, M.Q.; Rong, M.Z.; Wetzell, B.; Friedrich, K. *Wear*, **2003**, 254, 784.
- [211] Sajgalik, P.; Hnatko, M.; Lofaj, F.; Hvizdos, P.; Dusza, J.; Warbichler, P.; Hofer, F.; Riedel, R.; Lecomte, E.; Hoffmann, M.J. *J. Eur. Ceram. Soc.*, **2000**, 20, 453.
- [212] Zhang, Y.J.; Wang, N.L.; He, R.R.; Zhang, Q.; Zhu, J.; Yan, Y.J. *J. Mater. Res.*, **2000**, 15, 1048.
- [213] Munakata, F.; Matsuo, K.; Furuya, K.; Akimune, Y.; Ye, J.; Ishikawa, I. *Appl. Phys. Lett.*, **1999**, 74, 3498.
- [214] Honda, K.; Yokoyama, S.; Tanaka, S. *Appl. Spectrosc.*, **1998**, 52, 1274.
- [215] Kuo C.M.; Kuo, P.C. *J. Appl. Phys.*, **2000**, 87, 419.
- [216] Wong, E.W.; Sheehan, P.E.; Lieber, C.M. *Science*, **1997**, 277, 1971.
- [217] Kim P.; Lieber, C.M. *Science*, **1999**, 286, 2148.
- [218] Shen, G.; Bando, Y.; Liu, B.; Tang, C.; Huang, Q.; Golberg, D. *Chem. Eur. J.*, **2006**, 12, 2987.

-
- [219] Zhu, N.; Peng, Z.; Fu, X.; Wang, C.; Fu, Z.; Qi, L.; Miao, H. *Solid State Sci.*, **2010**, *12*, 1076.
- [220] Yang, W.; Xie, Z.; Miao, H. Zhang, L. Ji, H.; An, L. *J. Am. Ceram. Soc.*, **2005**, *88*, 466.
- [221] Gao, F.; Yang, W.; Fan, Y.; An, L. *Nanotechnology*, **2008**, *19*, 105602.
- [222] Yang, W.; Gao, F.; Wang, H.; Xie, Z.; An, L. *Crystal Growth & Design*, **2008**, *8*, 2607.
- [223] Yang, W.Y.; Xie, Z.P.; Miao, H.Z.; Zhang, L.G.; Ji, H.; An, L. *J. Am. Ceram. Soc.*, **2005**, *88*, 466.
- [224] Yin, L.W.; Bando, Y.; Zhu, Y.C.; Li, Y.B. *Appl. Phys. Lett.*, **2003**, *83*, 3584.
- [225] Han, W.; Fan, S.; Li, Q.; Gu, B.; Zhang, X.; Yu, D. *Appl. Phys. Lett.*, **1997**, *71*, 2271.
- [226] Zhang, L.D.; Meng, G.W.; Phillipp, F. *Mater. Sci. Eng. A*, **2000**, *286*, 34.
- [227] Gundiah, G.; Madhav, G.V.; Govindaraj, A.; Seikh, M.M.; Rao, C.N.R. *J. Mater. Chem.*, **2002**, *12*, 1606.
- [228] Gao, Y.H.; Bando, Y.; Kurashima, K.; Sato, T. *Microsc. Microanal.*, 2002, *8*, 5.
- [229] Kim, H.; Park, J.; Yang, H. *Chem. Phys. Lett.*, **2003**, *372*, 269.
- [230] Tang, C.; Ding, X.; Huan, X.; Gan, Z.W.; Liu, W.; Qi, S.R. *Jpn. J. Appl. Phys. Part 2*, **2002**, *41*, 589.
- [231] Tang, K.B.; Hu, J.Q.; Lu, Q.; Xie, Y.; Zhu, J.; Qian, Y.T. *Adv. Mater.*, **1999**, *11*, 653.
- [232] Srikanth, V. Deposition and characterization of Nanocrystalline Diamond/ β -SiC composite film system; Shaker Verlag, 2008.
- [233] The Physics of Diamond; Papali, P., Ed.; IOS Press: Amsterdam, 1996.
- [234] Zhang, X.F. *J. Cryst. Growth*, **1993**, *130*, 368.
- [235] Reznik, D. *Phys. Rev. B*, **1995**, *52*, 116.
- [236] Zhang, X.B.; Zhang, X. F.; Amelinckx, S.; Van Tendeloo, G.; Van Landuyt, J. *Ultramicroscopy*, **1994**, *54*, 237.
- [237] Chiang W.; Sankaran R.M. *Nat. Mater.*, **2009**, *8*, 882.

-
- [238] Wang, B.; Wei, L.; Yao, L.; Li, L.; Yang, Y.; Chen, Y. *J. Phys. Chem. C*, **2007**, *111*, 14612.
- [239] Xu, Z.; Bai, X.; Wang, Z.L.; Wang, E. *J. Am. Chem. Soc.*, **2006**, *128*, 1052.
- [240] Ruland, W.; Schaper, A. K.; Hou, H.; Greiner, A. *Carbon*, **2003**, *41*, 423.
- [241] Pattinson, S.W.; Ranganathan, V.; Murakami, H.K.; Koziol, K.; Windle, A.H. *ACS Nano*, **2012**, *6*, 7723.
- [242] Wagner, R.S.; Ellis, W.C. *Appl. Phys. Lett.*, **1964**, *4*, 89.
- [243] Dai, H.; Rinzler, A.G.; Nikolaev, P.; Thess, A.; Colbert, D.T.; Smalley, R.E. *Chem. Phys. Lett.*, **1996**, *260*, 471.
- [244] Reich, S.; Li, L.; Robertson, J. *Chem. Phys. Lett.*, **2006**, *421*, 469.
- [245] Yoshida, H.; Takeda, S.; Uchiyama, T.; Kohno, H.; Homma, Y. *Nano Lett.*, **2008**, *8*, 2082.
- [246] Iijima, S.; Ichihashi, T. *Phys. Rev. Lett.*, **1986**, *56*, 616.
- [247] Marks, L.D. *Rep. Prog. Phys.*, **1994**, *57*, 603.
- [248] Be'er, A.; Kofman, R.; Phillipp, F.; Lereah, Y. *Phys. Rev. B*, **2006**, *74*, 224111.
- [249] Jackson, R.S. *J. Iron Steel Inst.* **1970**, 208, 163.
- [250] Rodriguez-Manzo, J.A.; Terrones, M.; Terrones, H.; Kroto, H.W.; Sun, L.; Banhart, F. *Nat. Nanotech.*, **2007**, *2*, 307.
- [251] Yang, F.; Wang, X.; Zhang, D.; Yang, J.; Luo, D.; Xu, Z.; Wei, J.; Wang, J.; Xu, Z.; Peng, F.; Li, X.; Li, R.; Li, Y.; Li, M.; Bai, X.; Ding, F.; Li, Y. *Nature*, **2014**, *510*, 522.
- [252] Ding, F.; Larsson, P.; Larsson, J.A.; Ahuja, R.; Duan, H.; Rosen, A.; Bolton, K. *Nano Lett.*, **2008**, *8*, 463.
- [253] Zambelli, T.; Wintterlin, J.; Trost, J.; Ertl, G. *Science*, **1996**, *273*, 1688.
- [254] Dahl, S.; Logadottir, A.; Egeberg, R.C.; Larsen, J.H.; Chorkendorff, I.; Tornqvist, E.; Nørskov, J.K. *Phys. Rev. Lett.*, **1999**, *83*, 1814.
- [255] Gambardella, P.; Sljivancanin, Z.; Hammer, B.; Blanc, M.; Kuhnke, K.; Kern, K. *Phys. Rev. Lett.*, **2001**, *87*, 056103.
- [256] Bengaard, H.; Nørskov, J.K.; Sehested, J.; Clausen, B.S.; Nielsen, L.P.; Molenbroek,

- A.M.; Rostrup-Nielsen, J.R. *J. Catal.*, **2002**, 209, 365.
- [257] Guo, W.; Guo, Y. *J. Am. Chem. Soc.*, **2007**, 129, 2730.
- [258] Ferrari, A.C.; Meyer, J.C.; Scardaci, V.; Casiraghi, C.; Lazzeri, M.; Mauri, F. *Phys. Rev. Lett.*, **2006**, 97, 187401.
- [259] Reich, S.; Thomsen, C. *Philos. Trans. R. Soc. London A*, **2004**, 362, 2271.
- [260] Dresselhaus, M.S.; Dresselhaus, G.; Jorio, A.; Filho, A.G.S.; Saito, R. *Carbon*, **2002**, 40, 2043.
- [261] Prawer, S.; Nemanich, R.J. *Philos. Trans. R. Soc. London A*, **2004**, 362, 2537.
- [262] Silva, S.R.P.; Amaratunga, G.A.J.; Salje, E.K.H. *J. Mater. Sci.*, **1994**, 29, 4962.
- [263] Kuzmany, H.; Pfeiffer, R.; Hulman, M.; Kramberger, C. *Philos. Trans. R. Soc. London A*, **2004**, 362, 2375.
- [264] Schwan, J.; Ulrich, S.; Batori, V.; Ehrhardt, H.; Silva, S.R.P. *J. Appl. Phys.*, **1996**, 80, 440.
- [265] Silva, S.R.P.; Rafferty, B.; Amaratunga, G.A.J.; Schwan, J.; Franceschini, D.F.; Brown, L.M. *Diamond Relat. Mater.*, **1996**, 5, 401.
- [266] Dresselhaus, M.S.; Dresselhaus, G.; Eklund, P.C. *Science of Fullerenes and Carbon Nanotubes*, Academic, New York, 1996.
- [267] Yu, J.; Kalia, K.; Vashishta, P. *Europhys. Lett.*, **1995**, 32, 43.
- [268] Dresselhaus, M.S.; Dresselhaus, G.; Saito, R.; Jorio, A. *Phys. Rep.*, **2005**, 409, 47.
- [269] Jorio, A.; Saito, R.; Hafner, J.H.; Lieber, C.M.; Hunter, M.; McClure, T.; Dresselhaus, G.; Dresselhaus, M.S. *Phys. Rev. Lett.*, **2001**, 86, 1118.
- [270] Milnera, M.; Kúrti, J.; Hulman, M.; Kuzmany, H. *Phys. Rev. Lett.*, **2000**, 84, 1324.
- [271] Benoit, J.M.; Buisson, J.P.; Chauvet, O.; Godon, C.; Lefrant, S. *Phys. Rev. B*, **2002**, 66, 073417.
- [272] Zhao, Y.; Yakobson, B.I.; Smalley, R.E. *Phys. Rev. Lett.*, **2002**, 88, 185501.
- [273] Jorio, A.; Filho, A.G.S.; Dresselhaus, G.; Dresselhaus, M.S.; Swan, A.K. *Phys. Rev. B*, **2002**, 65, 1554121.
- [274] Saito, R.; Jorio, A.; Hafner, J.H.; Lieber, C.M.; Hunter, M.; McClure, T. *Phys. Rev. B*,

2001, 64, 0853121.

- [275] Rao, A.M.; Jorio, A.; Pimenta, M.A.; Dantas, M.S.S.; Saito, R.; Dresselhaus, G.; Dresselhaus, M.S. *Phys. Rev. Lett.*, **2000**, 84, 1820.
- [276] Tuinstra, F.; Koenig, J.L. *J. Phys. Chem.*, **1970**, 53, 1126.
- [277] Dresselhaus, M.S.; Eklund, P.C. *Adv. Phys.*, **2000**, 49, 705.
- [278] Thomsen, C.; Reich, S. *Phys. Rev. Lett.*, **2000**, 85, 5214.
- [279] Kürti, J.; Zdyomi, V.; Grüneis, A.; Kuzmany, H. *Phys. Rev. B*, **2002**, 65, 165433.
- [280] Huang, Y.; Duan, X.; Wei, Q.; Lieber, C. M. *Science*, **2001**, 291, 630.
- [281] Pan, Z.; Dai, Z.; Wang, Z. L. *Science*, **2001**, 291, 1947.
- [282] Huang, M.; Mao, S.; Feick, H.; Yan, H.; Wu, Y.; Kind, H.; Weber, E.; Russo, R.; Yang, P.D. *Science*, **2001**, 292, 1897.
- [283] Hu, J.Q.; Bando, Y.; Zhan, J.H.; Golberg, D. *Angew. Chem. Int. Ed.*, **2004**, 43, 4606.
- [284] Tang, C. C.; Bando, Y.; Golberg, D.; Ma, R.Z. *Angew. Chem. Int. Ed.*, **2005**, 44, 576.
- [285] Hu, J.Q.; Bando, Y.; Golberg, D.; Liu, Q.L. *Angew. Chem. Int. Ed.*, **2003**, 42, 3493.
- [286] Xia, Y.N.; Yang, P.D.; Sun, Y.G.; Wu, Y.Y.; Mayer, B.; Gates, B.; Yin, Y.D.; Kim, F.; Yan, H.Q. *Adv. Mater.*, **2003**, 15, 353.
- [287] Dai, Z.R.; Pan, Z.W.; Wang, Z.L. *Adv. Funct. Mater.*, **2003**, 13, 9.
- [288] Cui, Y.; Lieber, C.M. *Science*, **2001**, 291, 851.
- [289] Peng, X.G.; Manna, L.; Yang, W.D.; Wickham, J.; Scher, E.; Kadavanich, A.; Alivisatos, A.P. *Nature*, **2000**, 404, 59.
- [290] Gibson, C.P.; Putzer, K. *Science*, **1995**, 267, 1338.
- [291] Terauchi, M.; Tanaka, M.; Suzuki, K.; Ogino, A.; Kimura, K. *Chem. Phys. Lett.*, **2000**, 324, 359.
- [292] Wu, Z.S.; Deng, S.Z.; Xu, N.S.; Chen, J.; Zhou, J.; Chen, J. *Appl. Phys. Lett.*, **2002**, 80, 3829.
- [293] Liu, C.; Hu, Z.; Wu, Q.; Wang, X.; Chen, Y.; Sang, H.; Zhu, J.; Deng, S.; Xu, N. *J.*

Am. Chem. Soc., **2005**, 127, 1318.

- [294] Li, Y.B.; Bando, Y.; Golberg, D. *Appl. Phys. Lett.*, **2004**, 84, 3603.
- [295] Robertson, J. *Philos. Mag. B*, **1991**, 63, 57.
- [296] Deshpande, S.V.; Gulari, E.; Brown, S.W.; Rand, S.C. *J. Appl. Phys.*, 1995, 77, 6534.
- [297] Lenahan, P.M.; Curry, S.E. *Appl. Phys. Lett.*, **1990**, 56, 157

Appendix I

Table List of n/m ratio, chiral indices (m , n), diameter (d) and chiral angle (α) of carbon nanotubes.²⁴⁹

n/m	m	n	d	α	n/m	m	n	d	α	n/m	m	n	d	α	n/m	m	n	d	α
0.0000	u	0		0.000	0.1538	13	2	1.105	7.053	0.2759	29	8	2.640	11.857	0.4000	5	2	0.489	16.102
0.0333	30	1	2.389	1.626	0.1538	26	4	2.209	7.053	0.2778	18	5	1.641	11.927	0.4000	10	4	0.978	16.102
0.0345	29	1	2.311	1.682	0.1579	19	3	1.618	7.223	0.2800	25	7	2.282	12.008	0.4000	15	6	1.467	16.102
0.0357	28	1	2.233	1.740	0.1600	25	4	2.132	7.311	0.2857	7	2	0.641	12.216	0.4000	20	8	1.956	16.102
0.0370	27	1	2.154	1.804	0.1667	6	1	0.513	7.589	0.2857	14	4	1.282	12.216	0.4000	25	10	2.445	16.102
0.0385	26	1	2.076	1.872	0.1667	12	2	1.027	7.589	0.2857	21	6	1.923	12.216	0.4000	30	12	2.934	16.102
0.0400	25	1	1.998	1.945	0.1667	18	3	1.540	7.589	0.2857	28	8	2.564	12.216	0.4074	27	11	2.652	16.337
0.0417	24	1	1.920	2.024	0.1667	24	4	2.054	7.589	0.2917	24	7	2.205	12.432	0.4091	22	9	2.163	16.390
0.0435	23	1	1.841	2.111	0.1667	30	5	2.567	7.589	0.2941	17	5	1.564	12.520	0.4118	17	7	1.674	16.474
0.0455	22	1	1.763	2.204	0.1724	29	5	2.490	7.827	0.2963	27	8	2.487	12.598	0.4138	29	12	2.859	16.537
0.0476	21	1	1.685	2.307	0.1739	23	4	1.976	7.889	0.3000	10	3	0.923	12.730	0.4167	12	5	1.185	16.627
0.0500	20	1	1.607	2.419	0.1765	17	3	1.463	7.994	0.3000	20	6	1.846	12.730	0.4167	24	10	2.370	16.627
0.0526	19	1	1.528	2.543	0.1786	28	5	2.412	8.080	0.3000	30	9	2.770	12.730	0.4211	19	8	1.881	16.764
0.0556	18	1	1.450	2.680	0.1818	11	2	0.949	8.213	0.3043	23	7	2.129	12.885	0.4231	26	11	2.577	16.826
0.0588	17	1	1.372	2.833	0.1818	22	4	1.899	8.213	0.3077	13	4	1.205	13.004	0.4286	7	3	0.696	16.966
0.0625	16	1	1.294	3.004	0.1852	27	5	2.335	8.350	0.3077	26	8	2.411	13.004	0.4286	14	6	1.392	16.966
0.0667	15	1	1.216	3.198	0.1875	16	3	1.365	8.445	0.3103	29	9	2.693	13.098	0.4286	21	9	2.088	16.996
0.0667	30	2	2.431	3.198	0.1905	21	4	1.821	8.565	0.3125	18	5	1.488	13.174	0.4286	28	12	2.784	16.966
0.0690	29	2	2.353	3.304	0.1923	26	5	2.257	8.639	0.3158	19	6	1.770	13.289	0.4333	30	13	2.991	17.142
0.0714	14	1	1.137	3.418	0.2000	5	1	0.436	8.948	0.3182	22	7	2.052	13.373	0.4348	23	10	2.295	17.187
0.0714	28	2	2.275	3.418	0.2000	10	2	0.872	8.948	0.3200	25	8	2.335	13.436	0.4375	16	7	1.599	17.269
0.0741	27	2	2.197	3.540	0.2000	15	3	1.308	8.948	0.3214	28	9	2.617	13.486	0.4400	25	11	2.502	17.345
0.0769	13	1	1.059	3.670	0.2000	20	4	1.744	8.948	0.3333	3	1	0.282	13.898	0.4444	9	4	0.903	17.480
0.0769	26	2	2.119	3.670	0.2000	25	5	2.180	8.948	0.3333	6	2	0.565	13.898	0.4444	18	8	1.806	17.480
0.0800	25	2	2.040	3.811	0.2000	30	6	2.616	8.948	0.3333	9	3	0.847	13.898	0.4444	27	12	2.709	17.480
0.0833	12	1	0.981	3.963	0.2069	29	6	2.539	9.223	0.3333	12	4	1.129	13.898	0.4483	29	13	2.916	17.596
0.0833	24	2	1.962	3.963	0.2083	24	5	2.103	9.280	0.3333	15	5	1.412	13.898	0.4500	20	9	2.013	17.647
0.0870	23	2	1.884	4.128	0.2105	19	4	1.667	9.367	0.3333	18	6	1.694	13.898	0.4545	11	5	1.110	17.784
0.0909	11	1	0.903	4.307	0.2143	14	3	1.231	9.515	0.3333	21	7	1.976	13.898	0.4545	22	10	2.220	17.784
0.0909	22	2	1.806	4.307	0.2143	28	6	2.461	9.515	0.3333	24	8	2.259	13.898	0.4583	24	11	2.427	17.897
0.0952	21	2	1.728	4.502	0.2174	23	5	2.025	9.637	0.3333	27	9	2.541	13.898	0.4515	13	6	1.317	17.992
0.1000	10	1	0.825	4.715	0.2222	9	2	0.795	9.826	0.3333	30	10	2.823	13.898	0.4615	26	12	2.635	17.992
0.1000	20	2	1.650	4.715	0.2222	18	4	1.569	9.826	0.3448	29	10	2.747	14.290	0.4643	28	13	2.842	18.073
0.1000	30	3	2.475	4.715	0.2222	27	6	2.384	9.826	0.3462	26	9	2.465	14.335	0.4667	15	7	1.524	18.143
0.1034	29	3	2.397	4.869	0.2273	22	5	1.948	10.023	0.3478	23	8	2.183	14.392	0.4667	30	14	3.049	18.143
0.1053	9	2	1.572	4.950	0.2308	13	3	1.153	10.158	0.3500	20	7	1.900	14.465	0.4706	17	8	1.732	18.258
0.1071	28	3	2.319	5.033	0.2308	26	6	2.307	10.158	0.3529	17	6	1.618	14.564	0.4737	19	9	1.939	18.349
0.1111	9	1	0.747	5.209	0.2333	30	7	2.666	10.257	0.3571	14	5	1.336	14.705	0.4762	21	10	2.146	18.422
0.1111	18	2	1.494	5.209	0.2353	17	4	1.512	10.333	0.3571	28	10	2.672	14.705	0.4783	23	11	2.353	18.482
0.1111	27	3	2.241	5.209	0.2381	21	5	1.871	10.440	0.3600	25	9	2.389	14.800	0.4800	25	12	2.560	18.533
0.1154	26	3	2.163	5.397	0.2400	25	6	2.230	10.513	0.3636	11	4	1.053	14.921	0.4815	27	13	2.767	18.576
0.1176	17	2	1.416	5.496	0.2414	29	7	2.589	10.566	0.3636	22	8	2.107	14.921	0.4828	29	14	2.975	18.613
0.1200	25	3	2.085	5.559	0.2500	4	1	0.359	10.893	0.3667	30	11	2.878	15.021	0.5000	2	1	0.207	19.107
0.1250	8	1	0.669	5.818	0.2500	8	2	0.718	10.893	0.3684	19	7	1.825	15.079	0.5000	4	2	0.414	19.107
0.1250	16	2	1.338	5.818	0.2500	12	3	1.077	10.893	0.3704	27	10	2.596	15.143	0.5000	6	3	0.622	19.107
0.1250	24	3	2.007	5.818	0.2500	16	4	1.435	10.893	0.3750	8	3	0.771	15.295	0.5000	8	4	0.829	19.107
0.1304	23	3	1.929	6.053	0.2500	20	5	1.794	10.893	0.3750	16	6	1.542	15.295	0.5000	10	5	1.036	19.107

n/m	m	n	d	a	n/m	m	n	d	a	n/m	m	n	d	a	n/m	m	n	d	a
0.1333	15	2	1.260	6.178	0.2500	24	6	2.153	10.893	0.3750	24	9	2.314	15.295	0.5000	12	6	1.243	19.107
0.1333	30	4	2.520	6.178	0.2500	28	7	2.512	10.893	0.3793	29	11	2.803	15.436	0.5000	14	7	1.450	19.107
0.1364	22	3	1.851	6.309	0.2593	27	7	2.435	11.242	0.3810	21	8	2.031	15.490	0.5000	16	8	1.657	19.107
0.1379	29	4	2.443	6.376	0.2609	23	6	2.076	11.302	0.3846	13	5	1.260	15.608	0.5000	18	9	1.865	19.107
0.1429	7	1	0.591	6.587	0.2632	19	5	1.717	11.387	0.3846	26	10	2.520	15.608	0.5000	20	10	2.072	19.107
0.1429	14	2	1.182	6.587	0.2667	15	4	1.359	11.517	0.3889	18	7	1.749	15.746	0.5000	22	11	2.279	19.107
0.1429	21	3	1.774	6.587	0.2667	30	8	2.717	11.517	0.3913	23	9	2.238	15.824	0.5000	24	12	2.486	19.107
0.1429	28	4	2.365	6.587	0.2692	26	7	2.358	11.612	0.3929	28	11	2.727	15.874	0.5000	26	13	2.893	19.107
0.1481	27	4	2.287	6.812	0.2727	11	3	1.000	11.742						0.5000	28	14	2.900	19.107
0.1500	20	3	1.696	6.890	0.2727	22	6	1.999	11.742						0.5000	30	15	3.108	19.107
0.5172	29	15	3.034	19.591	0.6364	11	17	1.231	22.689	0.7500	4	3	0.476	25.285	0.8500	20	17	2.512	27.320
0.5185	27	14	2.827	19.626	0.6364	22	14	2.461	22.689	0.7500	8	6	0.953	25.285	0.8519	27	23	3.394	27.355
0.5200	25	13	2.619	19.667	0.6400	25	16	2.803	22.777	0.7500	12	9	1.429	25.285	0.8571	7	6	0.382	27.457
0.5217	23	12	2.412	19.715	0.6400	14	9	1.572	22.846	0.7500	16	12	1.905	25.285	0.8571	14	12	1.795	27.457
0.3238	21	11	2.205	19.773	0.6429	28	18	3.144	22.846	0.7500	20	15	2.382	25.285	0.8571	21	18	1.765	27.457
0.5263	19	10	1.996	19.842	0.6471	17	11	1.913	22.947	0.7500	24	18	2.858	25.286	0.8571	28	24	2.647	27.457
0.5294	17	9	1.791	19.927	0.6500	20	13	2.255	23.018	0.7500	28	21	3.334	25.285	0.8621	29	25	3.530	27.457
0.5333	15	8	1.584	20.034	0.6522	23	15	2.596	23.070	0.7500	24	18	2.858	25.285	0.8636	22	19	2.783	27.581
0.5333	30	16	3.167	20.034	0.6538	26	17	2.937	23.110	0.7586	29	22	3.469	25.469	0.8667	15	13	1.900	27.638
0.5357	28	15	2.960	20.099	0.6552	29	19	3.278	23.141	0.7600	25	19	2.993	25.498	0.8696	23	20	2.918	27.693
0.5385	13	7	1.376	20.174	0.6667	3	2	0.341	23.413	0.7600	25	19	2.993	25.498	0.8750	8	7	1.018	27.796
0.5385	26	14	2.753	20.174	0.6667	6	4	0.083	23.413	0.7619	21	16	2.517	25.539	0.8750	16	14	2.036	27.796
0.5417	24	13	2.546	20.260	0.6667	9	6	1.024	23.413	0.7647	17	13	2.040	25.598	0.8750	24	21	3.054	27.796
0.5455	11	16	1.169	20.363	0.6667	12	8	1.368	23.413	0.7667	30	23	3.605	25.639	0.8800	25	22	3.189	27.889
0.5455	22	12	2.339	20.363	0.6667	15	10	1.707	23.413	0.7692	13	10	1.564	25.693	0.8824	17	15	2.171	27.933
0.5500	20	11	2.132	20.485	0.6667	18	12	2.048	23.413	0.7692	26	20	3.128	25.693	0.8846	26	23	3.325	27.975
0.5517	29	16	3.094	20.531	0.6667	21	14	2.369	23.413	0.7727	22	17	2.652	25.767	0.8889	9	8	1.153	28.055
0.5556	9	5	0.962	20.633	0.6667	24	16	2.731	23.413	0.7778	9	7	1.088	25.872	0.8889	18	16	2.307	28.055
0.5556	18	10	1.924	20.633	0.6667	27	18	3.072	23.413	0.7778	18	14	2.176	25.872	0.8889	27	24	3.490	28.055
0.5556	27	15	2.887	20.633	0.6667	30	20	3.413	23.413	0.7778	27	21	3.264	25.872	0.8929	28	25	3.596	28.128
0.5600	25	14	2.680	20.751	0.6786	28	19	3.207	23.691	0.7778	27	21	3.264	25.872	0.8947	19	17	2.443	28.163
0.5625	16	9	1.717	20.817	0.6800	25	17	2.865	23.724	0.7826	23	18	2.787	25.972	0.8966	29	26	3.732	28.196
0.5652	23	13	2.472	20.889	0.6818	22	15	2.524	23.780	0.7857	14	11	1.699	26.037	0.9000	10	9	1.289	28.259
0.5667	30	17	3.228	20.927	0.6842	19	13	2.183	23.822	0.7857	28	22	3.399	26.037	0.9000	20	18	2.578	28.259
0.5714	7	4	0.755	21.052	0.6842	19	13	2.183	23.822	0.7857	28	22	3.399	26.037	0.9000	30	27	2.578	28.259
0.5714	14	8	1.510	21.052	0.6875	16	11	1.841	23.897	0.7895	19	15	2.311	26.114	0.9048	21	19	2.714	28.346
0.5714	21	12	2.265	21.052	0.6897	29	20	3.341	23.947	0.7917	24	19	2.923	26.189	0.9091	11	10	2.714	28.346
0.5714	28	16	3.021	21.052	0.6923	13	9	1.500	24.007	0.7931	29	23	3.534	26.189	0.9091	22	20	2.849	28.425
0.5769	26	15	2.814	21.195	0.6923	26	18	3.000	24.007	0.7931	29	23	3.534	26.189	0.9130	23	21	2.985	28.497
0.5789	19	11	2.058	21.247	0.6957	23	16	2.659	24.084	0.8000	5	4	0.612	26.329	0.9167	12	11	1.560	28.562
0.5833	12	7	1.303	21.361	0.7000	10	7	1.159	24.182	0.8000	10	8	1.223	26.329	0.9167	24	22	3.120	28.562
0.5833	24	14	2.606	21.361	0.7000	20	14	2.318	24.182	0.8000	15	12	1.835	26.329	0.9200	25	23	3.256	28.622
0.5862	29	17	3.155	21.435	0.7000	30	21	3.476	24.182	0.8000	20	16	2.446	26.329	0.9231	13	12	1.696	28.677
0.5882	17	10	1.851	21.487	0.7000	20	14	2.318	24.182	0.8000	25	20	3.058	26.329	0.9231	26	24	3.392	28.677
0.5909	22	13	2.399	21.555	0.7037	27	19	3.135	24.266	0.8000	30	24	3.669	26.329	0.9259	27	25	3.527	28.728
0.5926	27	16	2.948	21.398	0.7059	17	12	1.976	24.315	0.8000	30	34	3.669	26.329	0.9286	14	13	1.831	28.728
0.6000	5	3	0.548	21.787	0.7083	24	17	2.794	24.370	0.8077	26	21	3.193	26.485	0.9286	28	26	3.663	28.775
0.6000	10	6	1.096	21.787	0.7143	7	5	0.818	24.504	0.8095	21	17	2.582	26.522	0.9310	29	27	3.798	28.819
0.6000	15	9	1.644	21.787	0.7143	14	10	1.635	24.504	0.8125	16	13	1.970	26.582	0.9333	15	14	1.967	28.859
0.6000	20	12	2.193	21.787	0.7143	21	15	2.453	24.504	0.8148	27	22	3.329	26.628	0.9333	30	28	3.934	28.859
0.6000	25	15	2.741	21.787	0.7143	28	20	3.270	24.504	0.8182	11	9	1.359	26.696	0.9375	16	15	2.103	28.933
0.6000	30	18	3.289	21.787	0.7143	21	15	2.453	24.504	0.8182	22	18	2.717	26.996	0.9412	17	16	2.238	28.998
0.6071	28	17	3.082	21.967	0.7200	15	18	2.929	24.631	0.8214	28	23	3.464	26.760	0.9444	18	17	2.374	29.055
0.6154	13	8	1.437	22.173	0.7273	11	8	1.294	24.791	0.8276	29	24	3.599	26.882	0.9524	21	20	2.781	29.193

n/m	m	n	d	α	n/m	m	n	d	α	n/m	m	n	d	α	n/m	m	n	d	α
0.6154	26	16	2.875	22.173	0.7273	22	16	2.588	24.791	0.8333	6	5	0.747	26.995	0.9545	22	21	2.916	29.231
0.6190	21	13	2.327	22.264	0.7308	26	19	3.064	24.888	0.8333	12	10	1.494	26.995	0.9565	23	22	3.052	29.265
0.6207	29	18	3.216	22.304	0.7333	15	11	1.770	24.924	0.8333	18	15	2.241	26.995	0.9583	24	23	3.187	29.296
0.6250	8	5	0.889	22.411	0.7333	30	22	3.540	24.924	0.8333	24	20	2.988	26.995	0.9600	25	24	3.323	29.325
0.6250	16	10	1.779	22.411	0.7368	19	14	2.246	25.001	0.8333	30	25	3.735	26.995	0.9615	26	25	3.459	29.351
0.6250	24	15	2.668	22.411	0.7391	23	17	2.723	25.050	0.8400	25	21	3.123	27.126	0.9630	27	26	3.594	29.376
0.6296	27	17	3.009	22.525	0.7391	23	17	2.723	25.050	0.8421	19	16	2.376	27.167	0.9643	28	27	3.730	29.399
0.6316	19	12	2.120	22.572	0.7407	27	20	3.199	25.085	0.8462	13	11	1.629	27.245	0.9655	29	28	3.866	29.420
0.6333	30	19	3.351	22.015						0.8462	26	22	3.259	27.245	0.9667	30	29	4.001	29.439
															1.0000	m	m		30.000

Appendix II

Table The calculated interplanar spacings of the (Cr,Fe)₇C₃ phase.

d_{hkl}	(hkl)	Sind2	Teta	Fs2	P	I%
12.107	(-110)	2	3.65	1736	6	100
	(100)	1	3.65	1736	6	100
	(010)	1	3.65	1736	6	100
6.990	(2-10)	5	6.33	1683	6	32
	(-120)	5	6.33	1683	6	32
	(110)	2	6.33	1683	6	32
6.054	(-220)	8	7.31	1657	6	23
	(020)	4	7.31	1657	6	23
	(200)	4	7.31	1657	6	23
4.576	(3-10)	10	9.69	1584	12	25
	(-130)	10	9.69	1584	12	25
	(-230)	13	9.69	1584	12	25
	(3-20)	13	9.69	1584	12	25
	(120)	5	9.69	1584	12	25
	(210)	5	9.69	1584	12	25
4.523	(001)	1	9.81	0.00	2	0
4.237	(1-11)	3	10.47	0.00	12	0
	(-101)	2	10.47	0.00	12	0
	(011)	2	10.47	0.00	12	0
	(0-11)	2	10.47	0.00	12	0
	(-111)	3	10.47	0.00	12	0
	(101)	2	10.47	0.00	12	0
4.036	(-330)	18	11.00	1537	6	9
	(300)	9	11.00	1537	6	9
	(030)	9	11.00	1537	6	9
3.797	(-121)	6	11.70	0.00	12	0
	(-211)	6	11.70	0.00	12	0
	(2-11)	6	11.70	0.00	12	0
	(-12-1)	6	11.70	0.00	12	0
	(11-1)	3	11.70	0.00	12	0
	(111)	3	11.70	0.00	12	0
3.623	(20-1)	5	12.27	0.00	12	0
	(-221)	9	12.27	0.00	12	0
	(02-1)	5	12.27	0.00	12	0
	(2-21)	9	12.27	0.00	12	0
	(021)	5	12.27	0.00	12	0
	(201)	5	12.27	0.00	12	0
3.495	(220)	8	12.73	1471	6	7
3.358	(310)	10	13.26	1450	12	12
	(130)	10	13.26	1450	12	12
3.217	(-13-1)	11	13.85	0.00	24	0
	(3-1-1)	11	13.85	0.00	24	0
	(21-1)	6	13.85	0.00	24	0
	(-131)	11	13.85	0.00	24	0
	(3-21)	14	13.85	0.00	24	0
	(-23-1)	14	13.85	0.00	24	0
	(-231)	14	13.85	0.00	24	0
	(12-1)	6	13.85	0.00	24	0
	(3-11)	11	13.85	0.00	24	0

	(-321)	14	13.85	0.00	24	0
	(211)	6	13.85	0.00	24	0
	(121)	6	13.85	0.00	24	0
3.011	(3-31)	19	14.82	0.00	12	0
	(-331)	19	14.82	0.00	12	0
	(30-1)	10	14.82	0.00	12	0
	(03-1)	10	14.82	0.00	12	0
	(031)	10	14.82	0.00	12	0
	(301)	10	14.82	0.00	12	0
2.778	(320)	13	16.10	1333	12	7
	(230)	13	16.10	1333	12	7
2.766	(22-1)	9	16.17	0.00	12	0
	(221)	9	16.17	0.00	12	0
2.696	(31-1)	11	16.60	0.00	24	0
	(13-1)	11	16.60	0.00	24	0
	(311)	11	16.60	0.00	24	0
	(131)	11	16.60	0.00	24	0
2.367	(32-1)	14	18.99	0.00	24	0
	(23-1)	14	18.99	0.00	24	0
	(321)	14	18.99	0.00	24	0
	(231)	14	18.99	0.00	24	0
2.330	(330)	18	19.30	1199	6	2
2.261	(002)	4	19.91	1173	2	1
2.223	(1-12)	6	20.27	1158	12	4
	(-112)	6	20.27	1158	12	4
	(012)	5	20.27	1158	12	4
	(0-12)	5	20.27	1158	12	4
	(102)	5	20.27	1158	12	4
	(-102)	5	20.27	1158	12	4
2.152	(1-22)	9	20.98	1130	12	3
	(-122)	9	20.98	1130	12	3
	(2-12)	9	20.98	1130	12	3
	(-212)	9	20.98	1130	12	3
	(112)	6	20.98	1130	12	3
	(-1-12)	6	20.98	1130	12	3
2.118	(202)	8	21.32	1116	12	3
	(022)	8	21.32	1116	12	3
	(0-22)	8	21.32	1116	12	3
	(2-22)	12	21.32	1116	12	3
	(-222)	12	21.32	1116	12	3
	(-202)	8	21.32	1116	12	3
2.071	(33-1)	19	21.83	0.00	12	0
	(331)	19	21.83	0.00	12	0
2.027	(21-2)	9	22.33	1075	24	6
	(-312)	14	22.33	1075	24	6
	(-13-2)	14	22.33	1075	24	6
	(-132)	14	22.33	1075	24	6
	(3-22)	17	22.33	1075	24	6
	(-322)	17	22.33	1075	24	6
	(2-32)	17	22.33	1075	24	6
	(-232)	17	22.33	1075	24	6
	(12-2)	9	22.33	1075	24	6
	(3-12)	14	22.33	1075	24	6
	(212)	9	22.33	1075	24	6
	(122)	9	22.33	1075	24	6
1.973	(03-2)	13	22.98	1049	12	3

	(30-2)	13	22.98	1049	12	3
	(3-32)	22	22.98	1049	12	3
	(-332)	22	22.98	1049	12	3
	(032)	13	22.98	1049	12	3
	(302)	13	22.98	1049	12	3
1.899	(22-2)	12	23.93	1013	12	2
	(222)	12	23.93	1013	12	2
1.876	(31-2)	14	24.25	1001	24	4
	(13-2)	14	24.25	1001	24	4
	(312)	14	24.25	1001	24	4
	(132)	14	24.25	1001	24	4
1.754	(32-2)	17	26.05	934.5	24	3
	(23-2)	17	26.05	934.5	24	3
	(232)	17	26.05	934.5	24	3
	(322)	17	26.05	934.5	24	3
1.623	(33-2)	22	28.34	856.5	12	1
	(332)	22	28.34	856.5	12	1
1.508	(003)	9	30.72	0.00	2	0
1.496	(-113)	11	30.99	0.00	12	0
	(013)	10	30.99	0.00	12	0
	(103)	10	30.99	0.00	12	0
	(-103)	10	30.99	0.00	12	0
	(1-13)	11	30.99	0.00	12	0
	(0-13)	10	30.99	0.00	12	0
1.474	(1-23)	14	31.51	0.00	12	0
	(-123)	14	31.51	0.00	12	0
	(2-13)	14	31.51	0.00	12	0
	(-213)	14	31.51	0.00	12	0
	(113)	11	31.51	0.00	12	0
	(-1-13)	11	31.51	0.00	12	0
1.463	(203)	13	31.77	0.00	12	0
	(-203)	13	31.77	0.00	12	0
	(023)	13	31.77	0.00	12	0
	(0-23)	13	31.77	0.00	12	0
	(2-23)	17	31.77	0.00	12	0
	(-223)	17	31.77	0.00	12	0
1.432	(-2-13)	14	32.54	0.00	24	0
	(-1-23)	14	32.54	0.00	24	0
	(213)	14	32.54	0.00	24	0
	(1-33)	19	32.54	0.00	24	0
	(-313)	19	32.54	0.00	24	0
	(-133)	19	32.54	0.00	24	0
	(3-23)	22	32.54	0.00	24	0
	(-323)	22	32.54	0.00	24	0

Curriculum Vitae

Xubo Yan

Chair of Surface and Materials Technology

Institute of Materials Engineering

University of Siegen

57076 Siegen, Germany

Phone: +49-271-7404064

xubo.yan@uni-siegen.de



Personal data

Date of birth: 1st March, 1985 **Place of birth:** Hebei, China

Nationality: Chinese **Gender:** Male **Marital status:** Single

Education

2010-till date: Wissenschaftlicher Mitarbeiter, LOT, Universität Siegen, Germany.

2007-2010: Master of Science, Institute of Metal Research, Chinese Academy of Sciences, China.

2003-2007 Bachelor of Science, School of Materials Science and Engineering, Harbin Institute of Technology, China.

2000-2003 Hebei Zhengding High School, China.

1997-2000 Middle school in Hebei, China.